Modeling and Multi-Dimensional Analysis of a Proton Exchange Membrane Fuel Cell

Daming Zhou

Univ. Bourgogne Franche-Comté, UTBM
École doctorale SPIM « Sciences pour l'ingénieur et microtechniques »

THESIS

Modeling and Multi-Dimensional Analysis of A Proton Exchange Membrane Fuel Cell

By

Daming Zhou

A dissertation presented to the
Univ. Bourgogne Franche-Comté, UTBM
in partial fulfillment of the
requirements for the degree of Doctor

28 september 2017

JURY MEMBERS:

M. Babak Nahid-Mobarakeh	Institut National Polytechnique de Lorraine, Nancy
M. Hubert Razik	Université Claude Bernard Lyon 1, Lyon
M. Mahesh Krishnamurthy	Illinois Institute of Technology, Chicago, USA
M. Demba Diallo	Université de Paris Sud, Paris
M. Abdellatif Miraoui	Université de technologie de Belfort-Montbéliard, Belfort
M. Damien Paire	Université de technologie de Belfort-Montbéliard, Belfort
M. Fei Gao	Université de technologie de Belfort-Montbéliard, Belfort
M. Alexandre Ravey	Université de technologie de Belfort-Montbéliard, Belfort

ACKNOWLEDGMENTS

This work was done while the author was with the FEMTO-ST (UMR CNRS 6174), Energy Department, Univ. Bourgogne Franche-Comte, UTBM and with the laboratory FCLAB in Belfort.

I would like to give the most sincere thanks to Prof. Dr. Fei Gao, who are respectively my supervisor in FEMTO-ST and FCLAB. I am grateful for his guidance and support in my research work and the preparation of this dissertation. I would also like to express my deepest appreciation to Prof. Dr. Alexandre Ravey and Prof. Dr. Abdellatif Miraoui, who are also my thesis supervisors, for their insightful discussion about this work and constructive comments on the dissertation.

I would also thank the colleagues in FEMTO-ST and FCLAB, for their working on the experiments corresponding to this work. Many thanks for the friends in Belfort.

I would like to give my sincere thanks to Miss MengLi Yin for her meticulous care and companionship in Strasbourg and Belfort.

Finally, I would also like to express my deepest gratitude to Miss JiaQi Shang, she gives me her companionship and a very precious journey in Meerane, Germany. This is a really unforgettable memory during my life. Thank you again for accompanying me, my forever dear Meerane, forever dear JiaQi, forever dear Jiji Zha.

PUBLICATION LIST

INTERNATIONAL JOURNALS

[1] D. Zhou, F. Gao, E. Breaz, A. Ravey, A. Miraoui, "Tridiagonal Matrix Algorithm for Real-Time Simulation of a 2-D PEM Fuel Cell Model," IEEE Trans. Ind. Electron., Accepted and to be published;

[2] D. Zhou, F. Gao, E. Breaz, A. Ravey, A. Miraoui, K. Zhang, "Dynamic phenomena coupling analysis and modeling of proton exchange membrane fuel cells," IEEE Trans. Energy Convers., Vol. 31, Issue.4, Pages 1399-1412, 2016;

[3] D. Zhou, K. Zhang, A. Ravey, F. Gao, A. Miraoui, "On-Line Estimation of Lithium Polymer Batteries State-of-Charge Using Particle Filter Based Data Fusion with Multi-Models Approach," IEEE Trans. Ind. App., Vol. 52, Issue.3, Pages 2582-2595, 2016;

[4] D. Zhou, Y. Wu, F. Gao, E. Breaz, A. Ravey, A. Miraoui, "Degradation Prediction of PEM Fuel Cell Stack Based on Multi-Physical Aging Model with Particle Filter and Extrapolation Approach," IEEE Trans. Ind. App., Vol. 53, Issue.4, Pages 4041-4052, 2017;

[5] D. Zhou, A. Al-Durra, F. Gao, A. Ravey, I. Matraji, M. G. Simões, "On-line energy management strategy of fuel cell hybrid electric vehicles based on data fusion approach," Journal of Power Source, Vol. 366, Pages 278-291, 2017;

[6] D. Zhou, F. Gao, E. Breaz, A. Ravey, A. Miraoui, "Degradation Prediction of PEM Fuel Cell Using a Moving Window Based Hybrid Prognostic Approach," Energy, Vol. 138, Pages 1175-1186, 2017;

[7] D. Zhou, A. Ravey, A. Al-Durra, F. Gao, "A Comparative Study of Extremum Seeking Methods Applied to Online Energy Management Strategy of Fuel Cell Hybrid Electric Vehicles," Energy Conversion and Management, Vol. 151, Pages 778-790, 2017;

[8] D. Zhou, K. Zhang, A. Ravey, F. Gao, A. Miraoui, "Parameter Sensitivity Analysis for Fractional-Order Modeling of Lithium-Ion Batteries," Energies, Vol. 9, Issue. 123, 2016;

[9] D. Zhou, A. Al-Durra, F. Gao, A. Ravey, I. Matraji, M. G. Simões, "On-line Energy Management Strategy of Fuel Cell Hybrid Electric Vehicles：An Fractional-Order Extremum Seeking Method," IEEE Trans. Ind. Electron., First revision;

[10] D. Zhou, T. T. Nguyen, F. Gao, E. Breaz, S. Clénet, "Global Parameters Sensitivity Analysis and Development of a 2-D Model of PEM Fuel Cells," Energy conversion and management, under review;

[11] D. Zhou, Y. Wu, F. Gao, E. Breaz, A. Ravey, A. Miraoui, "Degradation Development of a multi-physical 2-D model of PEM fuel cell for real-time control," IEEE Trans. Ind. , under review;

[12] D. Zhao, M. Dou, D. Zhou, F. Gao, "Study of the modeling parameter effects on the polarization characteristics of the PEM fuel cell", Int. J. Hydrogen Energy, Vol. 41, Issue 47, Pages 22316-22327, 2016;

INTERNATIONAL CONFERENCES

[13] D. Zhou, F. Gao, A. Ravey, A. Al-Durra, M. G. Simões, "On-line Energy Management Strategy of Fuel Cell Hybrid Electric Vehicles Based on Time Series Prediction," IEEE Transportation Electrification Conference and Expo (ITEC), Chicago, IL, Jun. 22-24, 2017;

[14] D. Zhou, F. Gao, E. Breaz, A. Ravey, A. Miraoui, "Development of a Multiphysical 2-D model of PEM Fuel Cell for Real-Time Control," IEEE Industry Applications Society Annual Meeting, Hyatt Regency Cincinnati, OH, Oct. 1-5, 2017;

[15] D. Zhou, Y. Wu, F. Gao, E. Breaz, A. Ravey, A. Miraoui, "Degradation prediction of PEM fuel cell stack based on multi-physical aging model with particle filter approach," IEEE Industry Applications Society Annual Meeting, Portland, OR, Oct. 2-6, 2016;

[16] D. Zhou, F. Gao, E. Breaz, A. Ravey, A. Miraoui, "Development of a multiphysical multidimensional modeling of proton exchange membrane fuel cell," IEEE Transportation Electrification Conference and Expo (ITEC), Dearborn, MI, Jun. 27–29, 2016;

[17] D. Zhou, K. Zhang, A. Ravey, F. Gao, A. Miraoui, "Dynamic variable coupling analysis and modeling of proton exchange membrane fuel cells for water and thermal management," IEEE Applied Power Electronics Conference and Exposition (APEC), Long Beach, CA, Mar. 20-24, 2016;

[18] D. Zhou, K. Zhang, A. Ravey, F. Gao, A. Miraoui, "On-Line Estimation of Lithium Polymer Batteries State-of-Charge Using Particle Filter Based Data Fusion with Multi-Models Approach," IEEE Industry Applications Society Annual Meeting, Dallas, TX, Oct. 18–22, 2015;
« Best paper award »

[19] D. Zhou, K. Zhang, A. Ravey, F. Gao, A. Miraoui, "On-line estimation of state of charge of Li-ion battery using an iterated extended Kalman particle filter," IEEE Transportation Electrification Conference and Expo (ITEC), Dearborn, MI, Jun. 14–17, 2015.

INTRODUCTION

During the last few decades, electric vehicles (EVs), and most recently hybrid electric vehicles powered by fuel cells (FCHEVs) have a fast growing interest due to environment pollution and energy crisis. Compared to conventional thermal machine, fuel cell power generation system shows some significant advantages, such as high conversion efficiency, reduced greenhouse gas emissions, and fast fueling time. With these advantages, fuel cells have been widely considered as a more suitable energy device for long-range EVs. Among different fuel cell types, proton exchange membrane fuel cell (PEMFC) has the aforementioned advantages. In addition, it can operate at lower temperature and lower pressure with higher power density compared to other types of fuel cells.

Nevertheless, before mass commercialization of PEMFC, there are still many research works need to be done:

1) Design of appropriate control strategies and auxiliaries to achieve PEMFC optimal working modes (air compressor, humidifier, cooling circuit, power converters, etc.);
2) Fuel cell lifespan should be increased in order to meet the requirements of different applications, 5000 hours are required for transportation applications, and 100,000 hours are required for stationary;
3) Fuel cell vehicles are currently too expensive to compete with hybrids and conventional gasoline and diesel vehicles. The production costs of the PEMFC stack and hydrogen storage needs to be reduced;
4) The solutions of producing, transporting, and dispensing hydrogen need to widespread implementation.

To achieve these goals, it is important to develop advance real-time control and monitoring methods to optimize the fuel cell operation. However, it is very difficult to observe the internal variables and state of fuel cell during its operation. Since PEMFC incorporates different control variables in different physical domains with different time constant ranges, such as voltage transient due to double layer capacitance, gas pressure variation due to the volume of gas manifold, water content variation due to the water absorption in membrane and temperature variation due to the cell thermal

capacity, all these dynamic phenomena in different physical domains are indeed inter-coupled between each other and the variation of one would influence another.

A good understand of how these parameters impact the fuel cell performance would be very useful for fuel cell system design and control development. Therefore, an accurate multi-physical PEMFC model could greatly help the system control strategy development and the parameters sensitivity analyses. The main objective of this thesis is to present a dynamic multi-dimensional multi-physical PEMFC (electrochemical, fluidic, and thermal) model, which can be used for control coupling analysis, spatial distribution of physical quantities prediction, real-time control implementation and prognostic. The main contributions of this thesis can be summarized as follows:

1) A multi-dimensional dynamic modeling approach for a PEMFC is developed. The proposed PEMFC model covers multi-physical domains for electrochemical, fluidic, and thermal features;

2) A variable coupling analysis of fuel cell dynamic behaviors is presented and discussed based on the developed dynamic PEMFC model. This coupling analysis can help engineers to design and optimize the fuel cell control strategies, especially for the water and thermal management in fuel cell systems;

3) A 2-D modeling approach for PEMFC for real-time control implementation is developed. The practical feasibilities of the modeling approach for advanced real-time control of PEMFC systems have been experimentally demonstrated;

4) Two novel approaches for PEMFC performance degradation prediction are proposed. These prediction methods have been experimentally validated and their strong capabilities on forecasting the future trend of PEMFC degradation voltage under different fuel cell operation conditions have been demonstrated.

This thesis is organized as follows: Preface presents a brief introduction of proton exchange membrane fuel cell, and gives an overview on PEMFC multi-dimensional modeling approaches.

Chapter I proposes a dynamic multi-physical model of a proton exchange membrane fuel cell which considers electrical, fluidic and thermal domains. In addition, an innovative 2-dimensional modeling approach who considers in particular the fuel cell flow field geometric form is presented, in order to fully consider the characteristics of reactant gas convection in the serpentine gas pipeline and diffusion phenomena through the gas diffusion layer (GDL).

Based on the PEMFC dynamic multi-physical model developed in the previous chapter, a variable coupling analysis of fuel cell dynamic behaviors is presented and discussed in the first part of Chapter II. The analyses of dynamic phenomena step responses are conducted using the relative gain array (RGA) for various control input variables.

Chapter III proposes a novel real-time modeling approach based on the 2-D PEMFC multi-physical model developed in the Chapter I. In this approach, differential equations for reactant gas convection and diffusion phenomena in serpentine channels are transformed into tridiagonal systems of equations, in order to use an efficient numerical solver tridiagonal matrix algorithm (TDMA). In addition, a three levels bisection algorithm has been developed to solve spatial physical quantity distributions of electrochemical domain.

In the first part of Chapter IV, A multi-physical aging model has been proposed in order to predict the output voltage degradation of PEMFC. In the proposed aging model, three most important aging phenomena during PEMFC operation are considered. In addition, particle filter and extrapolation approach are used to estimate the aging parameters. In the second part of Chapter IV, an innovative approach for PEMFC aging prediction based on a combination of model-based and data-driven methods is presented. The proposed hybrid prognostic method is able to capture both the fade trend and non–linear features observed in the fuel cell voltage degradation data.

A conclusion is given at last.

As another energy power source widely used in the FCHEV powertrain, the lithium-ion batteries have advantages of high energy density and long cycle life. In order to accurately estimate state of charge (SOC) of battery during the FCHEVs operation, a novel approach for battery SOC estimation based on multi-models data fusion technique is presented Appendix A.

The last focus of this thesis is energy management strategy for FCHEVs, since it directly affects the efficiency and performance of energy storages in FCHEVs. For example, by using a suitable energy distribution controller, the fuel cell system can be maintained in a high efficiency region and thus saving hydrogen consumption. In Appendix B, an on-line adaptive energy management control is proposed based on extremum seeking method and fractional-order calculus, in order to improve both the performance and durability of PEMFC used in the FCHEVs.

PREFACE

0.1 Introduction to Fuel Cell: What is Fuel Cell

Nowadays, the research on fuel cells is a very active field, since fuel cells have been considered as one of the most attractive green energy generation device [1]. Different from lithium-ion battery [2][3], fuel cells are energy conversion devices which require a continuous source of fuel and oxidant (usually air or pure oxygen) to sustain the chemical reaction, in order to converts chemical energy into electricity, whereas the lithium-ion battery is energy storage device.

There are many different fuel cell types. For example, a single proton exchange membrane fuel cell generally consists of two separate electrodes cathode and anode, as well as an electrolyte. The gaseous fuels and oxygen respectively transport in the gas pipeline of cathode and anode, and diffuse from the gas diffusion layer to the catalyst layer. In the anode catalyst layer, the fuel is oxidized to generate electrons and protons (positively charged hydrogen ions), these protons flow from the anode side to the cathode side through the electrolyte (membrane), and are further reduced by absorbing electrons and protons to produce water. At the same time, electrons are drawn from the anode electrode to the cathode electrode through an external electrical circuit, producing directly the electricity. The complete electrochemical reaction in the fuel cell system can be written as the following [4]:

$$\mathrm{H_2} + \frac{1}{2}\mathrm{O_2} \rightarrow \mathrm{H_2O} + \mathrm{Electricity} + \mathrm{heat}$$

Based on their functionalities, a single proton exchange membrane fuel cell in a fuel cell stack can be separated into eight functional layers: one cooling channel, one membrane, two catalyst layers, two gas diffusion layers and two gas supply channels [5]. It should be noted that, electrical potential of an individual cell is relatively low, this voltage is generally around 0.7V. In order to provide sufficient electrical power to meet the requirement of applications, a fuel cell stack is commonly composed (placed in series) of a dozen or even a hundred individual cells [6].

0.2 Different types of Fuel Cells

Fuel Cells can be mainly categorized by electrolyte types. The electrolyte types determine the catalysts types and chemical reactions inside the fuel cell, as well as the

operation temperature. The commonly used fuel cell types are listed in the following subsections.

0.2.1 Proton Exchange Membrane Fuel Cell (PEMFC)

Proton exchange membrane fuel cell is considered as a more suitable energy device for mobile applications, such as hybrid electric vehicles or portable power supply, since it can operate at lower temperature and lower pressure with higher power density compared to other types of fuel cells [7]. In the proton exchange membrane fuel cell Nafion (copolymer fluoropolymer) are usually used materials for exchange membrane, platinum is widely used as the catalyst for PEMFC. The operation temperature of proton exchange membrane fuel cell system is around 80 ℃, its chemical reactions can be expressed as follows

The electrochemical half-reaction occurs at the anode electrode:

$$2H_2 \rightarrow 4H^+ + 4e^-$$

The electrochemical half-reaction occurs at the cathode electrode:

$$O_2 + 4H^+ + 4e^- \rightarrow 4H^+ + 2H_2O$$

0.2.2 Alkaline Fuel Cell (AFC)

The alkaline fuel cell (or hydrogen-oxygen fuel cell) is one of the most developed fuel cell, which is used in Apollo space program to provide the source of electrical energy and drinking water [8]. The design of alkaline fuel cell is similar to the PEMFC, but the electrolyte used in the alkaline fuel cell is generally a porous matrix saturated with an aqueous alkaline solution, for example the potassium hydroxide (KOH) or Sodium hydroxide (NaOH). Its operation temperature is similar to PEMFC, the materials of catalyst required for the electrodes can be selected from a number of relatively inexpensive chemicals, but with a lower current density. The chemical reactions for alkaline fuel cell system can be expressed as follows:

The electrochemical half-reaction occurs at the anode electrode:

$$2H_2 + 4OH^- \rightarrow 4H_2O + 4e^-$$

The electrochemical half-reaction occurs at the cathode electrode:

$$O_2 + 2H_2O + 4e^- \rightarrow 4OH^-$$

0.2.3 Phosphoric Acid Fuel Cell (PAFC)

In the phosphoric acid fuel cell, the phosphoric acid is used as a non-conductive liquid acid (electrolyte) to transfer positive hydrogen ions from anode to cathode through an external electrical circuit [9]. Since the phosphoric acid fuel cell has a simple and stable structure, it is generally used in the stationary applications. The phosphoric acid fuel cell system can operate efficiently in the temperature range from 150 ℃ to 200 ℃, its chemical reactions can be expressed as follows:

The electrochemical half-reaction occurs at the anode electrode:

$$2H_2 \rightarrow 4H^+ + 4e^-$$

The electrochemical half-reaction occurs at the cathode electrode:

$$O_2 + 4H^+ + 4e^- \rightarrow 2H_2O$$

0.2.4 Molten Carbonate Fuel Cell (MCFC)

The Molten carbonate fuel cell is quite different from the previous fuel cell types: it uses an electrolyte composed of molten carbonate salts suspended in a porous ceramic matrix and chemically inert solid electrolyte of alumina beta [10]. The molten carbonate salts in this type produce the CO_3^{2-} migrate ion from the cathode to the anode, then the hydrogen with carbonate ions from the electrolyte to produce water, carbon dioxide, and electrons. The operating temperature of molten carbonate fuel cells is above 650 ℃, its chemical reactions can be expressed as follows:

The electrochemical half-reaction occurs at the anode electrode:

$$CO_3^{2-} + H_2 \rightarrow CO_2 + H_2O + 2e^-$$

The electrochemical half-reaction occurs at the cathode electrode:

$$CO_2 + \frac{1}{2}O_2 + 2e^- \rightarrow CO_3^{2-}$$

0.2.5 Solid Oxide Fuel Cell (SOFC)

The solid oxide fuel cell uses a solid material as the electrolyte, such as dense ceramic materials yttrium-stabilized zirconia (YSZ), which separates gases from the anode and the cathode, blocks electrons and conducts oxygen ions O^{2-} from the cathode to the anode [11]. Since the solid oxide fuel cell requires high operating temperatures (from 800 ℃ to 1000 ℃), it is generally used for stationary applications. The chemical reactions for solid oxide fuel cell system can be expressed as follows:

The electrochemical half-reaction occurs at the anode electrode:

$$2H_2 + 2O^{2-} \rightarrow 2H_2O + 4e^-$$

The electrochemical half-reaction occurs at the cathode electrode:

$$O_2 + 4e^- \rightarrow 2O^{2-}$$

0.2.6 Direct Methanol Fuel Cell (DMFC)

The methanol fueled fuel cell is derived based on the proton exchange membrane fuel cell. It directly uses methanol (CH_3OH, in a liquid form) as the fuel. The main advantage of methanol fueled fuel cell is that the methanol is a relatively stable liquid, which is easy and low cost for transportation [12]. The efficiency of methanol fueled fuel cell is lower than other fuel cell types, it is generally used for portable applications, where the energy density is more important than efficiency. During methanol fueled fuel cell operation, the methanol is firstly converted to carbon dioxide and hydrogen at the anode, and the remaining steps of the reaction are similar to the PEMFC, its chemical reactions can be expressed as follows:

The electrochemical half-reaction occurs at the anode electrode:

$$CH_3OH + H_2O \rightarrow CO_2 + 6H^+ + 6e^-$$

The electrochemical half-reaction occurs at the cathode electrode:

$$\frac{3}{2}O_2 + 6H^+ + 6e^- \rightarrow 3H_2O$$

0.3 Why We Need A Proton Exchange Membrane Fuel Cell Model

Nowadays, research on proton exchange membrane fuel cells (PEMFC) has made major advances in sustainability, cost and compactness [13] [14], compared to other types of fuel cell, the PEMFC can provide higher power density for transport and portable applications with relatively short start-up time and lower operation temperature and pressure [15].

Nevertheless, before mass commercialization of PEMFC, one of the major challenges in PEMFC research is the development of appropriate control strategy for PEMFC stack and system auxiliaries (i.e., air compressor, cooling circuit, power converter), in order to maintain the optimal operation conditions of fuel cell system [16]. In addition, the PEMFC stack is a very compact device since it incorporates different phenomena in different physical domains. During fuel cell operation, these dynamic phenomena are indeed

inter-coupled between each other and the variation of one would influence another. In practice, it is very difficult to observe the internal variables and state of fuel cell during its operation.

In order to get a good understand of how these parameters quantitatively impact the fuel cell performance, and further help engineers to design and optimize the fuel cell control strategies, one possible solution for this problem is using a model-based control method. This brings up the need of an accurate and precise PEMFC dynamic model, which at least considers the following issues:

1) Dynamic behavior should be considered for transient state control;
2) The developed model should have a capability to provide multi-dimensional behaviors, which is very useful to give insights into the interaction effects of parameters on the fuel cell spatial performance;
3) The practical feasibilities of advanced real-time control of PEMFC systems should be considered, in order to effectively perform quantitative analysis of fuel cell performance and make fast control decisions.
4) Consideration of major internal physical aging phenomena of fuel cell for degradation prediction, for example the fuel cell ohmic losses, reaction activity losses, and reactants mass transfer losses.

The above issues are detailed presented in the following subsections.

0.3.1 Dynamic Behaviors

The control of the fuel cell system (air compressor, cooling circuit, power converter, etc.) is a very complicate work because it incorporates different control variables in different physical domains [17]. During fuel cell operation, different dynamic phenomena within different time constant ranges, such as voltage transient due to double layer capacitance, gas pressure variation due to the volume of gas manifold, water content variation due to the water absorption in membrane and temperature variation due to the cell thermal capacity, can be clearly observed during load transient [18]. These dynamic phenomena in different physical domains are indeed inter-coupled between each other and the variation of one would influence another. This inter-coupling effect is especially important between the dynamic phenomena which have similar transient time constants. Thus, all these dynamic phenomena should be considered in the developed PEMFC model.

0.3.2 Spatial Distribution of Physical Quantities

Compared with one-dimensional models, a multi-dimensional PEMFC model has a capability to provide spatial distribution of physical quantities, which is very useful for spatial non-uniformity and control coupling analysis [19].

For example, the one-dimensional modeling of fuel cell bipolar plate flow field are too simplified and do not represent accurately the pressure distribution characteristics, since the fuel cell gas supply pipeline is assumed to be single and straight. In reality, cathode and anode gas supply channels may be of different patterns like single serpentine, parallel serpentine or inter-digital channels. Therefore, a comprehensive representation of non-homogeneous gas phenomenon by fully taking the geometric form of the fuel cell pipeline into consideration is particularly useful to achieve highly accurate spatial distribution information for two-dimensional model of PEMFC.

0.3.3 Real-Time Applications

Different from the common modeling approach, a real-time oriented fuel cell model has more restrictions: the accuracy and computational efficiency of a real-time fuel cell model are both crucial for model based control process [20]. A sophisticated fuel cell model can provide comprehensive physical quantities for model-based control design and optimization. While the high performance computation of a fuel cell model ensures the model-based controller can be efficiently implemented in real-time applications with a low cost of computations.

0.3.4 Degradation Prediction

It is meaningful to develop a multi-physical aging model for degradation prediction of fuel cell performance [21]. This multi-physical aging model considers the real physical aging phenomena during the PEMFC degradation process. Although the model-based methods need large computations and complex physical model, it can predict not only the system degradation trend (fuel cell output voltage decay over time), but also the information about the internal physical parameters during the degradation process.

0.4 Structure

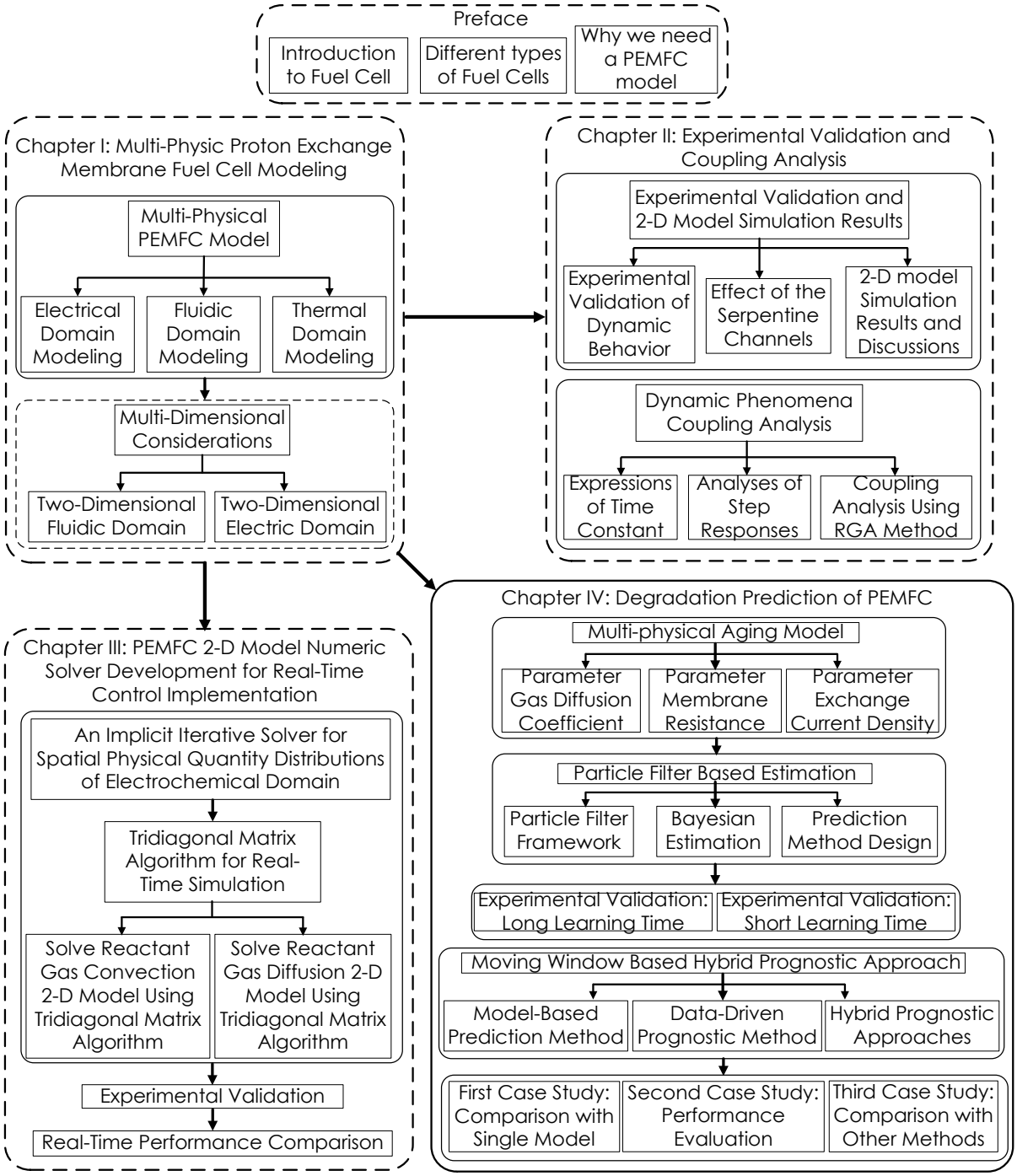

Figure 0.1 Structure

0.5 Reference

[1] F. Gao, B. Blunier, A. Miraoui, A. El-Moudni, "Cell layer level generalized dynamic modeling of a PEMFC stack using VHDL-AMS language," *Int. J. Hydrogen Energy*, vol. 34, pp. 5498-5521, Jan. 2009.

[2] D. Zhou, K. Zhang, A. Ravey, F. Gao, A. Miraoui, "On-Line Estimation of Lithium Polymer Batteries State-of-Charge Using Particle Filter Based Data Fusion with Multi-Models Approach," IEEE Trans. Ind. App., vol. 52, no.3, pp. 2582-2595, Feb. 2016.

[3] D. Zhou, K. Zhang, A. Ravey, F. Gao, A. Miraoui, "Parameter Sensitivity Analysis for Fractional-Order Modeling of Lithium-Ion Batteries," Energies, Vol. 9, no. 123, 2016;

[4] F. Gao, B. Blunier, A. Miraoui, *Proton Exchange Membrane Fuel Cell Modeling*. Hoboken, NJ, USA: Wiley, 2012.

[5] D. Zhou, F. Gao, E. Breaz, A. Ravey, A. Miraoui, K. Zhang, "Dynamic phenomena coupling analysis and modeling of PEMFCs," *IEEE Trans. Energy Convers.*, vol. 31, no. 4, pp. 1399–1412, Dec. 2016.

[6] F. Gao, B. Blunier, M. Simoes, A. Miraoui, "PEM Fuel Cell Stack Modeling for Real-Time Emulation in Hardware-in-the-Loop Applications," *IEEE Trans. Energy Convers.*, vol. 26, no. 1, pp. 184-194, March. 2011.

[7] J. Galvez, M. Ordonez, "Swinging Bus Operation of Inverters for Fuel Cell Applications With Small DC-Link Capacitance," *IEEE Trans. Power Electronics*, vol. 30, no. 2, pp. 1064-1075, Feb. 2015.

[8] G. F. McLean, T. Niet, S. Prince-Richard, and N. Djilali, "Anassessment of alkaline fuel cell technology," *Int. J. Hydrogen Energy, vol. 27, no. 507, 2002.*

[9] X. Chen, Y. Wang, L. Cai, Y. Zhou, "Maximum power output and load matching of a phosphoric acid fuel cell-thermoelectric generator hybrid system," *J. Power Sources*, vol. 294, pp. 430–436, 2015.

[10] S. J. Bae, Y. Ahn, J. Lee, J. I. Lee, "Proton exchange membrane fuel cell multi-physical dynamics and stack spatial non-homogeneity analyses," *J. Power Sources*, vol. 270, pp. 608-618, 2014.

[11] R. Kandepu, L. Imsland, B. A. Foss, C. Stiller, B. Thorud, and O. Bolland, "Modeling and control of a SOFC-GT-based autonomous power system," *Energy*, vol. 32, no. 4, pp. 406–417, Apr. 2007.

[12] N. A. Karim, S. K. Kamarudin, "An overview on non-platinum cathode catalysts for direct methanol fuel cell," *Appl. Energy*, vol. 103, pp. 212-220, 2013.

[13] A. Ravey, B. Blunier, A. Miraoui, "Control strategies for fuel cell based hybrid electric vehicles: from off-line to on-line and experimental," *IEEE Trans. Veh. Technol.*, vol. 61, no. 6, pp. 2452-2457, July. 2012.

[14] B. Somaiah, V. Agarwal, "Distributed Maximum Power Extraction From Fuel Cell Stack Arrays Using Dedicated Power Converters in Series and Parallel Configuration," *IEEE Trans. Energy Convers*, vol. 31, no. 4, pp. 1442-1451, Dec. 2016.

[15] M. Hamzeh, M. Ghafouri, H. Karimi, K. Sheshyekani, J. M. Guerrero, "Power Oscillations Damping in DC Microgrids," *IEEE Trans. Energy Convers*, vol. 31, no. 3, pp. 970-980, Sep. 2016.

[16] Q. Li, W. Chen; Z. Liu; J. Huang; L. Ma, "Net Power Control Based on Linear Matrix Inequality for Proton Exchange Membrane Fuel Cell System," *IEEE Trans. Energy Convers*, vol. 29, no. 1, pp. 1-8, Mar. 2014.

[17] D. Zhou, E. Breaz, A. Ravey, F. Gao, A. Miraoui, and K. Zhang, "Dynamic variable coupling analysis and modeling of proton exchange membrane fuel cells for water and thermal management," in *Proc. IEEE APEC,* Mar. 20-24, 2016, pp. 3476-3480.

[18] C. Kunusch, P. F. Puleston, M. A. Mayosky, A. P. Husar, "Control-Oriented Modeling and Experimental Validation of a PEMFC Generation System," *IEEE Trans. Energy Convers*, vol. 26, no. 3, pp. 851-861, Sep. 2011.

[19] A. Bıyıkoğlu, "Review of proton exchange membrane fuel cell models," *Int. J. Hydrogen Energy*, vol. 30, pp. 1181–1212, 2005.

[20] P. Massonnat, F. Gao, D. Paire, D. Bouquain, A. Miraoui, "A multi physical model for PEM fuel cells including a two dimensional fluidic finite element analysis in real time," in *Proc. IEEE ITEC*, Jun. 15-18, 2014.

[21] D. Zhou, Y. Wu, F. Gao, E. Breaz, A. Ravey A. Miraoui, "Degradation Prediction of PEM Fuel Cell Stack Based on Multi-Physical Aging Model with Particle Filter Approach," *Proc. IEEE IAS Annu. Meeting*, pp. 1-8, 2016-Oct.

Chapter I: Multi-Physic Proton Exchange Membrane Fuel Cell Modeling

In this chapter, a dynamic, multi-physical model of a proton exchange membrane fuel cell is fully developed at first. This model considers in particular the coupling effect between the dynamic behaviors during fuel cell transient operation. In addition, an innovative two-dimensional modeling approach is presented for proton exchange membrane fuel cell. Specifically, the proposed two-dimensional model covers multi-physical domains for both electrochemical and fluidic features, and fully takes the fuel cell channel geometric form into consideration.

1.1 Literature Review

Generally speaking, a lower dimensional fuel cell model may ignore some spatial physical quantities but a lower computational cost. For example, the one-dimensional model is considered as a macroscopic model, which describes the physical behaviors on the basis of individual layers in a single cell. Although the spatial distribution physical variables cannot be obtained using the one-dimensional models, the fuel cell dynamic phenomena can be well represented by first-order differential equations. Therefore, the one-dimensional models are preferred to investigate the transient behaviors inside the fuel cells. Many PEMFC dynamic models can be found in literature [1]-[4].

S. Park et al. [1] propose a dynamic PEMFC model which considers dynamic behaviors of temperature and two-phase effects. Based on the proposed model, a comparative study of transient behaviors are further performed including dynamics of temperature, oxygen and vapor concentration in the gas diffusion media, liquid water saturation, and the variations of water content in the membranes.

Z. Zhang et al. [2] propose a semi-empirical dynamic PEMFC model. The effects of the equivalent internal resistance and the stack thermal behavior on the output characteristics of PEMFC are investigated under different load conditions. The experimental validation shows that the proposed model can provide an accurate representation of the static and dynamic behaviors under different load conditions.

K. Sedghisigarchi et al. [3] give a dynamic and transient analysis based on a dynamic solid-oxide fuel cell model, the temperature dynamics in thermal domain and the output voltage losses dynamics in electrochemical domain are both considered in the developed model. The simulation results show that, for a very fast load variation, the temperature dynamics can be ignored.

F. Gao et al. [4] present a multi-physical dynamic PEMFC stack model, which can be directly used in real-time applications. This dynamic PEMFC model covers three physical domains for electrochemical, fluidic and thermal features. Specifically, a fuel cell dynamic time constants analysis is performed, and the dynamic responses of different physical domains are shown through current step.

A common drawback of these models is that the different fuel cell dynamic phenomena, especially the ones with similar time constant, are not considered simultaneously or over-simplified, thus make them unsuitable for dynamic variable coupling analysis.

Compare to one-dimensional models, multi-dimensional models have a capability to provide local phenomena and spatial distribution physical variables, which is very useful for spatial non-uniformity and control coupling analysis. However, calculating such complex physical quantities leads to higher computational requirements. Many PEMFC multi-dimensional models have been previously proposed in the literature [5]-[8].

Y. Shan et al. [5] propose a dynamic two-dimensional PEMFC model, which considers the fluidic and thermal behaviors. In order to obtain the temperature dynamic distribution along the gas channel direction and through-plane direction, a numerical solver is used based on SIMPLE algorithm. In addition to the thermal dynamic behaviors, the proposed 2-D model can also predict the current density and oxygen concentration dynamic distribution.

X. Wang et al. [6] present a three-dimensional non-isothermal PEMFC model. This model uses two different water transport equation to describe the water two-phase transportation during the fuel cell operation. Based on the developed model, a parameter sensitivity analysis is performed to show effects of different parameters on the fuel cell polarization curve.

S. Um et al. [7] develop a multi-dimensional transient model for PMFC. The proposed model simultaneously considers the electrochemical kinetics and hydrodynamics. In order to predict not only the experimental polarization curves, but also detailed distribution of electrochemical and fluidic features, the conservation equations are

numerically solved using finite volume based computational fluid dynamics (CFD) approach.

B. Sivertsen et al. [8] introduce a comprehensive non-isothermal three-dimensional PEMFC model. In the presented model, the fluid transport inside the fuel cell gas channels and gas diffusion layer, as well as the thermal behaviors are developed and solved based on the framework of a CFD code. This CFD computational model can accurately predict the cathode over-potential distribution.

A common drawback of these works is that the presented fuel cell bipolar plate flow field (gas channels) models are over-simplified (or not even considered). Thus they cannot describe accurately the non-linear and non-uniform pressure distribution characteristics. On the other hand, as a commonly used modeling technique for multi-dimensional model, the CFD models [7]-[8] are not suitable for real-time model-based controller since the computational burdens are too heavy.

1.2 Multi-Physical PEMFC Model

In this section, the presented PEMFC dynamic model is based on a developed multi-physical PEMFC model in the previous works [9]-[10]. The PEMFC stack level and the single cell level are shown in the Figure 1.1. As shown in Figure 1.1, one fuel cell stack level can be separated into eight cell layers, which consist of:

1) Cathode cooling channel layer;
2) Cathode gas supply channel layer;
3) Cathode gas diffusion layer;
4) Cathode catalyst layer;
5) Proton exchange membrane layer;
6) Anode catalyst layer;
7) Anode gas diffusion layer;
8) Anode gas supply channel layer.

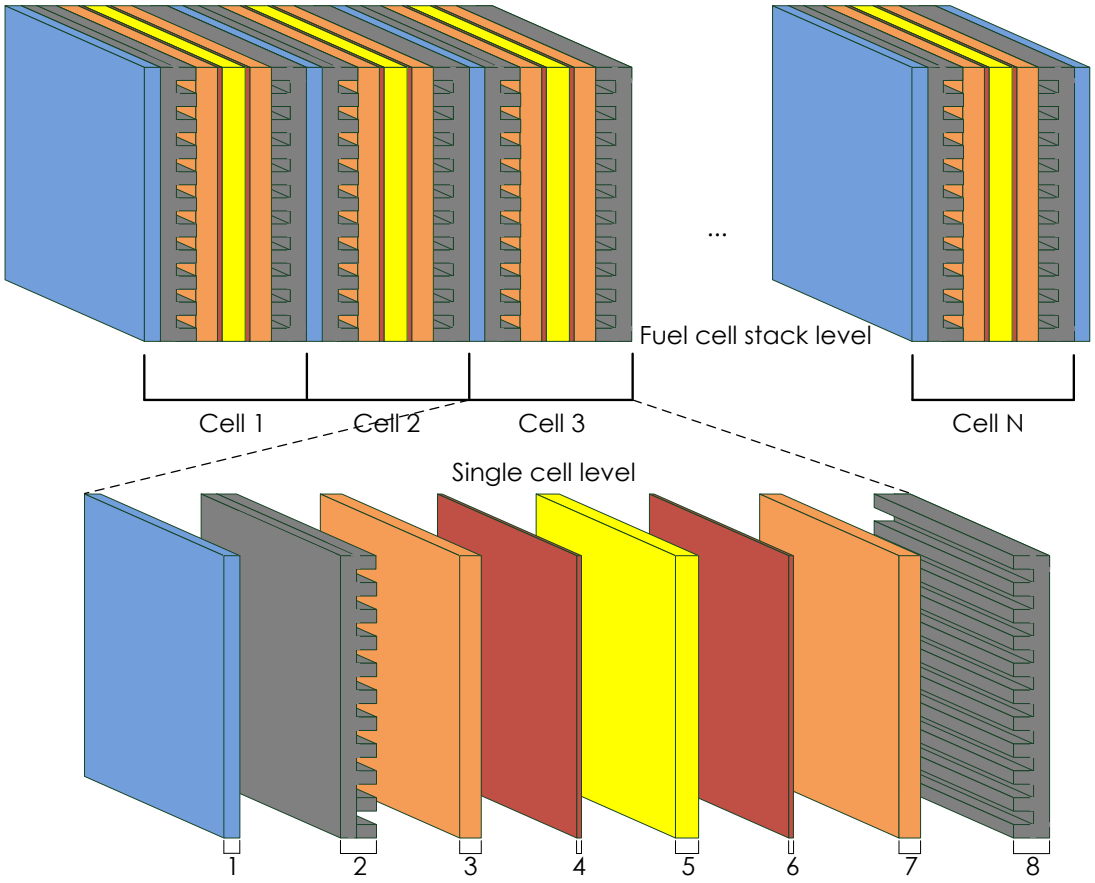

Figure 1.1 PEMFC stack level and the single cell level

The advantage of this cell layer structure is that each modeling layer can be described separately by its own physical equations and the boundary conditions. Each cell layer is considered as a control volume in the presented model. For each cell layer, the modeling of different physical domain is presented in the following subsections.

1.2.1 Electrical Domain Modeling

As an electricity-converting device, the PEMFC converts fuel energy into electricity through electrochemical reactions. Therefore, the electric domain is included in the proposed PEMFC model.

The total output voltage V_{cell} of a single-cell can be calculated by the following equation:

$$V_{cell} = E_{cell} - V_{ohmic} - V_{act} \tag{1.1}$$

where E_{cell} is the single fuel cell thermodynamic voltage (V), V_{ohmic} is the ohmic voltage drop (V), V_{act} is the cell activation voltage drop (V).

The thermodynamic voltage E_{cell} is calculated from the following Nernst equation [11]:

$$E_{cell} = 1.229 - 0.85 \cdot 10^{-3}(T_{cata} - 298.15) + \frac{R \cdot T_{cata}}{2F} \ln\left(\sqrt{P_{O_2,cata}} \cdot P_{H_2,cata}\right) \quad (1.2)$$

where T_{cata} is the catalyst layer temperature (K), $F = 96485$ is the Faraday constant (C/mol), $R = 8.314$ is the ideal gas constant, $P_{O_2,cata}$ is the oxygen pressure (atm) at the interface of cathode catalyst layer, $P_{H_2,cata}$ is the hydrogen pressure (atm) at the interface of anode catalyst layer (please refer to the last paragraph of this section).

The membrane resistance R_{mem} (Ω) is calculated by [12]:

$$R_{mem} = \frac{\int_0^{\delta_{mem}} r_{mem} dz}{A_{mem}} \quad (1.3)$$

where A_{mem} is the section surface of membrane (m^2), δ_{mem} is the membrane thickness (m). r_{mem} is the resistivity of membrane (Ω·m) which can be calculated by the following equation [12]:

$$r_{mem} = \begin{cases} \frac{1}{0.1933} e^{[1268(\frac{1}{T_{mem}} - \frac{1}{303})]} & if \quad 0 < \lambda_w < 1 \\ \frac{1}{0.5193\lambda_w - 0.326} e^{[1268(\frac{1}{T_{mem}} - \frac{1}{303})]} & if \quad \lambda_w > 1 \end{cases} \quad (1.4)$$

Thus, the cell ohmic voltage drop V_{ohmic} can be calculated from Ohm's law equation [13]:

$$V_{ohmic} = i \cdot R_{mem} \quad (1.5)$$

The electrochemical activation voltage drop V_{act} of single cell can be calculated by Butler-Volmer equation [14]:

$$i = i_0 A_{cata} \left[e^{\left(\frac{\alpha_c nF}{RT_{cata}} V_{act}\right)} - e^{\left(-\frac{(1-\alpha_c)nF}{RT_{cata}} V_{act}\right)} \right] \quad (1.6)$$

where i is the stack current (A), α_c is the charge transfer coefficient, n is the electrons number. The exchange current density i_0 (A/m^2) can be calculated by an empirical equation [15]:

$$i_0 = \gamma_c \cdot P_{O_2,cata}^{\beta_c} \cdot e^{-\frac{E_c}{RT_{cata}}\left(1 - \frac{T_{cata}}{298.15}\right)} \quad (1.7)$$

where γ_c and β_c are empirical parameters, E_c is the oxygen activation energy on the electrode catalyst interface. It should be noted that, the V_{act} in anode side for fuel cells of PEMFC type can be neglected due to the easy electrochemical process.

It can be seen from the equation 1.6 that, the term activation voltage drop V_{act} is in an implicit form. In order to explicitly calculate this non-linear implicit Butler-Volmer equation

to obtain the value of V_{act}, an iterative solver is used. For a high stack current, the Butler-Volmer equation can be written as the well-known Tafel equation [16]:

$$V_{act} = \frac{RT}{\alpha nF} ln\left(\frac{i}{i_0 A_{cata}}\right) \tag{1.8}$$

The dynamic behavior of activation losses voltage V_{act} in the electrical domain due to the "double layer effect" can be expressed by:

$$\frac{d}{dt} v_{act} = \frac{i}{C_{dl}}\left(1 - \frac{v_{act}}{V_{act}}\right) \tag{1.9}$$

1.2.2 Fluidic Domain Modeling

It should also be noted that, since the $P_{O_2,cata}$ and $P_{H_2,cata}$ used in equation 1.2 are reactant gas pressure at the catalyst layer interface instead of the gas supply channels, another fuel cell over-potential term due to pressures drop through the GDL, well known as "concentration losses", has been already implicitly considered in the proposed fluidic model. Therefore, the fluidic behaviors inside fuel cell, such as reactants convection in the channels and diffusion through gas diffusion layer, have a great impact on fuel cell performance. In this section, the fluidic domain modeling is presented.

1.2.2.1 Cooling Channels

In the gas channel, the Reynolds number can be calculated by the following equation [17]:

$$Re = \frac{\rho_{gas} V_{gas} D_{hydro}}{\mu} \tag{1.10}$$

where D_h is the channel hydraulic diameter (m), μ is the mean fluid velocity in the channel (Pa s). The mean velocity V_{gas} (m/s) of gas can be calculated based on the following equation:

$$V_{gas} = \frac{q}{A\rho_{gas}} \tag{1.11}$$

where q is the fluid mass flow (kg/s), A is the total section of cooling channels (m^2). The fluid density (kg/m^3) ρ_{gas} can be calculated by ideal gas equation of state:

$$\rho_{gas} = \frac{MP}{RT} \tag{1.12}$$

The gas pressure drop ΔP_{cool} of serpentine channel depends on the surface friction losses of straight pipeline, which can be modeled by the Darcy–Weisbach equation [18]:

$$\Delta P_{cool} = f_D \frac{\rho_{gas} L_{ch} \mu^2}{2 D_{hydro}} \tag{1.13}$$

with

$$\begin{cases} \Delta P_{in} = P_{cool,in} - P_{cool,center} \\ \Delta P_{out} = P_{cool,out} - P_{cool,center} \end{cases} \tag{1.14}$$

where $P_{cool,in}$, $P_{cool,out}$ and $P_{cool,cent}$ are respectively the pressure at inlet, outlet, and center of cooling channel, L_{ch} is the total length of straight channel (m), f_D is the Darcy friction factor which can be obtained from the empirical equation [19]:

$$f_D = \frac{64}{Re} \tag{1.15}$$

The gas pressure dynamic response in the fuel cell is generally due to the channels volume. Thus, the dynamic behaviors of fluid in the cooling channel can be given by the mass balance equation:

$$\frac{M_{gas} V_{cool}}{R T_{cool}} \left(\frac{d}{dt} P_{cool} \right) = \sum_{in/out}^{ch} q_{fluid} \tag{1.16}$$

where M_{gas} is the gas molar mass (kg/mol), V_{cool} is the volume of the cool channels (m^3), T_{cool} is the cooling channel temperature (K), P_{ch} is the gas pressure in the cool channels (Pa) and q_{fluid} is the fluid mass flow rate (kg/s) entering or leaving the channels.

1.2.2.2 Gas Supply Channels

The total pressure of the center of the gas supply channels can be calculated by:

$$P_{ca,channel} = P_{ca,O_2} + P_{ca,N_2} + P_{ca,H_2O} \tag{1.17}$$

$$P_{an,channel} = P_{an,H_2} + P_{an,H_2O} \tag{1.18}$$

where P_{ca,O_2}, P_{ca,N_2}, P_{ca,H_2O} are respectively the oxygen, nitrogen, and vapor pressure in the center of cathode supply channel. P_{an,H_2}, P_{an,H_2O} are respectively the hydrogen and vapor pressure in the center of anode supply channel. The gas pressure in the center of channels is defined as follow:

$$P_{gas,center} = \frac{P_{gas,channel,in} + P_{gas,channel,out}}{2} \tag{1.19}$$

where $P_{gas,channel,in}$ is the gas pressure at the channel inlet, and $P_{gas,channel,out}$ is the gas pressure at the channel outlet. Thus, the dynamic behaviors of fluid $m_{gas,center}$ in the center of gas supply channels can be also written based on the mass balance equation:

$$\frac{d}{dt} m_{gas,center} = q_{gas,channel,in} + q_{gas,channel,out} \quad (1.20)$$

$$m_{gas,center} = \frac{P_{gas,center} M_{gas} V_{channel}}{R T_{channel}} \quad (1.21)$$

where $q_{gas,channel,in}$ is the gas mass flow at the inlet of channel, $q_{gas,channel,out}$ is the gas mass flow at the outlet of channel, V_{cool} is the volume of the gas supply channels (m^3) and $T_{channel}$ is the temperature of gas supply channel (K).

1.2.2.3 Gas Diffusion Layer (GDL)

To obtain the reactant gas pressure at interface of the catalyst layer, the diffusion phenomenon in the gas diffusion layer can be described by modified Fick's law [20] [21]:

$$\frac{dp_{GDL,x}}{dz} = \frac{\Delta p_{GDL,x}}{\delta_{GDL}} = \frac{-R T_{GDL} \dot{N}_{GDL,x}}{A_{GDL} \cdot D^{eff}_{GDL,x-y}} \quad (1.22)$$

where $p_{GDL,x}$ is pressure of specie x in gas diffusion layer (Pa), δ_{GDL} is thickness of gas diffusion layer (m), T_{GDL} is the gas diffusion layer temperature (K), $\dot{N}_{GDL,x}$ is the gas molar flow rate of specie x (mol/s), A_{GDL} is the gas diffusion layer area (m^2), $D^{eff}_{GDL,x-y}$ is the gas diffusion coefficient (m^2/s) between the species x and y can be calculated from [22]:

$$D^{eff}_{GDL,x-y} = \frac{1}{P_{tot}} \cdot a \cdot \left(\frac{T_{GDL}}{\sqrt{T_{crit,x} T_{crit,y}}} \right)^b \cdot \left(P_{crit,x} P_{crit,y} \right)^{\frac{1}{3}} \cdot \left(T_{crit,x} T_{crit,y} \right)^{\frac{12}{5}} \cdot \left(\frac{10^{-3}}{M_x} + \frac{10^{-3}}{M_y} \right)^{\frac{1}{2}} \cdot \varepsilon^{\iota} \quad (1.23)$$

where P_{tot} is the total pressure of species (atm), T_{crit} is the critical temperature of species (K), P_{crit} is the critical pressure of species (atm), and M is the molar mass of species (kg/mol), ε is the porosity of the GDL and ι is the GDL tortuosity. The coefficients a and b depend on whether one of the species is a polar gas or not and are determined accordingly, which are given as follows [22]:

For pair of gases contains no polar gas:

$$a = 2.745 \times 10^{-4} \; and \; b = 1.823$$

For pair of gases contains polar gas:

$$a = 3.640 \times 10^{-4} \; and \; b = 2.334$$

1.2.2.4 Catalyst Layers

As mentioned before, the reactant gas mass flow rate through the GDL to the catalyst layer is directly proportional to the fuel cell stack current [23] [24]. Thus, the oxygen mass flow q_{O_2} (kg/s)at the cathode side can be expressed by:

$$q_{O_2} = \frac{M_{O_2} \cdot i}{4F} \tag{1.24}$$

the hydrogen mass flow q_{H_2} (kg/s)at the anode side can be expressed by:

$$q_{H_2} = \frac{M_{H_2} \cdot i}{2F} \tag{1.25}$$

and the mass flow of produced water q_{H_2O} (kg/s) at the cathode side due to the electrochemical reaction can be calculated by:

$$q_{H_2O,pro} = \frac{M_{H_2O} \cdot i}{4F} \tag{1.26}$$

1.2.2.5 Dynamic Membrane Water Content

Because the membrane ionic conductivity σ_{mem} is highly dependent on water content λ_w in polymer membrane [25], a more detailed knowledge of transient behavior of the λ_m would give a more accurate value of Ohmic losses η_{ohmic}, as shown in the equation 1.3. Moreover, the dynamic phenomena of λ_w plays an important role on the dynamic performance of PEM fuel cell due to its relatively long transient time (up to some minutes) [26].

The dynamics of the membrane water content λ_w is generally influenced by two water flow effects in the membrane: the electro-osmotic drag flow due to proton conduction from the anode to the cathode; the water back diffusion flow caused by the concentration gradient between anode and cathode side. The membrane water content λ_w is defined as the relationship of the number of water molecules per charged site (sulphonate site) [27]:

$$\lambda_w = \begin{cases} 0.0043 + 17.81\alpha_{H_2O} - 39.85\alpha_{H_2O}^2 + 36\alpha_{H_2O}^3 & if\ 0 < \alpha_{H_2O} \leq 1 \\ 14 + 1.4(\alpha_{H_2O} - 1) & if\ 1 < \alpha_{H_2O} \leq 3 \end{cases} \tag{1.27}$$

where α_{H_2O} is the water activity factor, which can be obtained based on the water local vapor partial pressure P_{H_2O} (pa), and the local vapor saturation pressure P_{sat} (pa):

$$\alpha_{H_2O} = \frac{P_{H_2O}}{P_{sat}} \tag{1.28}$$

where the local vapor saturation pressure P_{sat} is calculated by:

$$log_{10}\left(\frac{P_{sat}}{10^5}\right) = -2.1794 + 0.02953(T_{vapor} - 273.15) - 9.1837 \times 10^{-5}(T_{vapor} - 273.15)^2 + 1{,}4454 \times 10^{-7}(T_{vapor} - 273.15)^3 \tag{1.29}$$

where T_{vapor} is the vapor temperature (K). Thus, the dynamics of the water content λ_w in the membrane can be obtained by considering the water molar flows balance at two sides (i.e. anode and cathode) of membrane, and the mass conservation of water, as shown in Figure 1.2.

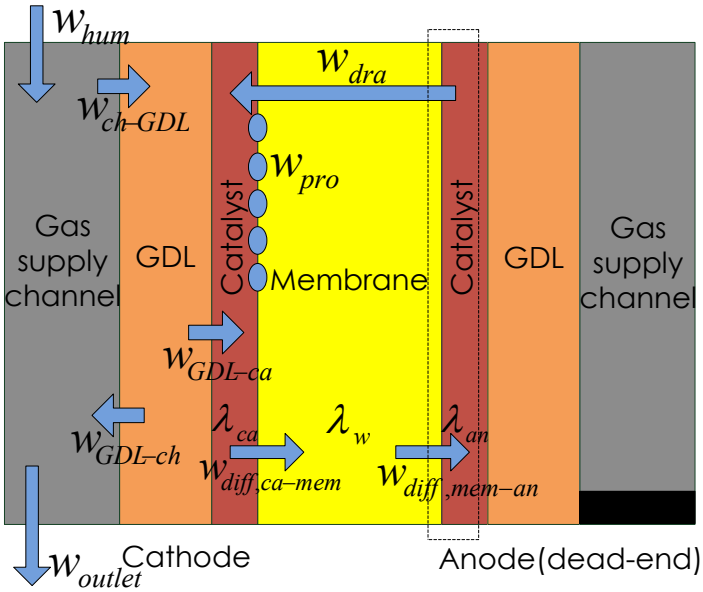

Figure 1.2 Dynamic water flow behaviors in fuel cell membrane.

Thus, the dynamics of the water content λ_w can be described by:

$$\frac{A_{mem}\delta_{mem}\rho_{dry,mem}}{M_{mem}}\frac{d\lambda_w}{dt} = W_{dra,an} - W_{dra,ca} + W_{diff,\mathrm{ca-mem}} - W_{diff,mem-ca} \tag{1.30}$$

where $\rho_{dry,mem}$ is the membrane dry density (kg/m^3), M_{mem} is the molecular mass of membrane (kg/mol), and W represents different water molar flow (mol/s) entering or leaving the membrane due to electro-osmotic drag and water back diffusion flow.

The water molar entering or leaving the membrane due to electro-osmotic drag W_{dra} can be described by:

$$W_{dra} = \frac{\lambda_w i}{22F} \cdot n_{drag}^{SAT} \tag{1.31}$$

where the $n_{drag}^{SAT} \approx 2.5$ is the coefficient of electro-osmotic drag for maximum hydration conditions. The water molar entering (from cathode to membrane) or leaving (from membrane to anode) the membrane $W_{diff,i}$ due to back diffusion flow can be described by [28]:

$$\begin{cases} W_{diff,ca-mem} = \dfrac{A_{mem} D_{water} \rho_{dry,mem} |\lambda_{ca} - \lambda_w|}{M_{mem} \delta_{mem}} \\ W_{diff,mem-an} = \dfrac{A_{mem} D_{water} \rho_{dry,mem} |\lambda_w - \lambda_{an}|}{M_{mem} \delta_{mem}} \end{cases} \tag{1.32}$$

where $\rho_{dry,mem}$ is the dry density of the membrane (kg/m^3), M_{mem} is the equivalent mass of the membrane (kg/mol). The boundary water content λ_i at anode and cathode side can be expressed as a function of water activity α_i which can be deduced from the water vapor partial pressure equation 1.28. The membrane water diffusion coefficient D_{water} (m^2/s) can be calculated from the empirical equations [28]:

$$D_{water}(\lambda_w) = \begin{cases} 10^{-10} e^{\left(2416\left(\frac{1}{303} - \frac{1}{T_{mem}}\right)\right)} & if \quad \lambda_w < 2 \\ 10^{-10}\left(1 + 2(\lambda_w - 2)\right) & if \quad 2 \le \lambda_w \le 3 \\ 10^{-10}\left(3 - 1.67(\lambda_w - 3)\right) & if \quad 3 \le \lambda_w \le 4.5 \\ 1.25 \times 10^{-10} & if \quad \lambda_w > 4.5 \end{cases} \tag{1.33}$$

As shown in Figure 1.2, in the case of non-humidified hydrogen supply and anode dead-end mode operation, the anode side water accumulation is only caused by the water diffusion from the membrane to the anode $W_{diff,mem-an}$, and the cathode side water accumulation depends on three factors: W_{GDL-ca} comes from humidified air supply at cathode W_{hum}, the produced water at cathode side W_{pro} during electrochemical reaction and the electro-osmotic drag flow from the anode to the cathode W_{dra}.

Under the dead-end mode operation (no water accumulation at anode side), the water molar flow entering into the membrane from anode due to electro-osmotic drag $W_{dra,an}$ is equal to the water molar flow leaving out the membrane to anode due to back-diffusion $W_{diff,mem-an}$ (dashed portion as shown in figure 1.2). Thus, the dynamics of the membrane water content λ_w can thus be simplified by:

$$\frac{A_{mem} \delta_{mem} \rho_{dry,mem}}{M_{mem}} \frac{d\lambda_w}{dt} = \frac{A_{mem} D_{water} \rho_{dry,mem} (\lambda_{ca} - \lambda_w)}{M_{mem} \delta_{mem}} - \frac{\lambda_w i}{22F} \cdot n_{drag}^{SAT} \tag{1.34}$$

with anode side water content λ_{an}:

$$\lambda_{an} = \lambda_w - \frac{\lambda_w i \cdot n_{drag}^{SAT} \; M_{mem} \delta_{mem}}{22F \cdot A_{mem} D_{water} \rho_{dry,mem}} \tag{1.35}$$

1.2.3 Thermal Domain Modeling

In addition to the fluidic phenomena, the effect of temperature on the fuel cell performance should also be considered in the fuel cell modeling. For example, the heat transfer changes the gas convection and diffusion behaviors, and further influences the electrochemical quantities inside the fuel cell.

The fuel cell temperature transient behavior in the thermal domain is due to the heat generation and thermal conduction and convection phenomena. Like dynamic behavior of membrane water content, dynamics of fuel cell temperature is an important phenomenon due to its relatively long transient time. This dynamic behavior can be generally described as follows:

$$\rho V C_p \frac{dT_{CV}}{dt} = \dot{Q}_{cond} + \dot{Q}_{mass} + \dot{Q}_{forced\_conv} + \dot{Q}_{source} \tag{1.36}$$

where ρ is the mean layer volume density of stack (kg/m^3), V is the layer volume of stack (m^3), C_p is the layer thermal capacity (J/kg·K), T_{CV} is the temperature (K) of each control volume and $\dot{Q}$ stands for the different types of heat (J) flows entering or leaving the layer respectively: conduction, convective flow, forced convection and internal heat sources.

The heat flows due to conduction can be expressed according to Fourier's law [29]:

$$\dot{Q}_{cond} = \frac{2\lambda_{CV} S_{section,CV}}{\delta_{CV}} \left(T_{boundary} - T_{CV}\right) \tag{1.37}$$

where λ_{CV} is the control volume thermal conductivity (W/m·K), $S_{section,CV}$ is the section of the control volume in heat transfer direction (m^2), and δ_{CV} is the control volume thickness (m).

The convective heat flow due to the mass transfer entering or leaving the control volume can be calculated by

$$\dot{Q}_{mass} = \left[\sum_{specie} \left(q_{specie} C_{p,specie}\right)\right] \left(T_{boundary} - T_{CV}\right) \tag{1.38}$$

where q_{specie} is the mass flow rate (kg/s).

The heat transfers by forced convection $\dot{Q}_{forced\_conv}$ can be written according to Newton's cooling law:

$$\dot{Q}_{forced\_conv} = h_{forced} S_{forced} (T_{cool} - T_{cell}) \tag{1.39}$$

where T_{cool} is the coolant temperature and S_{forced} is the contact area (m^2), h_{forced} is the forced convection heat transfer coefficient (W/m^2·K), which can be calculated by [29]:

$$h_{forced} = \frac{Nu \lambda_{CV}}{D_{hydro}} \tag{1.40}$$

where λ_{CV} is the fluid thermal conductivity, Nu is the Nusselt number of the fluid, which can be calculated by the empirical equations [30]:

$$Nu = 3.657 + \frac{0.0677 \cdot (Re \cdot \frac{C_{p,fluid}\mu}{\lambda_{CV}} \frac{D_{hydro}}{L})}{1 + 0.1 \cdot \frac{C_{p,fluid}\mu}{\lambda_{CV}} \cdot (Re \cdot \frac{D_{hydro}}{L})} \quad (1.41)$$

Where $C_{p,fluid}$ is the coolant thermal capacity (J/kg·K).

At last, the linear expression of the heat sources $\dot{Q}_{source}$ as a function of the cell temperature can be obtained:

$$\dot{Q}_{source} = k_{source} T_{cell} + i\eta_{act} + 4.2 i^2 k_{mem} \quad (1.42)$$

1.3 Multi-Dimensional Modeling Considerations

Compared with 1-D models [31]-[39], a 2-D PEMFC model has a capability to provide two-dimensional behaviors, which is very useful for spatial non-uniformity and control coupling analysis. This analysis can give detailed and valuable spatial physical quantity information under different fuel cell operation conditions by taking multiple spatial dimensions into consideration. For example to prevent local "hotspot" on electrode due to non-homogeneous distribution of reactants, and can be further employed in a model-based real-time controller.

Many PEMFC 2-D models have been previously proposed in the literature [40]-[45]. However, a common drawback of these works is that the presented fuel cell bipolar plate flow field (gas channels) models are over-simplified (or not even considered). Thus they cannot accurately describe the non-linear and non-uniform pressure distribution characteristics.

For example, as shown in the upper part of figure 1.3, the gas pressure prediction results of a model without the consideration of channel geometric form, could lead to an inaccurate gas diffusion phenomenon in the serpentine pipeline, which would further impact the accuracy of electrode current density analysis. In these models, the gas supply channel is assumed to be straight and single. In fact, the gas supply pipeline in the anode and cathode sides have different geometric patterns, as shown in the figure 1.4.

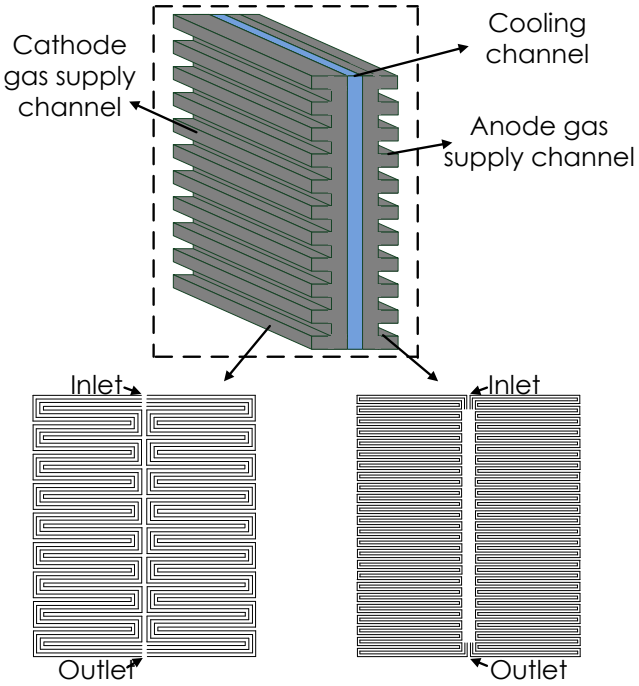

Figure 1.3 Double three-parallel serpentine pattern of cathode gas supply channel and double single serpentine pattern of anode gas supply channel

It can be seen from the figure 1.4 that, the flow field forms of a Ballard NEXA 1.2kW fuel cell stack used in this thesis includes a single serpentine pipeline in anode side and a parallel serpentine pipeline in cathode side. Therefore, a comprehensive representation of non-homogeneous gas phenomenon by fully taking the geometric form of the fuel cell pipeline into consideration is particularly useful to achieve highly accurate spatial distribution information for 2-D model of PEMFC.

Figure 1.4 Actual geometry form of gas channel of NEXA PEMFC: the left one is cathode air channel, the right one is anode hydrogen gas channel

In this section, a 2-D, multi-physical PEMFC model is fully developed, which covers fluidic and electric domains with an innovative 2-dimensional modeling approach. The basis of individual layers in a single cell of the proposed 2-D PEMFC model is shown in the figure 1.5.

It can be seen from the figure 1.5 that, in the proposed 2-D PEMFC model, a single cell model consists of 7 individual layers: 1) cathode gas supply channel; 2) cathode gas diffusion layer (GDL); 3) cathode catalyst layer; 4) membrane; 5) anode catalyst layer; 6) anode gas diffusion layer (GDL); 7) anode gas supply channel.

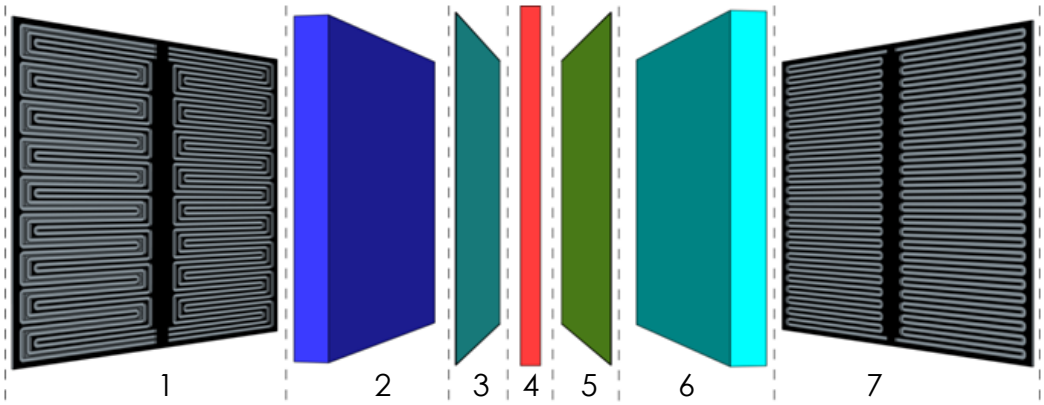

Figure 1.5 Structure of a single cell of fuel cell stack.

In order to take the geometric form of the fuel cell pipeline into consideration, a 2-D modeling of fluidic domain is developed firstly, followed by a 2-D electric modeling.

1.3.1 Two-Dimensional Approach in Fluidic Model

To accurately model the reactant gas pressure distribution on the electrodes surface, a comprehensive modeling of gas convection-diffusion phenomena in the gas supply channel and GDL is presented hereafter by precisely considering the fuel cell gas channel geometric form in this section.

1.3.1.1 Gas Supply Channels

Different from single and straight channel assumption in the previously developed PEMFC model, the geometric patterns of gas supply channels (both anode and cathode sides) are now considered in the improved model, such as single serpentine, parallel serpentine channels, with the consideration of sharp and curved U-bends (channel angles). Under the same inlet air supply conditions, the gas pressure distribution on the surface of GDL depends highly on the flow field form. Thus, a detailed

representation of non-homogeneous gas pressure distribution by considering the flow field form can be very useful to achieve accurate modeling results.

In this thesis, the geometric form of gas supply channels is taken from Ballard NEXA fuel cell as shown in figure 1.6. This two-sided design includes a three-parallel serpentine channel for cathode air supply, and a single serpentine pattern channel for anode hydrogen supply.

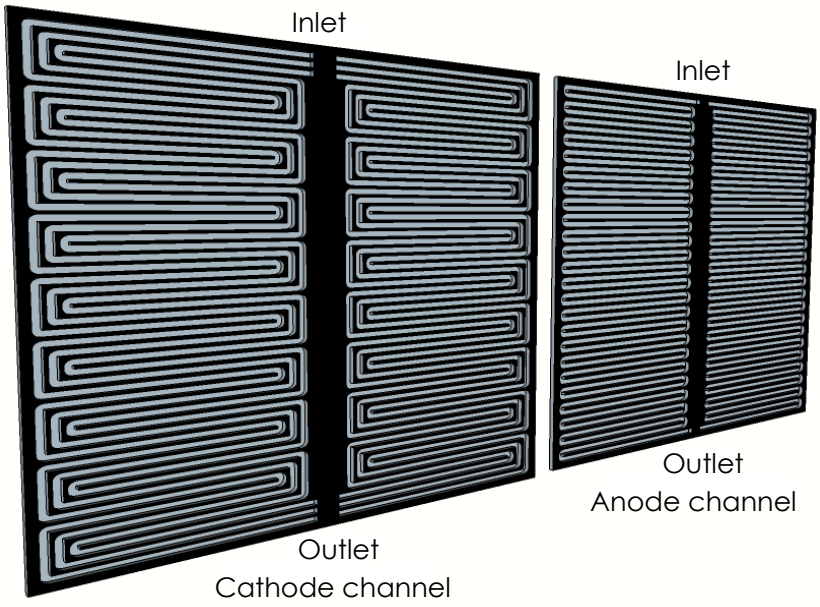

Figure 1.6 Three-parallel serpentine channel for cathode air supply; and single serpentine channel for anode hydrogen supply.

The gas pressure drop ΔP_{ch} of serpentine channel depends on three factors [46] [47]: the surface friction losses of straight pipeline (modeled by the Darcy–Weisbach equation), the frictional loss suffered in the elongated section of the bends, and the sum of excess loss coefficients ε_i for *n* U-bends:

$$\Delta P_{ch} = f_D \frac{\rho_{gas} L_{ch} u^2}{2 D_{hydro}} + \frac{1}{2} \rho_{gas} u^2 \left(4 f_f \frac{L_{bend}}{D_{hydro}} + \sum_{i=1}^{n} \varepsilon_i \right) \tag{1.43}$$

where f_D is the Darcy friction factor, ρ_{gas} is the fluid density in the channel (kg/m^3), L_{ch} is the total length of straight channel (m), u is the mean fluid velocity in the channel (m/s), D_{hydro} is the hydraulic diameter of the channel (m), L_{bend} is the total length of elongated section of the bends (m), the Kays friction factor f_f can be given by [46]:

$$f_f \cdot Re = 13.84 + 10.38 exp\left(\frac{-3.4}{\alpha_{bend}}\right) \tag{1.44}$$

where w is the pipeline width (m), h is the pipeline thickness (m). Re is the Reynolds number of the fluid in the channels, channel aspect ratio α_{bend} is defined by:

$$\alpha_{bend} = \frac{w_{ch}}{h_{ch}} \tag{1.45}$$

The excess bend loss coefficient of *i* th bend ε_i is given by [46]:

$if\ Re < 100$

$$\varepsilon_i = 0 \tag{1.46a}$$

$if\ 100 < Re < 1000$

$$\varepsilon_i = 0.46\left(Re^{\frac{1}{3}}\right) \times (1 - 0.18C + 0.016C^2) \times (1 - 0.2\alpha + 0.0022\alpha^2) \times \left(1 + 0.26\left(\frac{L_s}{D_{hydro}}\right)^{\frac{2}{3}} - 0.0018\left(\frac{L_s}{D_{hydro}}\right)^2\right) \tag{1.46b}$$

$if\ 1000 < Re < 2200$

$$\varepsilon_i = 3.8(1 - 0.22C + 0.022C^2)(1 - 0.1\alpha + 0.0063\alpha^2) \times \left(1 + 0.12\left(\frac{L_s}{D_{hydro}}\right)^{\frac{2}{3}} - 0.0003\left(\frac{L_s}{D_{hydro}}\right)^2\right) \tag{1.46c}$$

where L_s is the spacer length between two neighboring duct, and C is the curvature ratio of the bend, is given by [46]:

$$C = \frac{R_C}{D_{hydro}} \tag{1.47}$$

where R_C is the mean radius of bends, D_{hydro} is the duct hydraulic diameter which is calculated by:

$$D_{hydro} = \frac{4wh}{2(w + h)} \tag{1.48}$$

where the pipeline width w, pipeline thickness h, and spacer length between two neighboring duct L_s can be seen clearly in the figure 1.7.

From figure 1.7, the rectangle pane is represented as the cross sectional area of pipeline. The anode channel curved U-bends are the same as those in the cathode channel.

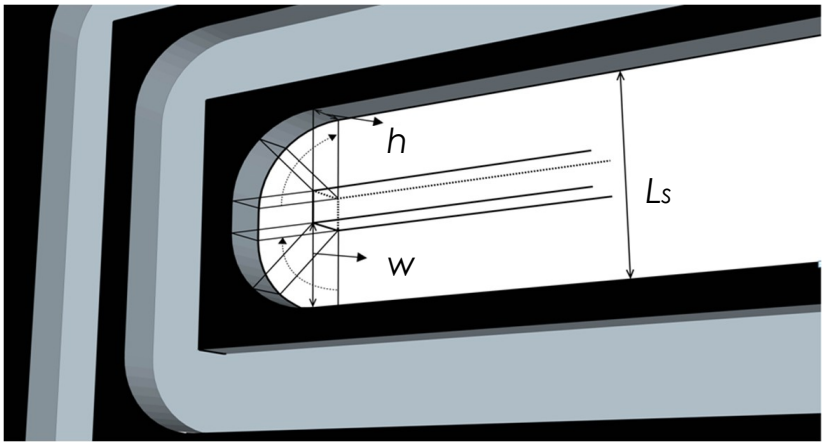

Figure 1.7 Schematic diagram of pipeline width w, pipeline thickness h and spacer length between two neighboring duct L_s in the channel curved U-bends.

1.3.1.2 Gas Diffusion Layer

The modeling equations for reactant gas diffusion phenomena in the GDL are described in this section. Based on the gas supply channel geometry, the GDL, which is directly adjacent to the gas channels layer, can be divided into two sections, denoted as "fluid adjacent volume" and "solid adjacent volume", as illustrated in figure 1.8. From figure 1.8, the thin line GDL control volume is adjacent to the channel fluidic section, denoted as "fluid adjacent volumes" of GDL. The gas flows to a "fluid adjacent volumes" come from the gas channel pipeline and the adjacent volumes. In contrast, the bold line GDL control volumes in figure 1.8 are adjacent to the channel solid section, denoted as "solid adjacent volume" of GDL. The gas flows to a "solid adjacent volume" come only from the adjacent volumes in gas diffusion layer.

In the previous section, the gas convection phenomenon in the serpentine pipeline has been well developed. As shown in the figure 1.8, the convective gas flow direction in the gas pipeline is marked by arrow 1 in the gas pipeline A, and by arrow 3 in the gas pipeline B. Then, the gas diffusion phenomena through the GDL can be divided into six categories:

1) Diffusion from pipeline to "fluid adjacent volume" (z-axis, marked with arrows 2 and 4);

2) Diffusion between two adjacent "fluid adjacent volumes" (y-axis, marked with arrows 5 and 6);

3) Diffusion between adjacent "fluid adjacent volume" and "solid adjacent volume" (x-axis, marked with arrow 7).

4) Diffusion between two adjacent "solid adjacent volume" (y-axis, marked with arrow 8);

5) Diffusion from "fluid adjacent volumes" to catalyst layer (z-axis, marked with arrows 9 and 10);

6) Diffusion from "solid adjacent volume" to catalyst layer (z-axis, marked with arrow 11).

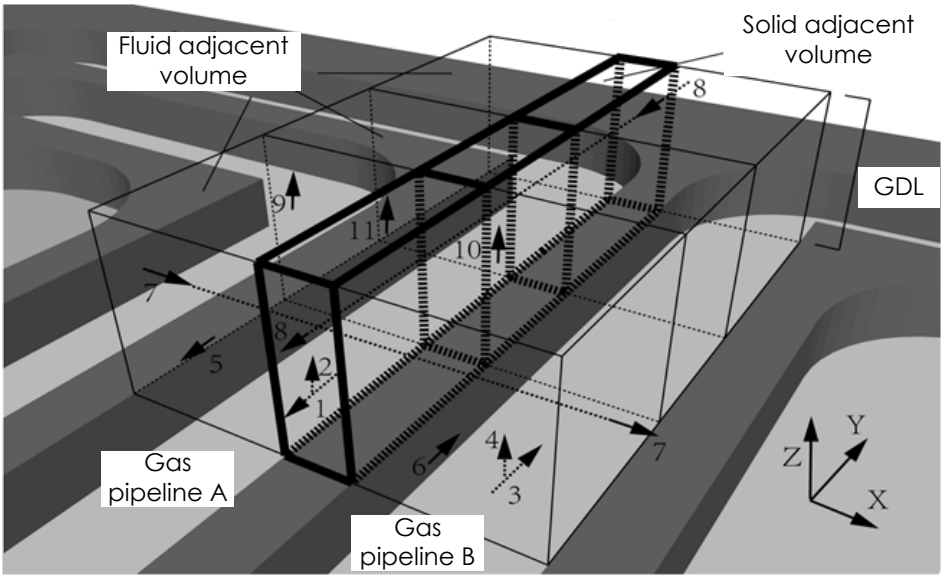

Figure 1.8 Gas diffusion phenomena in the GDL.

It should be noted that, when the stack current increases, the diffusion from gas pipeline to "fluid adjacent volume", and the diffusion from volumes to catalyst layer become more important due to the increase of mass flow from gas channels to the catalyst layer, which is proportional to the fuel cell current. All these diffusion phenomena in the gas diffusion layer, except the above-mentioned current-driven ones, can be modeled by the modified Fick's diffusion equation 1.22.

In fact, the benefit of parallel pipeline is its lower pressure drop due to shorter single channel length. However its main drawback is water droplet accumulation during fuel cell operation. The single serpentine can improve water removal while introduce a larger pressure drop. This parallel serpentine flow field combines thus the advantages of both patterns, in order to achieve better performance of fuel cell system.

1.3.1.3 Non-Uniform Control Volume Consideration

In order to fully describe the gas flow in the serpentine pipeline gas channels, and further accurately obtain the two-dimensional physical quantity distribution both in fluidic

domain and electrochemical domain, the control volume mesh grid definition of gas channels in the proposed 2-D PEMFC model is considered in a non-uniform manner. It means that, the geometry form of each control volume follows the channel geometric patterns. The 2-D channel model can be then implemented by defined control volumes with the physical equations presented in the previous section. The control volume 2-D mesh grid at both cathode and anode sides are depicted in the following figure 1.9.

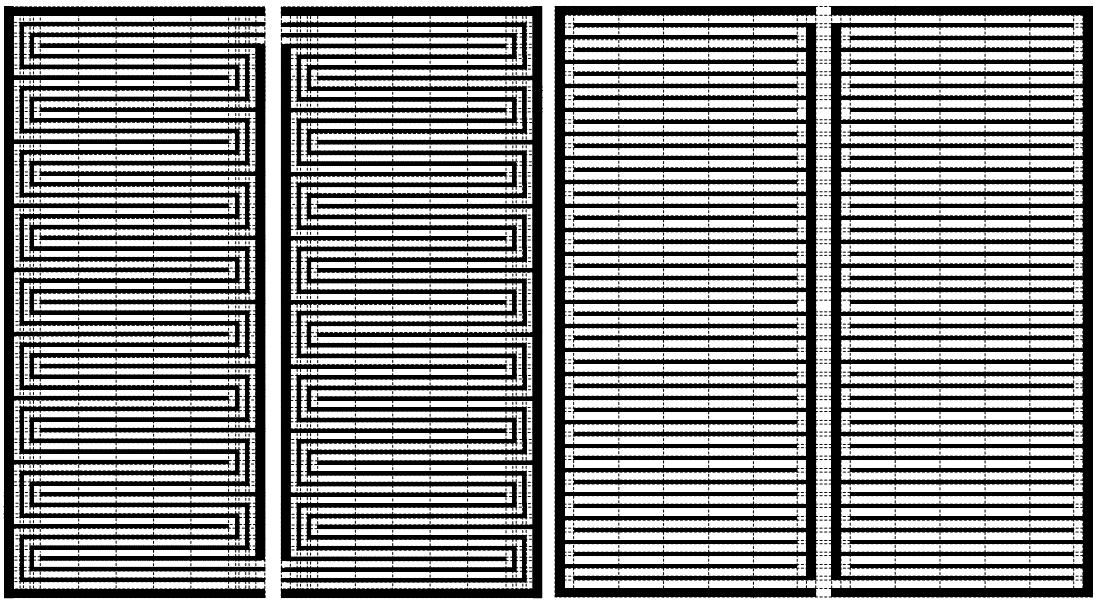

Figure 1.9 Control volumes 2-D mesh grid at cathode/anode sides.

As shown in the figure 1.9, the two surface dimensions are considered for the proposed 2-D model, the non-uniform control volume distribution of each side is based on the geometry form of channels (i.e. three-parallel serpentine pattern at cathode side and single-parallel serpentine pattern at anode side, denoted by black mesh in the figure 1.9.

1.3.2 Two-Dimensional Approach in Electric Model

The characteristics of reactant gas convection and diffusion in the pipeline and gas diffusion layer are fully described in the previous section. However, the spatial physical quantity distribution on the surface of electrode (e.g. the current density distribution) cannot be directly obtained using the non-uniform mesh grid. In order to unify the mesh segments distribution in homogenous material such as electrode and electrolyte, the non-uniform mesh grid of gas channels layer of each side are then linearly converted to uniform mesh grid for GDL and membrane layers denoted by red mesh in the figure 1.10.

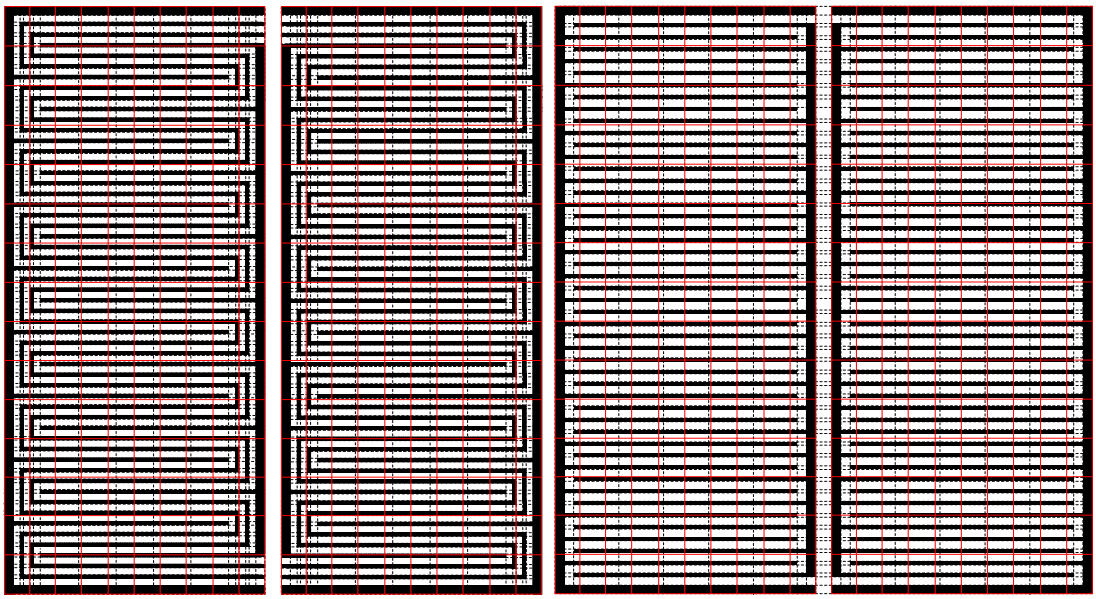

Figure 1.10 Control volumes 2-D mesh grid at cathode/anode sides, and uniform segments for electrochemical calculation

1.4 Conclusion

In this section, a dynamic, multi-physical model of a proton exchange membrane fuel cell is developed at first. The presented model considers in particular the transient phenomena in both fluidic and thermal domains (please refer to the previous work [9] [10]).

Based on the developed multi-physical model, a 2-D modeling approach for a proton-exchange-membrane fuel cell (PEMFC) is then proposed. The proposed model covers multi-physical domains for both fluidic and electric features. In order to accurately describe the characteristics of reactant gas convection and diffusion in the pipeline and gas diffusion layer, the gas pressure drop in the serpentine pipelines is comprehensively analyzed, especially for the reactant gas pressure drop due to the pipeline U-bends, followed by a comprehensive description of gas diffusion layer 2-D modeling by fully considering the geometric form of flow field [48]. The experimental validation and coupling effects analysis are presented in the following chapter.

1.5 Reference

[1] S. Park, S. Choe, "Dynamic modeling and analysis of a 20-cell PEM fuel cell stack considering temperature and two-phase effects," *J. Power Sources*, vol. 179, pp. 660–672, 2008.

[2] Z. Zhang, X. Huang, J. Jiang, B. Wu, "An improved dynamic model considering effects of temperature and equivalent internal resistance for PEM fuel cell power modules," *J. Power Sources*, vol. 161, pp. 1062–1068, 2006.

[3] K. Sedghisigarchi and A. Feliachi, "Dynamic and transient analysis of power distribution systems with fuel Cells-part I: fuel-cell dynamic model," *IEEE Trans. Energy Convers.*, vol. 19, no. 2, pp. 423–428, Jun. 2004.

[4] F. Gao, B. Blunier, D. Chrenko, D. Bouquain, and A. Miraoui, "Multirate fuel cell emulation with spatial reduced real-time fuel cell modeling," *IEEE Trans. Ind. App.*, vol. 48, pp. 1127–1135, Jul. 2012.

[5] Y. Shan, S. Choe, S. Choi, "Unsteady 2D PEM fuel cell modeling for a stack emphasizing thermal effects," *J. Power Sources*, vol. 165, pp. 196-209, 2007.

[6] X. Wang, J. Xu, D. Lee, "Parameter sensitivity examination for a complete three-dimensional, two-phase, non-isothermal model of polymer electrolyte membrane fuel cell," *Int. J. Hydrogen Energy*, vol. 37, no. 20, pp. 15766–15777, 2012.

[7] S. um, C. Yang and K. Chen, "Computational Fluid Dynamics Modeling of Proton Exchange Membrane Fuel Cells," *J. Electrochem. Soc.*, vol. 147, no. 12, pp. 4485-4493, 2000.

[8] B. R. Sivertsen, N. Djilali, "CFD-based modelling of proton exchange membrane fuel cells," *J. Power Sources*, vol. 141, no. 1, pp. 65-78, Feb. 2005.

[9] D. Zhou, F. Gao, E. Breaz, A. Ravey, A. Miraoui, K. Zhang, "Dynamic phenomena coupling analysis and modeling of PEMFCs," *IEEE Trans. Energy Convers.*, vol. 31, no. 4, pp. 1399–1412, Dec. 2016.

[10] D. Zhou, K. Zhang, A. Ravey, F. Gao, A. Miraoui, "Dynamic variable coupling analysis and modeling of proton exchange membrane fuel cells for water and thermal management," *IEEE Applied Power Electronics Conference and Exposition (APEC)*, Long Beach, CA, Mar. 20-24, 2016.

[11] J. Larminie, A. Dicks. *Fuel cell systems explained*. 2nd ed. USA: Wiley, 2012.

[12] T. Springer, T. Zawodzinski T, S. Gottesfeld, "Polymer electrolyte fuel cell model," *J. Electroanal. Chem.* vol. 138, pp. 2334-2342, 1991.

[13] D. Zhou, A. Ravey, F. Gao, A. Miraoui, and K. Zhang, "On-Line Estimation of Lithium Polymer Batteries State-of-Charge Using Particle Filter Based Data Fusion with Multi-Models Approach," in *Proc. IEEE IAS*, Oct. 18-22, pp. 1-8, 2015.

[14] D. Noren, M. Hoffman, "Clarifying the Butler–Volmer equation and related approximations for calculating activation losses in solid oxide fuel cell models," *J. Power Sources*, vol. 152, pp. 175-181, 2005.

[15] D. Zhao, M. Dou, D. Zhou, and F. Gao, "Study of the modeling parameter effects on the polarization characteristics of the PEM fuel cell," *Int. J. Hydrogen Energy*, vol. 41, no. 47, pp. 22316–22327, 2016.

[16] D. Zhao, F. Gao, P. Massonnat, M. Dou, A. Miraoui, "Parameter Sensitivity Analysis and Local Temperature Distribution Effect for a PEMFC System," *IEEE Trans. Energy Convers.*, vol. 30, no.3, pp. 1008-1018, Mar. 2015.

[17] F. White, *Fluid mechanics*. 4th ed. McGraw Hill, ISBN 0-07-069716-7; 1998.

[18] A. Tang, J. Bao, M. Kazacos, "Studies on pressure losses and flow rate optimization in vanadium redox flow battery," *J. Power Sources*, vol. 248, pp. 154–162, 2014.

[19] J. Park, X. Li, "An experimental and numerical investigation on the cross flow through gas diffusion layer in a PEM fuel cell with a serpentine flow channel," *J. Power Sources*, vol. 163, pp. 853-863, 2007.

[20] A. Bertei, C. Nicolella, "Common inconsistencies in modeling gas transport in porous electrodes: The dusty-gas model and the Fick law," *J. Power Sources*, vol. 279, pp. 133-137, 2015.

[21] N. Legrand, B. Knosp, P. Desprez, F. Lapicque, S. Raël, "Physical characterization of the charging process of a Li-ion battery and prediction of Li plating by electrochemical modeling," *J. Power Sources*, vol. 245, pp. 208-216, 2014.

[22] R. Bird, W. Stewart, E. Lightfoot, *Transport phenomena*. 2nd ed. John Wiley & Sons; 2002.

[23] F. Gao, B. Blunier, D. Bouquain, A.Miraoui, and A. El Moudni, "Polymer electrolyte fuel cell stack emulator for automotive hardware-in-the-loop applications," in *Proc. IEEE VPPC*, Sep. 7-10, pp. 998-1004, 2009.

[24] F. Gao, B. Blunier, M. Simões, A. Miraoui, A. El-Moudni, "PEM fuel cell stack Hardware-In-the-Loop emulation using DC/DC converter design," in *Proc. IEEE EPEC*, Oct. 22-23, pp. 1-6, 2009.

[25] R. O'Hayre, S. Cha, W. Colella, F. Prinz, *Fuel cell fundamentals*. John Wiley & Sons, Inc., 2006.

[26] T. Colinart, A. Chenu, S. Didierjean, O. Lottin, S. Besse, "Experimental study on water transport coefficient in Proton Exchange Membrane Fuel Cell," *J. Power Sources*, vol. 190, pp. 230-240, 2009.

[27] F. Barbir. *PEM fuel cells, theory and practice, sustainable world*. Elsevier Academic Press, ISBN 978-0-12-078142-3.

[28] S. Dutta, S. Shimpalee, J. Van, "Numerical prediction of mass-exchange between cathode and anode channels in a PEM fuel cell," *Int. J. Heat Mass Transfer*, vol. 44, pp. 2024-2029, 2001.

[29] F. Incropera, D. DeWitt, T. Bergman, A. Lavine. *Fundamentals of heat and mass transfer*. 6th ed, vol. 1. Wiley; 2007.

[30] B. Spang. *Correlations for convective heat transfer*. On-line URL, www.cheresources.com; 2008.

[31] C. Restrepo, T. Konjedic, A. Garces, J. Calvente, R. Giral, "Identification of a PEM fuel cell's model parameters by means of an evolution strategy," *IEEE Trans. Ind. Inf.*, vol. 11, no. 2, pp. 548-559, Apr 2015.

[32] G. Park, Z. Gajic, "A Simple Sliding Mode Controller of a Fifth-Order Non-linear PEM Fuel Cell Model," *IEEE Trans. Energy Convers*, vol. 29, no. 1, pp. 65-71, Mar. 2014.

[33] W. Yang, Y. He, Y. Li, "Modeling of dynamic operating behaviors in a liquid-feed direct methanol fuel cell," *Int. J. Hydrogen Energy*, vol. 37, no. 23, pp. 18412-18424, Dec. 2012.

[34] K. Nanaeda, F. Mueller, J. Brouwer, S. Samuelsen, "Dynamic modeling and evaluation of solid oxide fuel cell – combined heat and power system operating strategies," *J. Power Sources*, vol.195, no. 10, pp. 3176-3185, May. 2010.

[35] M. Guarnieri, V. Noto, F. Moro, "A Dynamic Circuit Model of a Small Direct Methanol Fuel Cell for Portable Electronic Devices," *IEEE Trans. Ind. Electron.*, vol. 57, no. 6, pp. 1865-1873, June. 2010.

[36] A.Stefanopoulou, I. Kolmanovsky, B. McCain, "A Dynamic Semi-Analytic Channel-to-Channel Model of Two-Phase Water Distribution for a Unit Fuel Cell," *IEEE Trans. Contr. Syst. Technol.*, vol. 17, no. 5, pp. 1055-1068, Sep. 2009.

[37] A. M. Dhirde, N. V. Dale, H. Salehfar, M. D. Mann, and T. H. Han, "Equivalent electric circuit modeling and performance analysis of a PEM fuel cell stack using impedance spectroscopy," *IEEE Trans. Energy Convers.*, vol. 25, no. 3, pp. 778–786, Sep. 2010.

[38] S. Pasricha, S. Shaw, "A dynamic pem fuel cell model," *IEEE Trans. Energy Convers.*, vol. 21, no. 2, pp. 484–490, Jun. 2006.

[39] S. Pasricha, M. Keppler, S. Shaw, M. Nehrir, "Comparison and identification of static electrical terminal fuel cell models," *IEEE Trans. Energy Convers.*, vol. 22, no. 3, pp. 746–754, Sep. 2007.

[40] R. Methekar, V. Prasad, R. Gudi, "Dynamic analysis and linear control strategies for PEM fuel cell using a distributed parameter model," *J. Power Sources*, vol. 165, pp.152-170, 2007.

[41] M. Mangold, A. Bück, R. Hanke-Rauschenbach, "Passivity based control of a distributed pem fuel cell model," *J. Process Control*, vol. 20, pp. 292–313, 2010.

[42] M. Carnevali, M. Serra, C. Batlle, "Distributed parameter model simulation tool for PEM fuel cells," *Int. J. Hydrogen Energy*, vol. 39, pp. 4044–4052, 2014.

[43] D. Chen, H. Peng, "A Thermodynamic Model of Membrane Humidifiers for PEM Fuel Cell Humidification Control," *J. dyn. syst. meas. control*, vol. 127, no. 3, pp. 424–432, 2005.

[44] A. Weber, J. Newman, "Modeling Transport in Polymer-Electrolyte Fuel Cells," *Chem. Rev.*, vol. 104, no. 10, pp. 4679–4726, 2004.

[45] H. Wu, X. Li and P. Berg, "On the modeling of water transport in polymer electrolyte membrane fuel cells," *Electrochimica Acta*, vol. 54, no. 27, pp. 6913-6927, Nov. 2009.

[46] S. Maharudrayya, S. Jayanti, A.P. Deshpande, "Pressure losses in laminar flow through serpentine channels in fuel cell stacks," *J. Power Sources*, vol. 138, pp. 1-13, 2004

[47] S. Maharudrayya, S. Jayanti, A.P. Deshpande, "Pressure drop and flow distribution in multiple parallel-channel configurations used in proton-exchange membrane fuel cell stacks," *J. Power Sources*, vol. 157, pp. 358-367, 2006.

[48] D. Zhou, F. Gao, E. Breaz, A. Ravey, A. Miraoui, "Development of a multi-physical multidimensional modeling of proton exchange membrane fuel cell," *IEEE Transportation Electrification Conference and Expo*, Dearborn, Jun. 27–29, 2016.

Chapter II: Experimental Validation and Coupling Analysis

This chapter presents the experimental test and simulation in order to validate the proposed 2-D model with a commercial Ballard NEXA 1.2 kW PEMFC stack. With the developed 2-D model, the spatial physical quantity information can be accurately observed and analyzed by taking the multiple spatial dimensions into consideration. These spatial results are very useful to help to quantitatively analyze the coupling effects in different physical domains, and study the influences of model parameters on the fuel cell spatial performance.

2.1 Literature Review

Although the coupling of dynamic phenomena in a fuel cell has an important influence on the control design of fuel cell system, very little information has yet been published in the literature on the analysis of interaction between fuel cell dynamic variables in different physical domains.

Zhao *et al.* [1] present a decoupling control strategy for the strong coupling between mass flow and pressure in centrifugal compressor system, which is a key component for supplying compressed air to the fuel cell cathode channel, but the dynamic phenomena coupling in fuel cell system have not been considered. Cheah *et al.* [2] give a detailed analysis of coupling effects of electro-osmotic drag, water diffusion and interfacial water transport. Carnes *et al.* [3] present a analysis of coupling effect of the water transport within the proton exchange membrane and the partially saturated gas diffusion electrodes. Cao *et al.* [4] propose a single neuron adaptive proportional-integral derivative (PID) feedback controller for a solid oxide fuel cell, which combines the advantages of robust control and PID control, in order to automatically adjust control parameters when system encounters uncertainties and disturbances. However, they only considered the coupling effect of dynamic water transport in fluidic domain without taking the thermal domain dynamics into account.

2.2 Model Experimental Validation and Discussion

A commercial 1.2 kW Ballard NEXA 47 cells stack is used to perform the experimental validation, which is shown in the following figure 2.1. This PEMFC stack is supplied by compressed air and hydrogen.

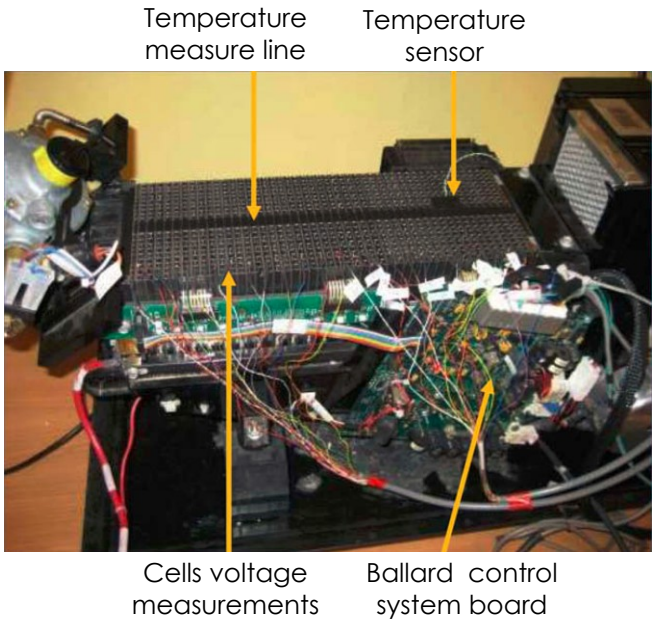

Figure 2.1 Experiment platform: 1.2 kW Ballard NEXA 47 cells PEMFC stack, Ballard control system board, and measurements

During the experiment, the Ballard control system is used to measure most of the experimental data, such as the oxygen flow rate, gas temperature, fuel cell stack current and voltage, etc. The voltage of individual cell is measured by voltage acquisition module of National Instrument. An embedded thermal sensor is used to measure the fuel cell stack temperature.

2.2.1 Experimental Validation of Dynamic Model

Firstly, the comparison of simulation and experimental results of single cell polarization curve are shown in the figure 2.2. It can be seen from the results that, the polarization curve from the proposed model shows an exact conformity with the real PEMFC.

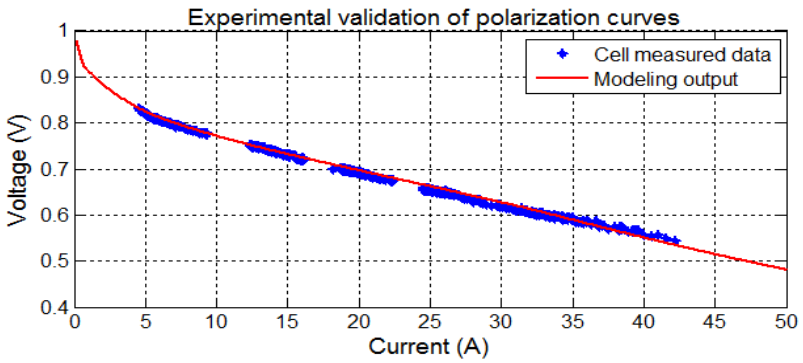

Figure 2.2 Experimental validation of polarization curves.

In order to further validate the presented dynamic fuel cell model through simulation and experiment, different current profiles (static and dynamic) for model validation purpose are presented in figure 2.3.

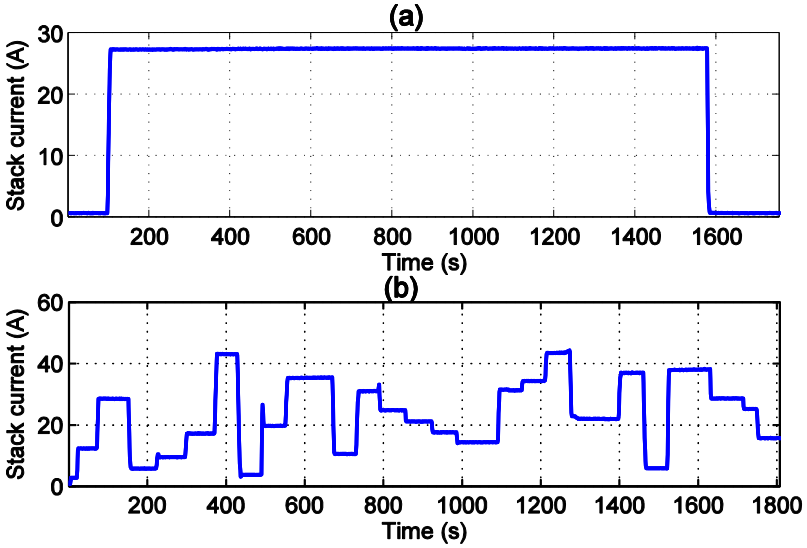

Figure 2.3 Experimental validation under different stack current profile: (a) Long current step. (b) Short current step.

The current profiles (figure 2.3) are applied to the developed model and to the real fuel cell stack. The predicted and measured real stack voltage are compared in figure 2.4.

It can be seen clearly from the figure 2.4 that, the predicted voltage values from the model show a great agreement with the real fuel cell. In addition, the voltage dynamic behavior is also well reproduced by the model. Figure 2.5 shows the simulated and experimental stack temperature during operation, the comparison results show again a good agreement between them.

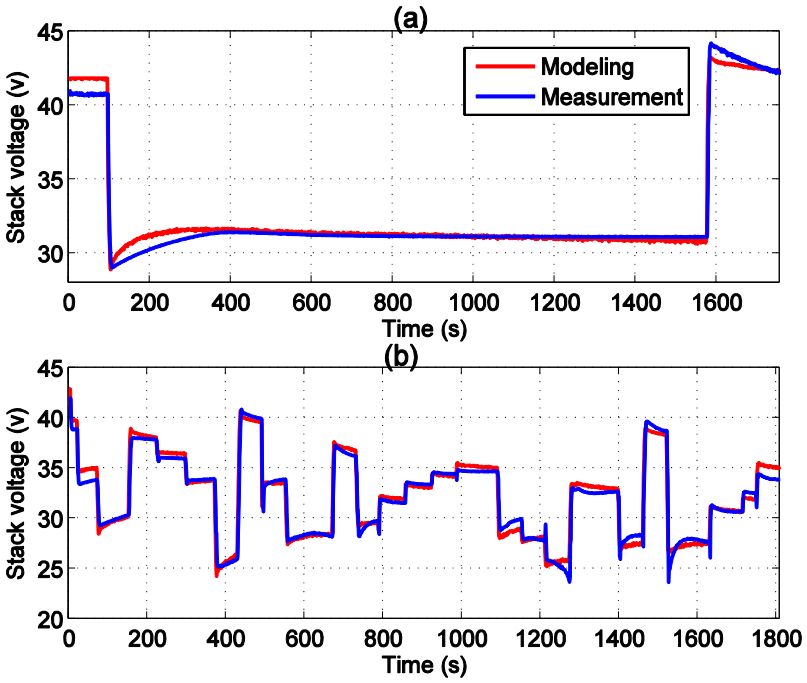

Figure 2.4 Experimental validation of stack voltage with different step current profile: (a) Long current step. (b) Short current step.

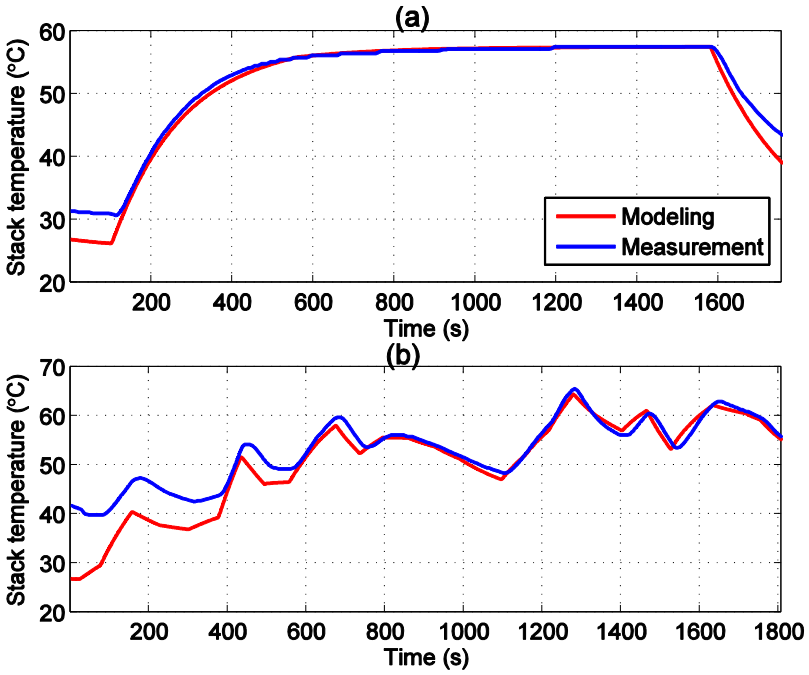

Figure 2.5 Experimental validation of stack temperature with different step current profile: (a) Long current step. (b) Short current step.

2.2.2 Dynamic Membrane Water Content Results and Discussions

The same current profiles (figure 2.3) are applied to the developed model. The model simulation results are shown in figure 2.6. Figure 2.6 (a) shows that the dynamic responses of water content at both cathode, anode sides and in the membrane after the long current step. From figure 2.6 (a), the cathode water content λ_{ca} increases at 100 s, because more water is produced at cathode side at high current. In contrast, the anode water content λ_{an} decreases at 100 s, due to a higher water electro-osmotic drag flow (higher current) from anode to cathode. The green line represents thus membrane average water content λ_w, which depend on the boundary conditions at both cathode and anode sides. The dynamic of membrane Ohmic resistance, which is highly depend on membrane water content based on equation 1.3, is also shown in figure 2.6 (b). It can be seen from the figure that, the transient time of membrane water content, thus the transient of Ohmic resistance, can last about 500 s.

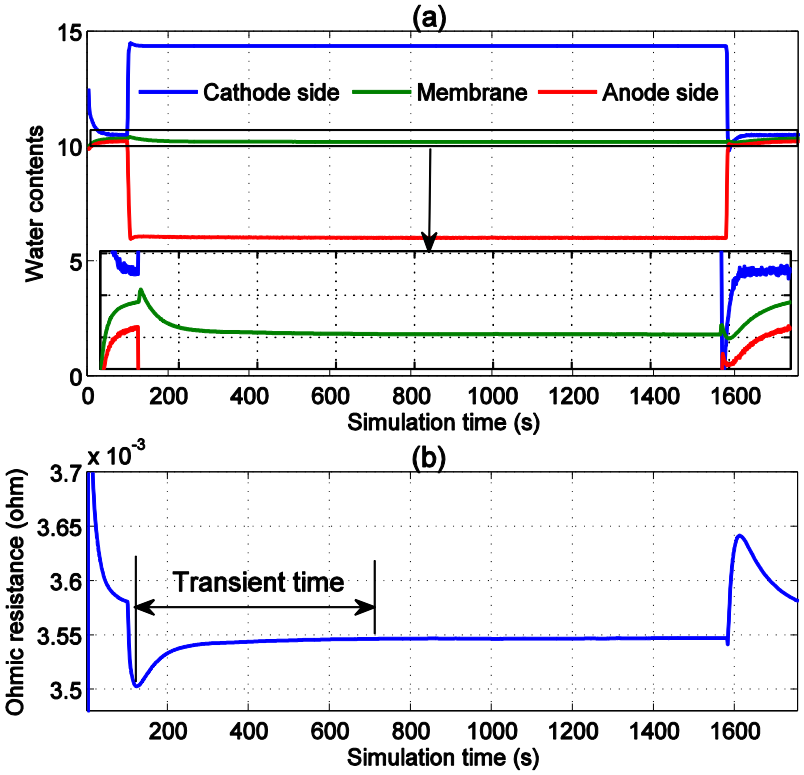

Figure 2.6 Dynamic responses after a current step: (a) Water content. (b) Ohmic resistance.

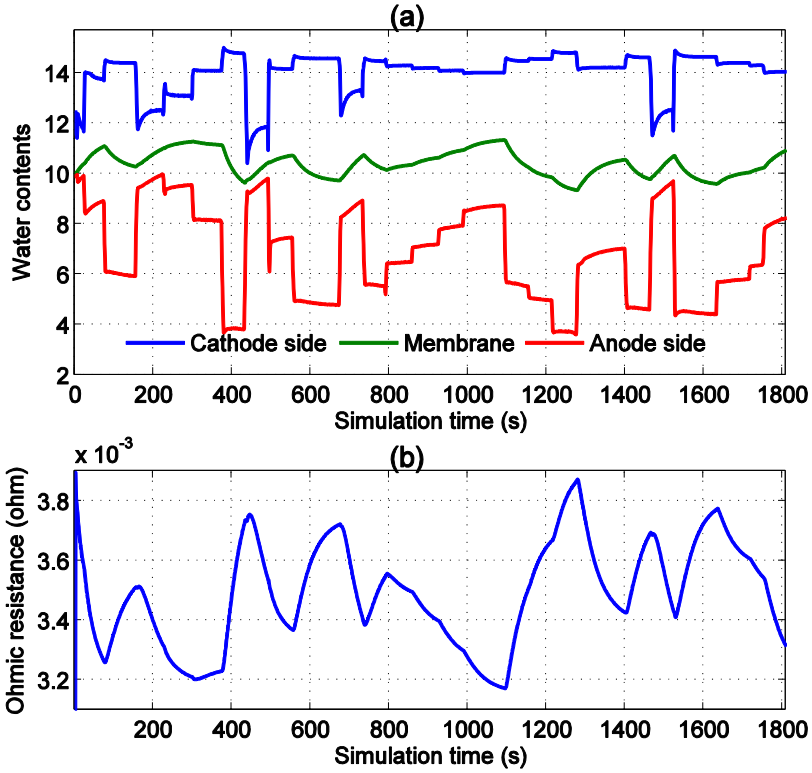

Figure 2.7 Dynamic responses after current step variation: (a) Water content. (b) Ohmic resistance.

Figure 2.7 (a) shows that the dynamic responses to quick current step variation. From figure 2.7 (a), the anode water content λ_{an} decreases sharply at a high current step, due to the high water electro-osmotic drag flow. It can be concluded from the figure that, the dynamic membrane water content λ_w is directly related to the stack current variations. The corresponding dynamic behaviors of Ohmic resistance are shown in figure 2.7 (b).

2.2.3 Effect of the Gas Supply Serpentine Channels and Discussions

The major improvement of gas supply channels modeling by taking the channel geometric form into consideration can give a more accurate pressure distribution prediction in the fuel cell, which can lead to a more precise prediction of fuel cell voltage. A comparison of gas pressure drop in the channel between the developed flow field model and the model using straight channels assumption (as in the most of literature) is given hereafter, in order to highlight the importance of channel geometric form on the pressure modeling accuracy.

Comparison of simulation results of pressure drop in the channels of two modeling approaches with different step current profile are shown in figure 2.8 and figure 2.9.

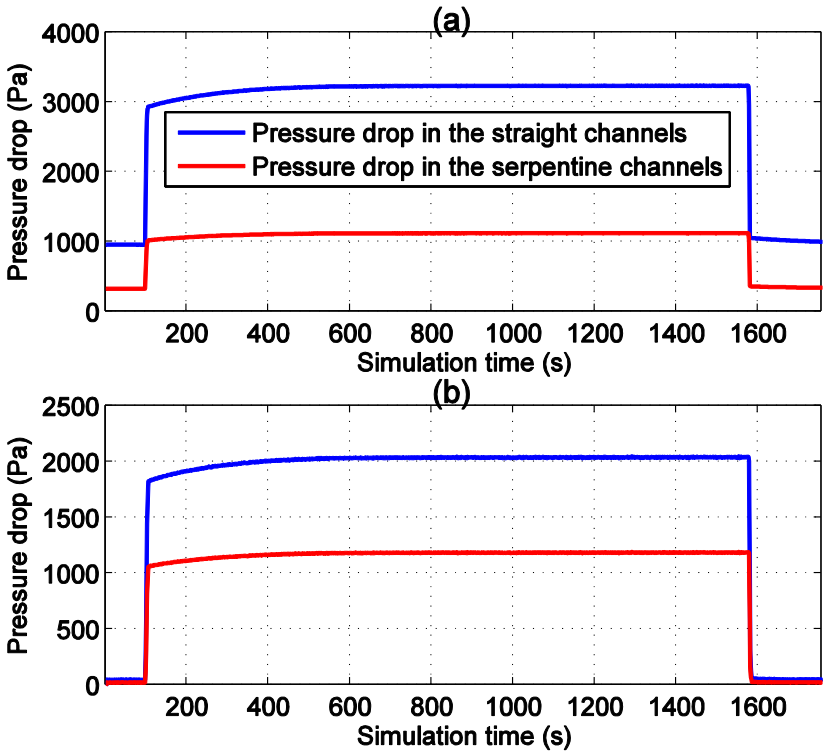

Figure 2.8 Comparison of pressure drop in the channels of two modeling approaches with long step current: (a) Cathode channels. (b) Anode channels.

From figure 2.8 (a), it can be seen clearly from the figure that, the predicted pressure drop is much higher with the assumption of straight gas channel form. By taking the channel geometric form into consideration, the obtained pressure drop in the channel can be differed as much as 2.94 % of total channel pressure compared to the "straight channel" assumption. It has to be noted that, this pressure prediction error would not lead to a significant error in the fuel cell voltage value. However, it could lead to a wrong gas pressure distribution pattern on the surface of electrode for the electrode current density analysis for example. Thus, in order to get a more accurate gas channel pressure results, the channel geometric form has to be taken into account in the fuel cell model. The comparison of simulation results of pressure drop of two modeling approaches with short step current is also presented in figure 2.9.

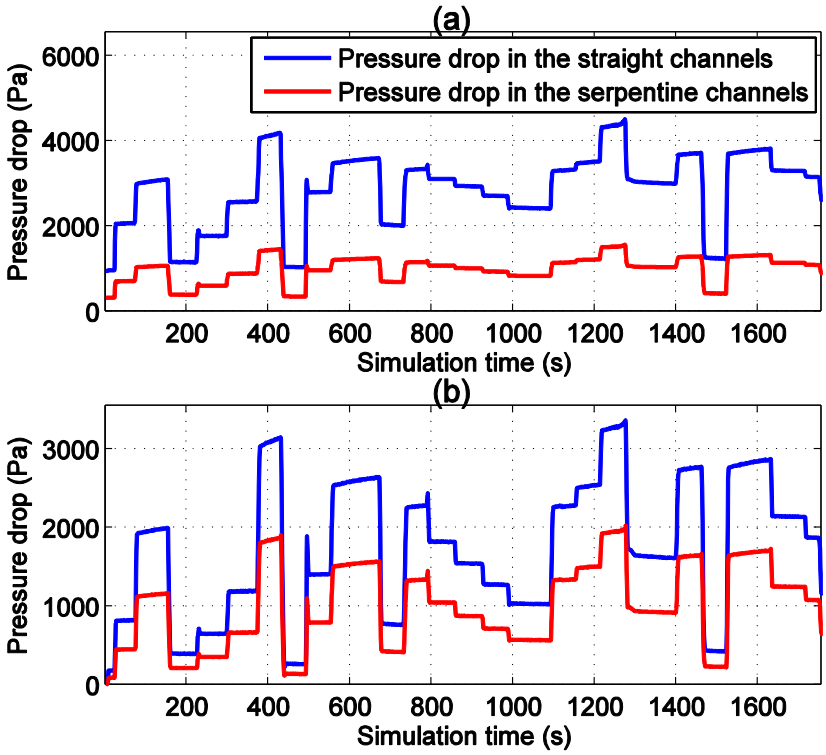

Figure 2.9 Comparison of pressure drop in the channels of two modeling approaches with short step current: (a) Cathode channel. (b) Anode channels.

2.3 2-D Model Simulation Results and Discussions

2.3.1 Model Grid Independence Analysis

The model grid independence analysis determines the minimum mesh grid number needed for a multi-dimensional model. When increasing the mesh number, if the changes of model outputs are less than a pre-defined acceptable error, this mesh number can be considered to meet the independence criteria.

Table 1.1 Mesh Grid Independence Check for 2D Model Output

Mesh number	Model outputs difference (%) (to previous mesh number results)
32	-
48	0.314
64	0.132
128	0.015
256	0.007

The proposed 2-D model output voltage differences for different control volume numbers of uniform segments are shown in the table 1.1. It can be concluded from the table 1.1 that, when the mesh number is larger than 256, the model outputs difference is less than 0.01%, thus it can be consider that the model outputs are no longer affected by the change of mesh grid size.

2.3.2 Results and Discussions

The proposed 2-D model thoroughly considers the geometric form of parallel serpentine flow field in the fuel cell. The oxygen pressure distribution in the cathode three-parallel serpentine channel, and hydrogen pressure distribution in the anode single-parallel serpentine channel are shown in figure 2.10 (non-uniform mesh grid distribution of each side).

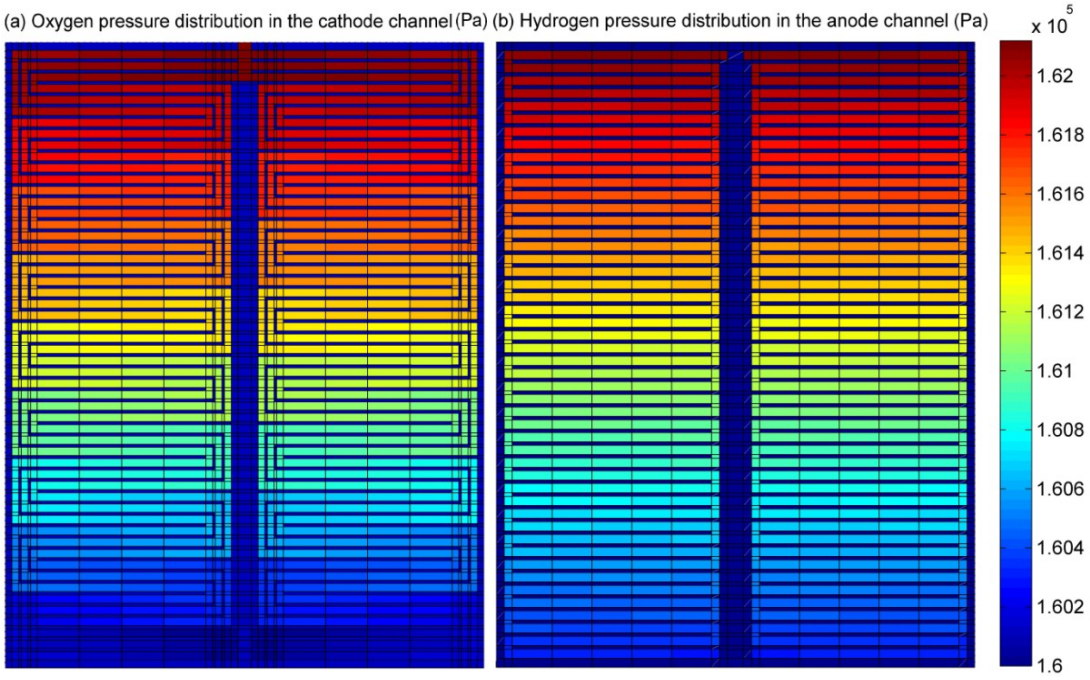

Figure 2.10 Gas pressure distribution in the parallel serpentine channels: (a) cathode side. (b) anode side.

As shown in the figure 2.10, both the oxygen and hydrogen pressure decrease gradually along the direction of the air flow in the parallel serpentine channels, due to the progressive consumption of reactant gas along the channels. As mentioned in the previous section, by taking the channel geometric form into consideration, the non-uniformity distribution results can be effectively obtained.

The 2-D simulation results of physical quantities in GDL layer (electrode) are also illustrated under different oxygen stoichiometry ratio τ, which defined by:

$$\tau = q_{O_2,inlet}/q_{O_2} \tag{1.49}$$

where $q_{O_2,inlet}$ is the inlet oxygen molar flow rate. Based on the segment independence analysis results, the mesh number 600 is chosen for the proposed 2-D model experimental validation, in order to give an accurate distribution results.

When the cell current is set to 27.5A, the oxygen pressure distributions on the surface of electrode (GDL) under different oxygen stoichiometry ratio are shown in the figure 2.11.

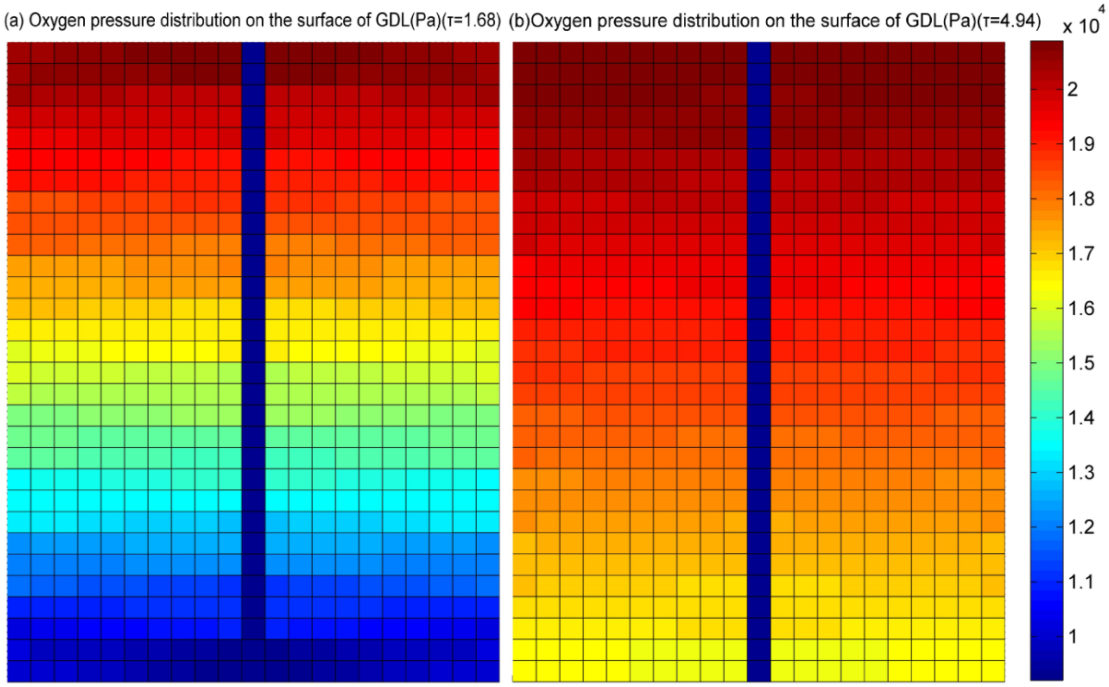

Figure 2.11 Oxygen pressure distribution on the surface of GDL under different oxygen stoichiometry: (a) τ=1.68. (b) τ=4.94

It can be clearly observed from the figure 2.11 (b) that, under a higher τ condition $\tau = 4.94$, the oxygen pressure variation is less significant compared to figure 2.11 (a). That is because the oxygen supply excess rate is higher, and further lead to a more uniform oxygen pressure distribution on the surface of electrode.

Under the same current, the current density distributions on the surface of electrode are also shown in the figure 2.12.

It can be seen from the figure 2.12 that, the current density distribution is similar to that of oxygen pressure. The oxygen pressure at catalyst layer is higher at channel inlet than outlet, which leads to a higher current density at air inlet. As shown in the figure 2.12 (a), under the condition τ=1.68, the maximum difference of current density is about 45% between fuel cell inlet and outlet. It can be also observed from the figure 2.12 (b) that,

under a higher τ condition τ=4.94, the current density distribution gradient is less significant compared to figure 2.12 (a). In this case, the maximum difference of current density is only about 15% between fuel cell inlet and outlet.

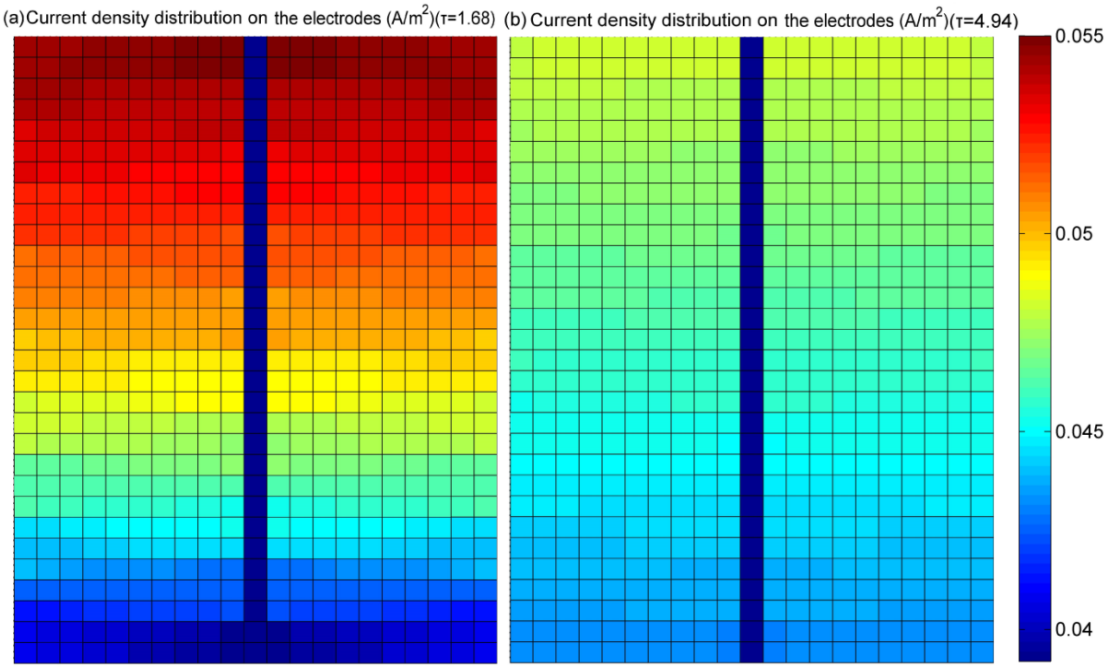

Figure 2.12 Current density distribution on the electrodes under different oxygen stoichiometry: (a) τ=1.68. (b) τ=4.94

2.4 Dynamic Phenomena Coupling Analysis

The dynamic fuel cell model has been presented for the purpose of fuel cell control performance optimization. The fuel cell dynamic behaviors in different physical domains are indeed inter-coupled between each other and the variation of one would influence another. The dynamic variable coupling analysis should be performed for fuel cell system in order to develop an optimized control algorithm.

The water and thermal management is very important for the fuel cell performance and efficiency. For the thermal domain, the fuel cell temperature dynamic behavior is the most significant dynamic in the fuel cell stack. The time constants of fuel cell system in thermal domain can be relatively long, due to large thermal capacities and volumes of cell components (bipolar plates, membrane, etc.) [5]. For the fluid domain, The dynamic of the membrane water content is another significant dynamic phenomenon in the fuel cell stack, which has similar transient time constant compared to temperature dynamic in the thermal domain. It is thus necessary to analyze the variable coupling between these two fuel cell operational parameters.

It should also be noted that, as shown and discussed in the previous section, a non-uniform distribution of current density in the fuel cell electrode can be observed due to the reactant gas pressure variation in the gas supply channels. A more homogenous distribution of current density can maintain the stability and improve the long-term performance of the fuel cell system. The current density distribution is simultaneously affected by the dynamic phenomena in both thermal and fluid domains. Therefore, it should also be carefully considered for coupling analysis in order to provide insights into the variable interaction among three different physical domains.

In this section, detailed expressions of time constant for temperature and membrane water content are given at first, followed by analyses of step responses for various fuel cell system input variables. The corresponding dynamic variable coupling analysis is introduced and discussed at last.

2.4.1 Expressions of Time Constant for Temperature and Membrane Water Contents

The expression of time constant of temperature in thermal domain can be deduced from the general first order dynamic form [5]:

$$\tau_{thermal} = \frac{\rho_{cell} V_{cell} C_p}{h_{forced} S_{forced} + h_{nat_{radia}} S_{ext} - k_{source}} \tag{2.1}$$

Thus, in the thermal domain, the fuel cell temperature transient response time can be estimated to be 497s in the case of studied 1.2 kW Ballard NEXA fuel cell stack.

For the time constant of membrane water content, the left hand side of equation 1.34 becomes zero in steady-state, and the steady-state membrane water content value λ_{i_Final} (s) can be obtained:

$$\lambda_{i\_Final} = \frac{A_{mem} D_{water} \rho_{dry,mem} F \lambda_{ca}}{A_{mem} D_{water} \rho_{dry,mem} F + \frac{n_{drag}^{SAT}}{22} i M_{mem} \delta_{mem}} \tag{2.2}$$

Then the water content dynamic in transient state can be obtained in a general first order dynamic form:

$$\frac{A_{mem} \rho_{dry,mem} \delta_{mem}^2 F}{A_{mem} D_{water} \rho_{dry,mem} F + \frac{n_{drag}^{SAT}}{22} i M_{mem} \delta_{mem}} \cdot \frac{d\lambda_w}{dt} + \lambda_w = \lambda_{i\_Final} \tag{2.3}$$

And the expression of time constant of water content in membrane τ_{water} (s) can then be obtained by the following equation:

$$\tau_{water} = \frac{A_{mem}\rho_{dry,mem}\delta_{mem}^2 F}{A_{mem}D_{water}\rho_{dry,mem}F + \frac{n_{drag}^{SAT}}{22} iM_{mem}\delta_{mem}} \tag{2.4}$$

It can be seen clearly from equation 2.4 that τ_{water} is determined by stack current i. Thus, the system time constant value of water content τ_{water} can be estimated to 108.75 s when stack current is 27 A, means that the response time of membrane water content variation can last about 435 s. This value is in agreement with the results shown in figure 2.6.

It can also be seen that, temperature in thermal domain and membrane water content in fluidic domain have very similar dynamic time constant. It is thus necessary to analyze the variable coupling between these two fuel cell operational parameters.

2.4.2 Analyses of Step Responses

2.4.2.1 High Efficiency Operating Region

In order to understand the effects of fuel cell operational parameter coupling from a control point of view among three different physical domains, the fuel cell system can be considered as a multi input and multi output (MIMO) system, where four possible control input variables are listed as follows:

1) The coolant inlet temperature $T_{cool,inlet}$ (controlled by heat exchanger and bypass circuit);
2) The gas channel inlet temperature $T_{channel,inlet}$ (controlled by inlet/outlet gas heat exchanger);
3) The gas supply channel inlet water vapor pressure $P_{H_2o,inlet}$ (controlled by gas humidifier);
4) The inlet air molar flow rate $q_{air,inlet}$ (controlled by air compressor).

And four controlled output variables in the proposed MIMO system are listed as follows:

1) The membrane electrode assembly (MEA) temperature $T_{membrane}$;
2) The bipolar plate temperature $T_{support}$;
3) The membrane water content $\lambda_{membrane}$;
4) The uniformity coefficient of current density distribution on the electrode $\gamma_{current}$.

where the uniformity coefficient $\gamma_{current}$ is the current density ratio between the highest and the lowest value on the same electrode. This coefficient is proposed to describe the degree of uniformity of current density distribution.

Thus, the non-linear state space equations of this MIMO system can then be expressed as follows:

$$\begin{cases} \dot{T}_{membrane} = f_1\left(T_{membrane}, T_{cool,inlet}, T_{channel,inlet}, q_{air,inlet}\right) \\ \dot{T}_{support} = f_2\left(T_{support}, T_{cool,inlet}, T_{channel,inlet}, q_{air,inlet}\right) \\ \dot{\lambda}_{membrane} = f_3\left(\lambda_{membrane}, P_{H_2o,inlet}, T_{cool,inlet}, q_{air,inlet}\right) \\ \gamma_{current} = \dfrac{i_{current,maximum}}{i_{current,minimum}} \\ \qquad\qquad = f_4\left(T_{cool,inlet}, T_{channel,inlet}, P_{H_2o,inlet}, q_{air,\text{inlet}}\right) \\ y = \begin{pmatrix} T_{membrane} \\ T_{support} \\ \lambda_{membrane} \\ \gamma_{current} \end{pmatrix} \end{cases} \tag{2.5}$$

As the above fuel cell MIMO system state space shown, the vector form representations of the manipulated input variables is $u = [T_{cool,inlet}, T_{channel,inlet}, P_{H_2o,inlet}, q_{air,inlet}]^T$, and the controlled output variables is $y = [T_{membrane}, T_{support}, \lambda_{membrane}, \gamma_{current}]^T$. f_1, f_2, f_3 and f_4 can be derived using the formula of the physical modeling equations presented in chapter II. Since there is a complicated non-linear mathematical relationship between input and output variables, examining the dynamic responses of controllable outputs after step changes of inputs are particularly useful for having insight on the possible variable coupling. Figure 2.13 - 2.16 show the simulated dynamic responses of controllable outputs after step changes of different inputs.

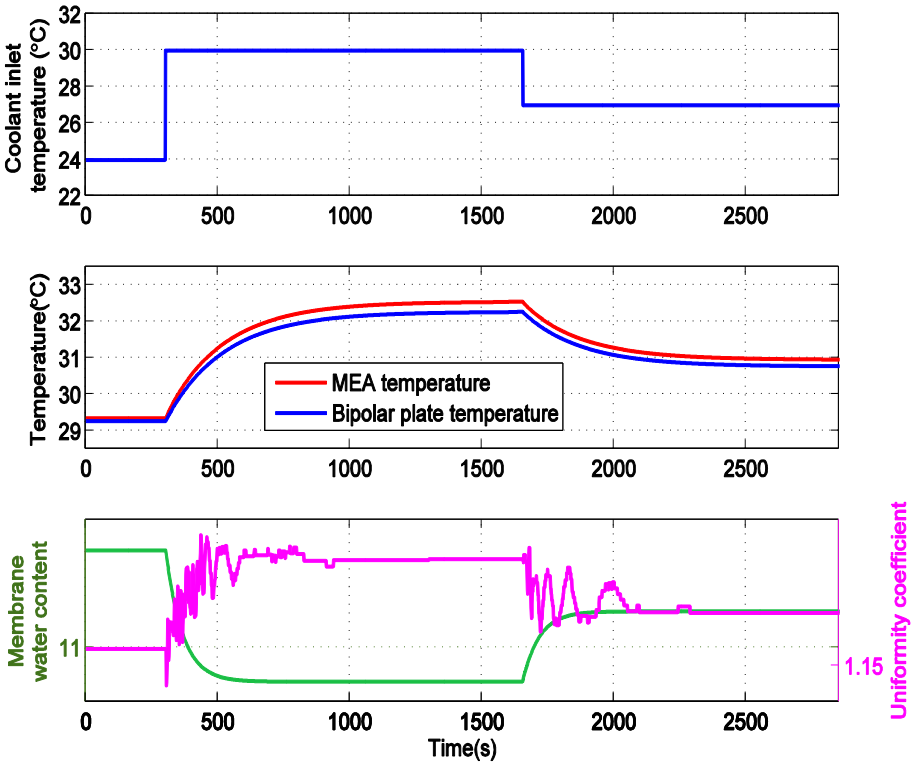

Figure 2.13 The MIMO system outputs response after step change of $T_{cool,inlet}$.

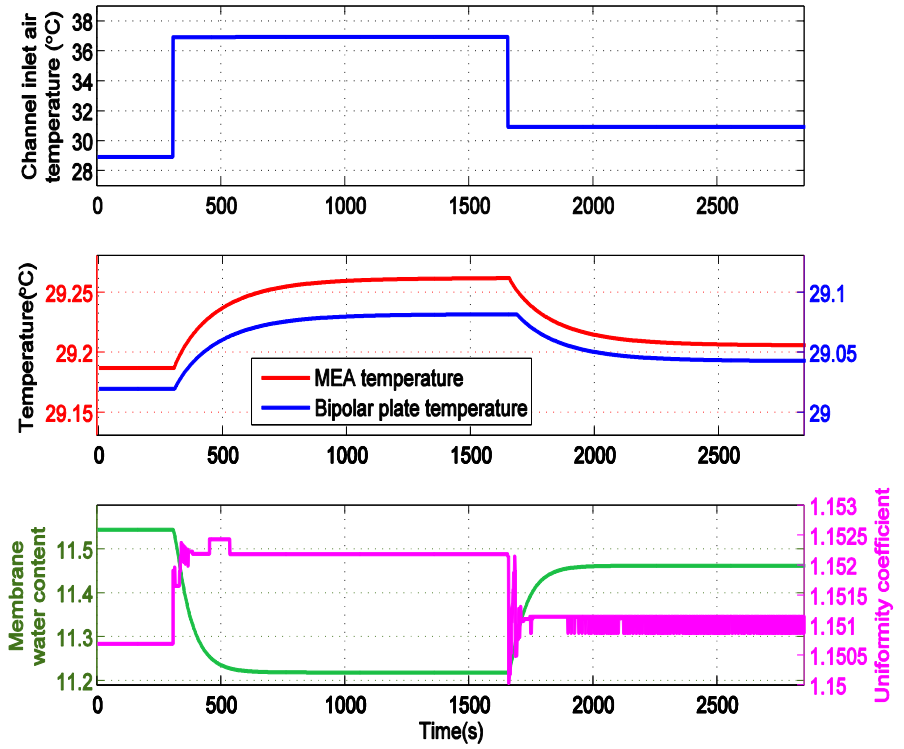

Figure 2.14 The MIMO system outputs response after step change of $T_{channel,inlet}$.

The first operating point is set to between 1/3 and 1/2 rated power point, which corresponds to the high efficiency operating region of fuel cell system. Figure 2.13 shows

the dynamic response of the MIMO system outputs after step changes of the coolant inlet temperature. An increase of the coolant inlet temperature is set at 300 s, which lead to an increase of temperature both in the bipolar plate and MEA. It further results in an increase of the saturation vapor pressure. Therefore, the water activity α_i decreases, as well as the membrane water content at cathode side at 300 s, as the green line shows at the bottom of the Figure 2.13. The uniformity coefficient, presented by the purple line on the same figure, slightly increases at 300 s. It means that the distribution of current density on the electrode is less homogeneous. Similarly, when the coolant inlet temperature decreases at 1650 s, it results in an opposite effect on the four fuel cell variables.

Figure 2.14 shows the dynamic response of the MIMO system outputs after step changes of the channel inlet air temperature. An increase in the bipolar plate temperature and MEA temperature can be observed when the channel inlet air temperature is increased at 300 s. With the MEA temperature increase, the membrane water content decrease, as the green line shows. At the same time the purple line indicates a slightly less homogenous distribution of current density with the increase of gas channel inlet temperature.

Figure 2.15 shows the dynamic response of the fuel cell MIMO system outputs after step changes of the gas supply channel inlet water vapor pressure. It can be seen from the figure 2.15 that membrane water content increases due to an increase of inlet water vapor pressure at 300 s. For the thermal domain, a step change of the gas supply channel inlet water vapor pressure has no significant effect on the temperature. For the electrical domain, an increase of channel inlet water vapor pressure makes the current density distribution slightly more dispersed.

Figure 2.16 shows the dynamic response of the MIMO system outputs after step changes of the air inlet mass flow rate. An increase of air inlet mass flow rate has weak effects on the thermal domain. Due to the increase of air flow rate, the water removal rate increases, and further results in a decrease of the membrane water content. For the electrical domain, an increase of air inlet mass flow rate makes the current density distribution more homogenous. That is because the oxygen is supplied under a higher flow ratio. For the same oxygen consumption rate (same current), the oxygen pressure through the cathode gas channel is thus more uniformly distributed, and further leads to more homogenous distribution of current density on the fuel cell electrode.

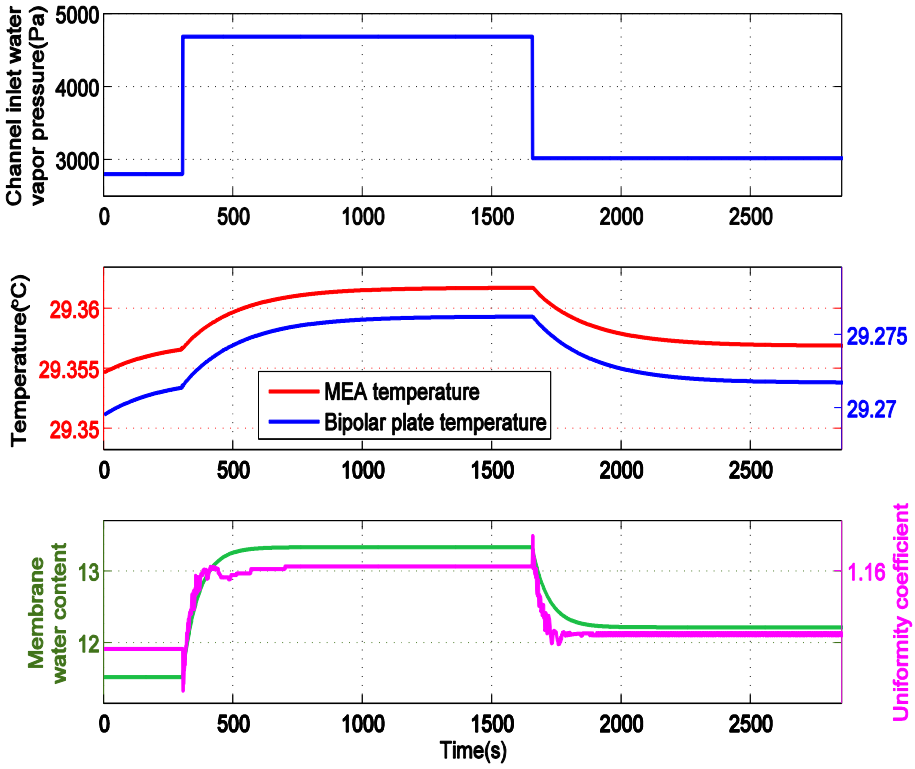

Figure 2.15 The MIMO system outputs response after step change of $P_{H_2O,inlet}$.

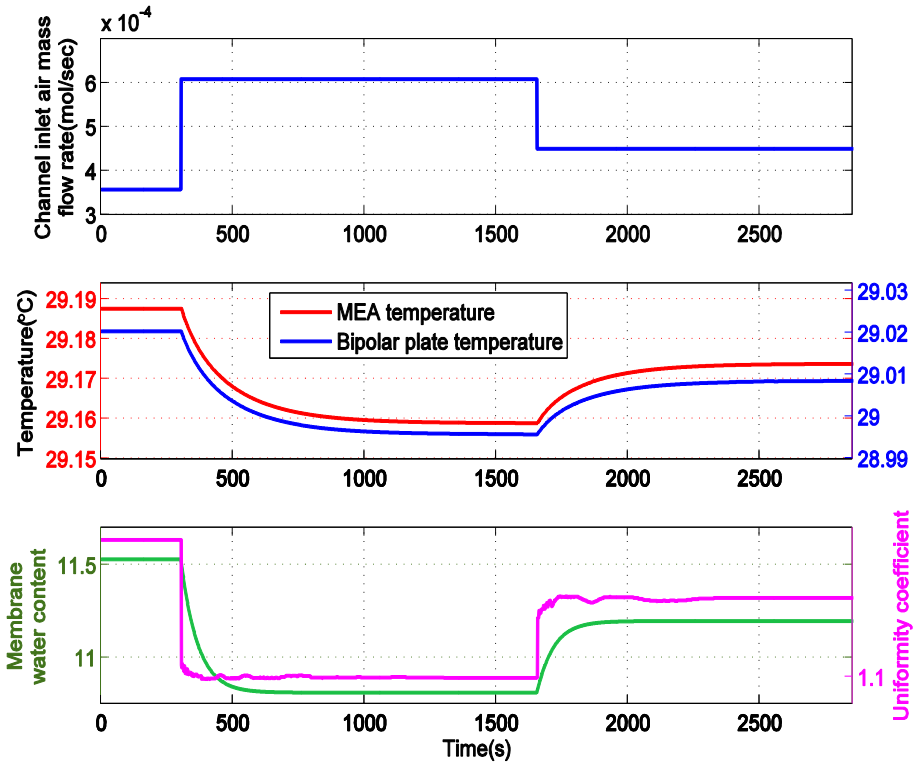

Figure 2.16 The MIMO system outputs response after step change of $q_{air,inlet}$.

2.4.2.2 Rated power Operating Region

For a well-designed fuel cell hybrid powertrain with a proper energy management strategy, the operating range of the fuel cell system would be either in its "max efficiency" zone, or in its "rated power" zone. Thus, a coupling analysis is also performed for the operating point in "rated power" region (i.e. for the studied NEXA stack, it corresponds to a fuel cell current of 42 A), where the fuel cell system power is close to its rated value. The simulated dynamic responses of the MIMO system outputs after step changes are shown in the figures 2.17 - 2.20.

It can be seen from figures 2.17 - 2.20 that, for the operating point in the "rated power" region, the four variation ranges of membrane water content $\lambda_{membrane}$ are reduced compare to that of figures 2.13 - 2.16 as shown in the previous section. That is because when the fuel cell system operates at "max power" region, the dynamic behavior of membrane water is changed and lead to an insensitive $\lambda_{membrane}$. Based on the presented analyses of step responses, detailed analyses of coupling effects between inputs and outputs are further given in the following section.

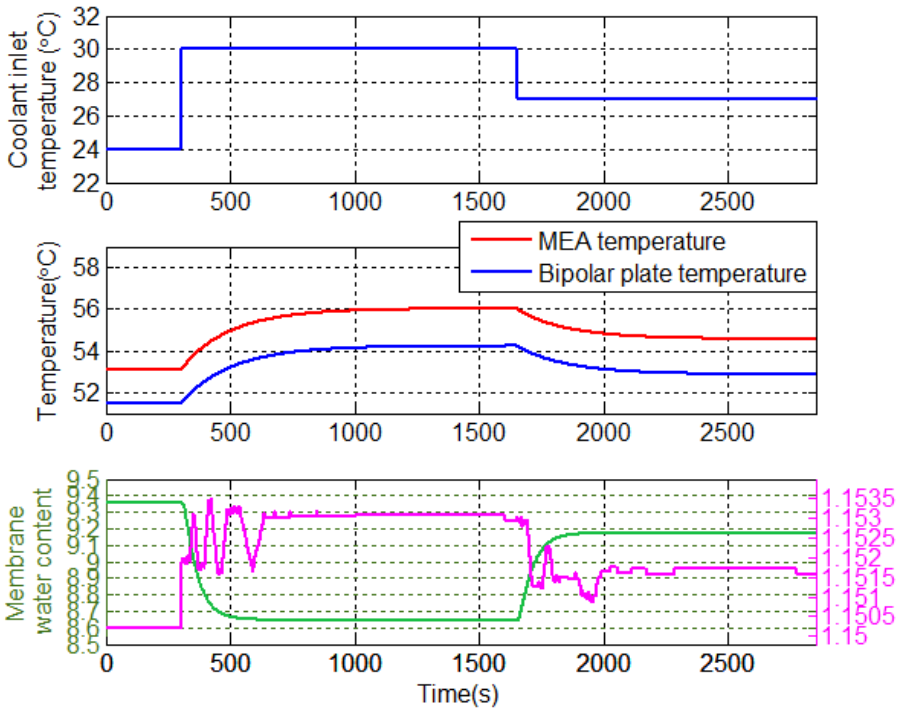

Figure 2.17 The MIMO system outputs response after step change of $T_{cool,inlet}$.

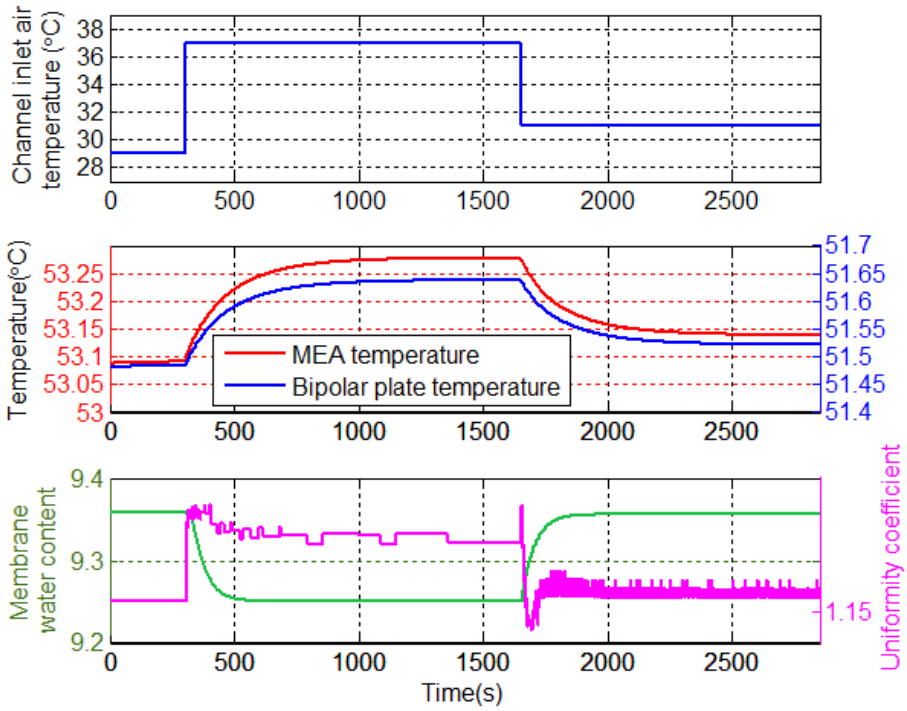

Figure 2.18 The MIMO system outputs response after step change of $T_{channel,inlet}$.

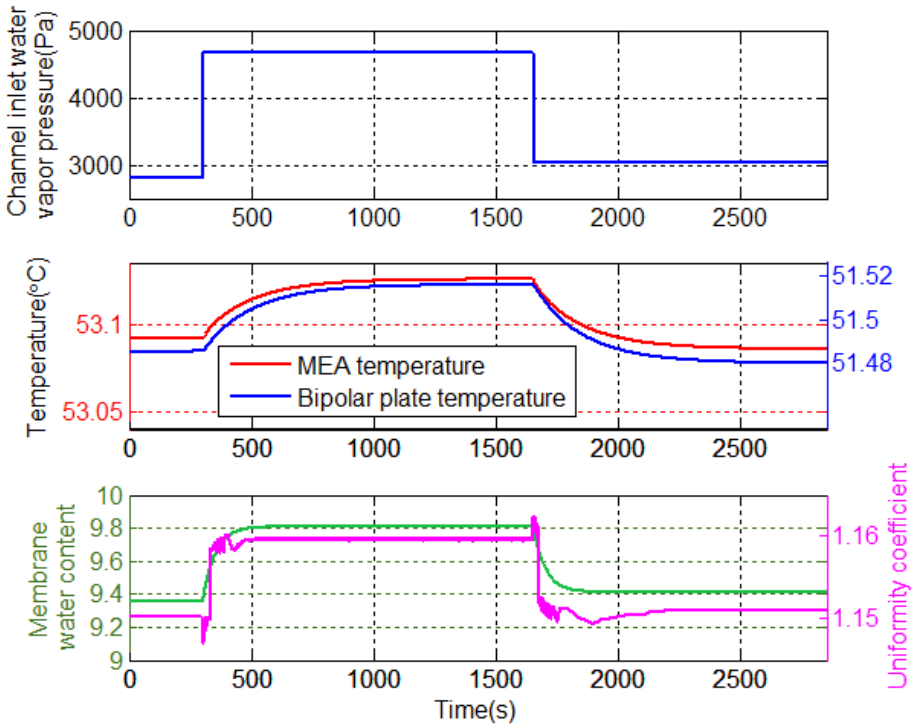

Figure 2.19 The MIMO system outputs response after step change of $P_{H_2O,inlet}$.

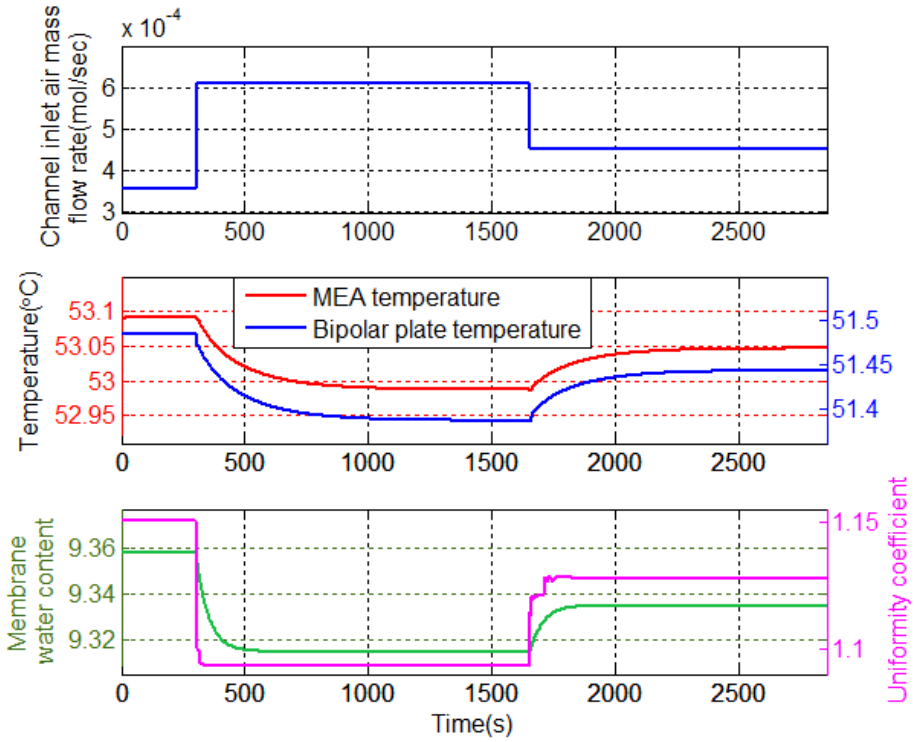

Figure 2.20 The MIMO system outputs response after step change of $q_{air,inlet}$.

2.4.3 Coupling Analysis Using RGA Method

2.4.3.1 Relative Gain Array

In order to quantitatively analyze the interactions among multiple control loops, the relative gain array (RGA) method in control theory are carried out in this study. RGA method is a theory developed by Bristol in 1966 [6] [7] to quantify the degree of interaction of input and output variables. For a j inputs i outputs system, the $i \times j$ matrix RGA is given by:

$$RGA = \begin{bmatrix} \lambda_{11} & \cdots & \lambda_{1j} \\ \cdots & & \cdots \\ \lambda_{i1} & \cdots & \lambda_{ij} \end{bmatrix} \tag{2.6}$$

The open-loop gains of the i-th controlled outputs are determined based on the response to a change of the j-th manipulated inputs, and all other manipulated inputs remain constant:

$$\lambda_{ij} = \frac{\frac{\partial y_i}{\partial u_j}|_{u_r=cont,(r\neq j)}}{\frac{\partial y_i}{\partial u_j}|_{y_r=cont,(r\neq i)}}, (i = 1,2,\cdots; j = 1,2,\cdots) \tag{2.7}$$

where u_j represents the control inputs $T_{cool,inlet}$, $T_{channel,inlet}$ $P_{H_2O,inlet}$ and $q_{air,inlet}$ respectively. y_i represents the system outputs $T_{membrane}$, $T_{support}$, $\lambda_{membrane}$ and $\gamma_{current}$, respectively.

In order to give a clear implications of interactions among control loops, the RGA analysis rules are expressed based on the values of λ_{ij}:

1) $\lambda_{ij} < 0$, a change of u_j produce an opposite direction effect on y_i when other control loops are closed, the sign of open-loop gain between u_j and y_i is changed. In this case, the selection of control pairing u_j-y_i should be avoided;

2) $\lambda_{ij} = 0$, a change of u_j can not affect y_i and therefore should not be used to control y_i. In this case, there is no interaction between control pairing u_j-y_i and other control loops (i.e., coupling does not exist);

3) $0 < \lambda_{ij} < 1$, there exist two effects: the effect of open-loop gain between u_j and y_i, and the effect from other control loops. The effect of open-loop gain from control pairing u_j-y_i increases with the value of λ_{ij}. When $\lambda_{ij} = 0.5$, the two effects are equivalent, there is a strongest coupling effect between the two control variable pairs for a two inputs two outputs system. When $0.5 < \lambda_{ij} < 1$, the open-loop gain of control pairing u_j-y_i becomes the dominant effect. In this case, the most suitable control variable pairing should be u_j-y_i, and optimized control results could be achieved by using a decoupling control method [1] [8];

4) $\lambda_{ij} = 1$, the relative gain 1 indicates the most suitable control variable pairing u_j-y_i, since the open-loop gain between u_j and y_i is not affected by the interaction from the other control loops. In this case, there is no coupling between variable pairing u_j-y_i and other control loops;

5) $\lambda_{ij} > 1$, the effect of other control loops enhance the open-loop gain between u_j and y_i, the larger λ_{ij} is above the unity, the greater will be this effect. In this case, variable pairing u_j-y_i is recommended when λ_{ij} is not very large, a multivariable control design [9] could be used to achieve optimized control performance;

6) $\lambda_{ij} \gg 1$, a value of λ_{ij} greater than 3 indicates that the system is difficult to control due to strong coupling effects from other control loops, and is also sensitive to input uncertainty (e.g., cause by neglected actuator dynamics) [10]. In this case, a robust decoupling control strategy [4] could be used to achieve optimized control performance.

2.4.3.2 Coupling Analysis of the Proposed MIMO system (High Efficiency Operating Region)

When the MEA temperature $T_{membrane}$, the bipolar plate temperature $T_{support}$, the membrane water content $\lambda_{membrane}$, and the uniformity coefficient of current density distribution on the electrode $\gamma_{current}$ are viewed as outputs $y = [T_{membrane}, T_{support}, \lambda_{membrane}, \gamma_{current}]^T$, the formula of this four inputs four outputs system can be described as follows:

$$\begin{bmatrix} T_{membrane} \\ T_{support} \\ \lambda_{membrane} \\ \gamma_{current} \end{bmatrix} = G_{MIMO}(s) \begin{bmatrix} T_{cool,inlet} \\ T_{channel,inlet} \\ P_{H_2O,inlet} \\ q_{air,inlet} \end{bmatrix} \tag{2.8}$$

It should be noted that, the transfer function $G_{MIMO}(s)$ is highly non-linear. In order to linearize the non-linear system equation 2.8, two common operating points of fuel cell system in typical fuel cell hybrid powertrain are selected for the analysis. The first operating point is set to between 1/3 and 1/2 rated power point, which corresponds to the high efficiency operating region of fuel cell system.

On the other hand, the magnitude range difference of each physical parameter is very large. For example, the variation range of control input $T_{cool,inlet}$ is from 297.15 K to 303.15 K, the variation range of control input $P_{H_2O,inlet}$ is from 2814 Pa to 4700 Pa. In order to analyze the coupling effect of different physical parameters in the same RGA, their numerical variation ranges are normalized firstly prior to the RGA analysis.

Table 2.1 Relative Gain Array of System among Thermal, Fluidic and Electrical Domain in Fuel Cell High Efficiency Operation Range

	$T_{cool,inlet}$	$T_{channel,inlet}$	$P_{H_2O,inlet}$	$q_{air,inlet}$
$T_{membrane}$	-2.6948	3.6892	0.0056	0.0000
$T_{support}$	3.5376	-2.5309	-0.0083	0.0016
$\lambda_{membrane}$	0.1859	-0.1899	1.0369	-0.0329
$\gamma_{current}$	-0.0287	0.0316	-0.0343	1.0314

Then by applying RGA method to the normalized parameters of MIMO system equation 2.8 in fuel cell high efficiency operation range, table 2.1 presents the calculated corresponding steady-state RGA values between different input/output variables. It can be seen from table 2.1 that, the RGA elements absolute value of λ_{11}, λ_{12},

λ_{21} and λ_{22} are relatively large, indicate that there exist a strong coupling effects. The RGA element value λ_{31} indicates that the thermal control input $T_{cool,inlet}$ have an intermediate coupling effect on fluidic variable $\lambda_{membrane}$. These two observations are in agreement with the analysis result of time constant in section 2.4.1, that coupling effects may exist between the thermal variable and fluidic variable membrane water content due to similar dynamic time constant values.

It can be concluded from the RGA elements value of λ_{13}, λ_{23}, λ_{33} and λ_{43} that, input variable $P_{H_2o,inlet}$ has a direct control effect on the $\lambda_{membrane}$, at the same time it has little effect on other three output variables. The similar conclusion can be also obtained for input variable $q_{air,inlet}$. As the RGA elements value of λ_{14}, λ_{24}, λ_{34} and λ_{44} indicated, the input $q_{air,inlet}$ has a direct control effect on $\gamma_{current}$, but it has little effect on all other output variables.

2.4.3.3 Coupling Analysis of the proposed MIMO system (Rated Power Operating Region)

In addition to the high efficiency operating region, the second operating point is set to around its rated power point, which corresponds to the high power operating region of fuel cell system. In this case, table 2.2 presents the calculated corresponding RGA values between different input/output variables.

Table 2.2 Relative Gain Array in Fuel Cell High (Rated) Power Operation Range

	$T_{cool,inlet}$	$T_{channel,inlet}$	$P_{H_2o,inlet}$	$q_{air,inlet}$
$T_{membrane}$	-3.0861	4.0767	0.0094	0.0000
$T_{support}$	4.0384	-3.0351	0.0135	-0.0167
$\lambda_{membrane}$	0.1227	-0.0966	0.9817	-0.0078
$\gamma_{current}$	-0.0750	0.0551	-0.0046	1.0245

From table 2.2, the similar coupling effects can be observed, and the same results of coupling analysis can be obtained. Thus it can be concluded that, there exist the similar coupling effects between thermal and fluidic domains in the proposed MIMO system for both fuel cell system typical operation points.

2.4.3.4 Coupling Analysis of Sub-System

From the analyses in the previous section, it could be possible to separate the proposed MIMO system into two control sub-systems by minimizing control coupling effects

between each other. The linearized formula of first possible sub-system can be described as follows:

$$\begin{bmatrix} T_{membrane} \\ T_{support} \\ \lambda_{membrane} \end{bmatrix} = G_{sub\_1}(s) \begin{bmatrix} T_{cool,inlet} \\ T_{channel,inlet} \\ P_{H_2O,inlet} \end{bmatrix} \tag{2.9}$$

Table 2.3 Relative Gain Array of First Sub-System

	$T_{cool,inlet}$	$T_{channel,inlet}$	$P_{H_2O,inlet}$
$T_{membrane}$	-2.7098	3.7040	0.0057
$T_{support}$	3.5451	-2.5362	-0.0088
$\lambda_{membrane}$	0.1647	-0.1678	1.0031

Table 2.3 presents the corresponding RGA values for new three inputs three outputs sub-system in fuel cell high efficiency operation range. As analyzed in the previous section, large RGA elements indicate that the control design is critical and challenging due to existence of coupling effect. In this case, a robust decoupling control strategy [4] is recommended to achieve the optimal control objectives for output variables. For example, in [4], a single neuron adaptive PID feedback controller is proposed, which can eliminate the interference derived from the coupling effect.

On the other hand, as the previously analyzed, the variable $\gamma_{current}$ could almost be independently controlled by input variable $q_{air,inlet}$, which can be considered as the second one input one output control sub-system:

$$[\gamma_{current}] = G_{sub\_2}(s)[q_{air,inlet}] \tag{2.10}$$

Furthermore, by conducting the same analysis for the rated power operating point, similar sub-systems separation can also be obtained for the proposed fuel cell MIMO system.

Based on the above analysis, it can be concluded that, different fuel cell operational parameters coupling can be observed among different physical domains during fuel cell operation. When a coupling effect exists, special attention should be paid for control system design, in order to achieve an optimized control performance for fuel cell systems.

2.5 Conclusion

Although the coupling of dynamic phenomena in a fuel cell has an important influence on the control design of fuel cell system, very little information has yet been published in the literature on the analysis of interaction between fuel cell dynamic variables in different physical domains. The first part of this chapter investigates in particular the coupling effect between the dynamic behaviors during fuel cell transient operation, based on the proposed improved dynamic multi-physical proton exchange membrane fuel cell model, which can be found in the previous works [11] [12].

2.5 Reference

[1] D. Zhao, Q. Zheng, F. Gao, D. Bouquain, M. Dou, A. Miraoui, "Disturbance decoupling control of an ultra-high speed centrifugal compressor for the air management of fuel cell systems," *Int. J. Hydrogen Energy*, vol. 39, no.4, pp. 1788-1798, Jan. 2014.

[2] M. Cheah, I. Kevrekidis, J. Benziger, "Effect of Interfacial Water Transport Resistance on Coupled Proton and Water Transport Across Nafion," *J. Phys. Chem. B,* vol. 115, pp. 10239–10250, 2011.

[3] B. Carnes, N. Djilali, "Analysis of coupled proton and water transport in a PEM fuel cell using the binary friction membrane model," *Electrochimica Acta*, vol. 53, no. 3, pp. 1038-1052, Nov. 2006.

[4] H. Cao, X. Li, "Thermal Management-Oriented Multivariable Robust Control of a kW-Scale Solid Oxide Fuel Cell Stand-Alone System," *IEEE Trans. Energy Convers.*, vol. 31, pp. 596–605, 2016.

[5] F. Gao, B. Blunier, A. Miraoui, A. El-Moudni, "Proton exchange membrane fuel cell multi-physical dynamics and stack spatial non-homogeneity analyses," *J. Power Sources*, vol. 195, pp. 7609–7626, 2010.

[6] E. H. Bristol, "On a new measure of interaction for multivariable process control," *IEEE Trans. Autom. Control*, vol. 11, no. 1, pp. 133–134, Jan. 1966.

[7] M. Wal, B. Jager, "A review of methods for input/output selection," *Automatica*, vol. 37, no. 4, pp. 487–510, 2001.

[8] D. Zhao, M. Dou, B. Blunier, A. Miraoui, "Control of an ultra high speed centrifugal compressor for the air management of fuel cell systems," in *Proc. IEEE IAS*, oct. 7-11, 2012, pp. 1-8.

[9] J. Pukrushpan, A. Stefanopoulou, S. Varigonda, L. Pedersen, S. Ghosh, H. Peng, "Control of natural gas catalytic partial oxidation for hydrogen generation in fuel cell applications," *IEEE Trans. Contr. Syst. Technol.*, vol. 13, no. 1, pp. 3-14, Jan. 2005.

[10] S. Skogestad and M. Morari, "Implications of large rga-elements on control performance," *Industrial & engineering chemistry research*, vol. 26, no. 11, pp. 2323-2330, 1987.

[11] D. Zhou, F. Gao, E. Breaz, A. Ravey, A. Miraoui, K. Zhang, "Dynamic phenomena coupling analysis and modeling of PEMFCs," *IEEE Trans. Energy Convers.*, vol. 31, no. 4, pp. 1399–1412, Dec. 2016.

[12] D. Zhou, K. Zhang, A. Ravey, F. Gao, A. Miraoui, "Dynamic variable coupling analysis and modeling of proton exchange membrane fuel cells for water and thermal management," *IEEE Applied Power Electronics Conference and Exposition (APEC)*, Long Beach, CA, Mar. 20-24, 2016.

Chapter III: PEMFC 2-D model numeric solver development for Real-Time Control Implementation

As mentioned before, the quantitative analyses in Chapter II can provide us useful information for modeling assumptions (simplification), which can be used to simplify the 2-D modeling. For example, since the tortuosity ι and porosity ε can be considered as insensitive parameters for a lower fuel cell stack current, the diffusion mass transport can be reasonably neglected. In this case, there is no total pressure gradient in the gas diffusion layer. During the development of fuel cell model with these simplifications, the computational complexity can be effectively reduced while maintaining a high accuracy.

The main objective of this paper is to present a novel 2-D PEMFC modeling approach based on a numerical solver tridiagonal matrix algorithm (TDMA) for real-time control implementation. The proposed PEMFC model covers multi-physical domains in both fluidic and electrochemical. The major contributions of this paper can be summarized as follows:

1) A novel non-uniform control volumes mesh grid is defined in fluidic domain modeling based on channel geometric patterns, in order to thoroughly describe the gas flow characteristics by taking the fuel cell flow field geometric form into consideration. In addition, the differential equations of reactant gas convection and diffusion phenomena are transformed into tridiagonal systems of equations, which can be efficiently solved by tridiagonal matrix algorithm.

2) An implicit iterative solver has been developed to solve spatial physical quantity distributions for electrochemical domain. This original iterative solver algorithm is composed by three interactive computational loops and uses a robust convergence method for real-time computation.

3) The practical feasibilities of the proposed 2-D model in advanced real-time control of PEMFC systems have been experimentally demonstrated in a RT-LAB real-time simulator. The computing technologies presented in this paper are original for real-time PEMFC model and completely independent of commercial

platform. It can be easily implemented to any embedded controller of PEMFC systems.

3.1 Literature Review

Different from the common modeling approach, a real-time oriented fuel cell model has more restrictions: the accuracy and computational efficiency of a real-time fuel cell model are both crucial for model based control process [1]. A sophisticated fuel cell model can provide comprehensive physical quantities for model-based control design and optimization. While the high performance computation of a fuel cell model ensures the model-based controller can be efficiently implemented in real-time applications with a low cost of computations. Several real-time control-oriented PEMFC models have been previously presented in the literature [2]-[4].

Jung *et al.* [2] present a PEMFC real-time model, which considers both the electrical and thermal dynamics. In order to reduce the computational burden, three optimization strategies are used: minimizing algebraic calculation, model separation and reducing the layer structure.

Gao *et al.* [3] develop a cell-level dynamic PEMFC model, which covers electrochemical, fluidic and thermal domains. A top-down design approach is used to provide an efficient PEMFC model structure. By using VHDL-AMS language, the developed model can be used in the hardware-in-the-loop application.

Colclasure *et al.* [4] describes a physical-based transient solid oxide fuel cell (SOFC) model, which considers the coupled interactions of multiple physics. In order to facilitate the real-time control applications, linear model reduction method is used.

However, their models remain in 1-D. During the model-based control process, the spatial physical quantity distribution is neglected, such as gas pressure gradient in the channel, or current density distribution on the surface of electrode. Many PEMFC 2-D models have been previously proposed in the literature [5] [6]. However, a common drawback of these models is the computational complexity of mathematical operations. For example, as mentioned before, the commonly used complex computational fluid dynamic (CFD) models are not suitable for real-time simulation, since the computational burdens are too heavy.

3.2 Tridiagonal Matrix Algorithm for Real-Time Simulation

The tridiagonal matrix algorithm is an efficient numerical solver, which can be applied iteratively for solving multi-dimensional problems [7]-[9]. The tridiagonal matrix algorithm uses a special form of Gaussian elimination, in order to solve a set of equations for tridiagonal system in a backward substitution. Therefore, it can reduce the computational time and memory usage considerably [9].

3.2.1 Tridiagonal Matrix Algorithm

A The TDMA is an efficient numerical solution for solving tridiagonal matrices. The TDMA consists of two steps: a forward elimination procedure and a backward substitution procedure. A tridiagonal system can be written as the following equations in the tridiagonal matrix form:

$$\begin{bmatrix} b_1 & c_1 & & & & 0 \\ a_2 & b_2 & c_2 & & \cdots & \\ & a_3 & b_3 & c_3 & \cdots & \\ & & & \cdots & & \\ & & & & & c_{n-1} \\ 0 & & & & a_n & b_n \end{bmatrix} \begin{bmatrix} x_1 \\ x_2 \\ x_3 \\ \cdots \\ x_{n-1} \\ x_n \end{bmatrix} = \begin{bmatrix} d_1 \\ d_2 \\ d_3 \\ \cdots \\ d_{n-1} \\ d_n \end{bmatrix} \tag{3.1}$$

where $\boldsymbol{x}$ denoted the non-zero inputs of tridiagonal system.

For the first line:

$$b_1 x_1 + c_1 x_2 = d_1 \tag{3.2}$$

Divide both sides of the equation 3.2 by b_1:

$$x_1 + \gamma_1 x_2 = e_1 \tag{3.3}$$

with

$$\begin{cases} \gamma_1 = \dfrac{c_1}{b_1} \\ e_1 = \dfrac{d_1}{b_1} \end{cases}$$

In order to forward eliminate x_1, the equation 3.3 multiplied by a_2 and minus the second row of equation 3.1:

$$(b_2 - a_2\gamma_1)x_2 + c_2 x_3 = d_2 - a_2 e_1 \tag{3.4}$$

Divide both sides of the equation 3.4 by $b_2 - a_2\gamma_1$:

$$x_2 + \gamma_2 x_3 = e_2 \tag{3.5}$$

with

$$\begin{cases} \gamma_2 = \dfrac{c_2}{b_2 - a_2\gamma_1} \\ e_2 = \dfrac{d_2 - a_2 e_1}{b_2 - a_2\gamma_1} \end{cases}$$

Similarly, in order to forward eliminate x_2, the equation 3.5 multiplied by a_3 and minus the second row of equation 3.1:

$$(b_3 - a_3\gamma_2)x_3 + c_3 x_4 = d_3 - a_3 e_2 \tag{3.6}$$

Similar forward elimination procedure is repeated until the n row, the tridiagonal matrix in equation 3.1 can be transformed into a upper triangular matrix:

$$\begin{bmatrix} 1 & \gamma_1 & & & & 0 \\ 0 & 1 & \gamma_2 & & \cdots & \\ & 0 & 1 & \gamma_3 & \cdots & \\ & & & \cdots & & \\ & & & & & \gamma_{n-1} \\ 0 & & & & 0 & 1 \end{bmatrix} \begin{bmatrix} x_1 \\ x_2 \\ x_3 \\ \cdots \\ x_{n-1} \\ x_n \end{bmatrix} = \begin{bmatrix} e_1 \\ e_2 \\ e_3 \\ \cdots \\ e_{n-1} \\ e_n \end{bmatrix} \tag{3.7}$$

with

$$\begin{cases} \gamma_{n-1} = \dfrac{c_{n-1}}{b_{n-1} - a_{n-1}\gamma_{n-2}} \\ e_n = \dfrac{d_n - a_n e_{n-1}}{b_n - a_n\gamma_{n-1}} \end{cases}$$

The inputs of tridiagonal system $\boldsymbol{x}$ can then be solved by backward substitution:

$$\begin{cases} x_n = e_n \\ x_{n-1} = e_{n-1} - \gamma_{n-1}x_n \\ \cdots \\ x_2 = e_2 - \gamma_2 x_3 \\ x_1 = e_1 - \gamma_1 x_2 \end{cases} \tag{3.8}$$

Thus, the general solution for tridiagonal system equation 3.1 can be written as the following equations:

$$x_i = \begin{cases} d_i' & for\ i = n \\ d_i' - c_i' x_{i+1} & for\ i = n-1, n-2, \ldots, 1 \end{cases} \tag{3.9}$$

with

$$c_i' = \begin{cases} \dfrac{c_i}{b_i} & for\ i = 1 \\ \dfrac{c_i}{b_i - a_i c_{i-1}'} & for\ i = 2,3 \ldots, n-1 \end{cases}$$

$$d_i' = \begin{cases} \dfrac{d_i}{b_i} & for\ i = 1 \\ \dfrac{d_i - a_i d_{i-1}'}{b_i - a_i c_{i-1}'} & for\ i = 2,3 \ldots, n \end{cases}$$

A detailed schematic diagram of the TDMA is presented in the following figure 3.1. It is worth specific mention that, by using this special form of Gaussian elimination, and solving the tridiagonal matrices in such backward substitution, compared with straightforward Gaussian elimination $O(n^3)$, the arithmetic complexity of TDMA exponential decays to operations $O(n)$. It means that, if total number of control volumes is 32 (the elements number of inputs $\boldsymbol{x}$ in tridiagonal system), the model computation speed can be 1024 times faster compared with Gaussian elimination. Such fast solving speed allows to significantly reduce the computational time and memory usage.

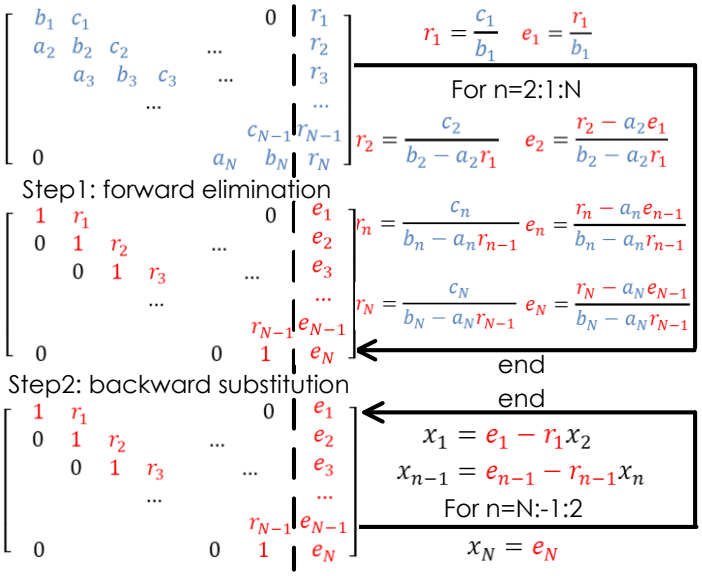

Figure 3.1 Schematic diagram of the TDMA.

3.2.2 Modeling Hypotheses

In order to be able to simulate the model in real-time while keeping the accurate spatial non-homogeneous effect prediction and model accuracy, some assumptions are used when modeling the PEMFC stack.

1) The two-phase flow of water is ignored, but the liquid water saturation, vapor transportation and pressure gradient is considered in the proposed model;

2) The gas flow in the channel and diffusion through the GDL is considered in steady state, since the transient time constant of fluid is relatively short (microsecond or millisecond);

3) The diffusion mass transport due to total pressure gradient is neglected;

4) The activation losses V_{act} of the anode side are neglected due to the fast electrode kinetic of hydrogen gas in PEMFC;

5) The Ohm losses are only determined by resistance of Nafion membrane, the layer contact resistance, electrode resistance are negligible;

6) The reactants are considered as ideal gases;

7) The geometric characteristics of each layer remain unchanged.

3.2.3 Solve Reactant Gas Convection 2-D Model Using Tridiagonal Matrix Algorithm

The control volume partitions of cathode parallel serpentine channel are shown in the figure 3.2 [10]. Based on the gas supply channel geometry, the gas supply channel can be divided into two sections, denoted as "straight volume" and "bend volume", as illustrated in figure 3.2. From figure 3.2, the thin dotted line channel control volume is in the straight section, denoted as "straight volumes" of gas channel. In contrast, the bold dotted line channel control volume is in the curved section, denoted as "bend volumes" of gas channel. The direction of gas convection flow is marked with arrows.

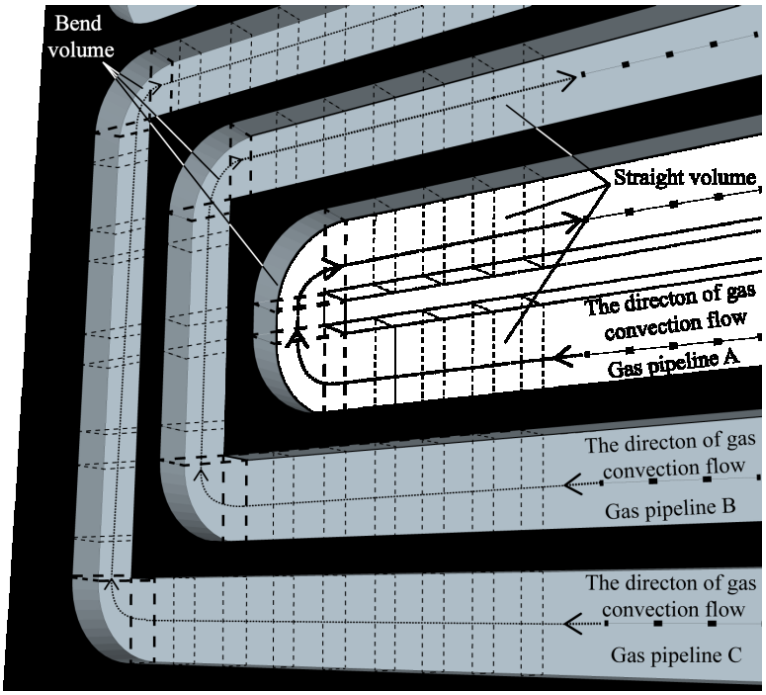

Figure 3.2 Control volume partitions of cathode gas supply channel based on the geometric form.

In order to employ TDMA, the equation 1.43 should be discretized in the serpentine channel based on finite volume method. In addition, all the discretized equations should be transformed into tridiagonal matrix as expressed in equation 3.1. Taking the gas pipeline A (shown in the figure 3.2) as an example, the control volume mesh grid definitions are shown in figure 3.3.

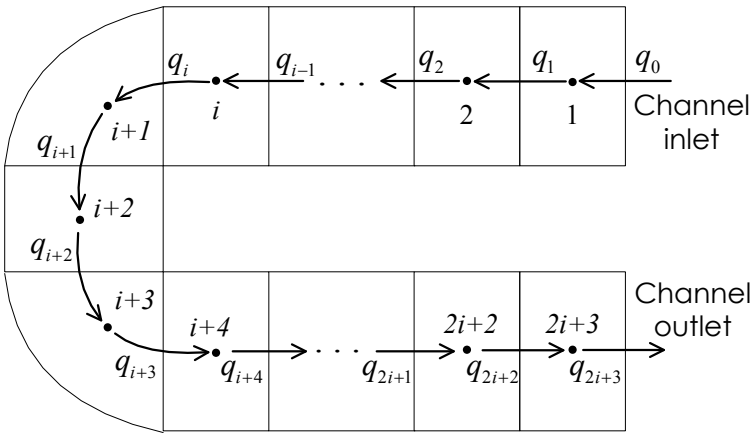

Figure 3.3 Control volume mesh grid definition of the "gas pipeline A" marked in the figure 3.2.

Based on the discretization using finite volume method, for each control volume, the fluid mass flow entering into a control volume is equal to the fluid mass flow leaving out a control volume due to convective transportation. Thus, for the control volume 1 shown in the figure 3.3:

$$q_{inlet} = q_1 \tag{3.10}$$

where q_{inlet} is the gas mass flow at gas supply channel inlet

Based on the assumption 2), the fluid behaviors considered in strady state. Thus, the discretized form of equation 1.13 can be expressed as the following form:

$$\frac{\Delta P}{\Delta x} = \frac{32\mu q}{D^2 \rho A} \tag{3.11}$$

Thus, the fluid mass flow q can be written as:

$$q = \frac{\Delta P}{\Delta x}\frac{D^2 \rho A}{32\mu} = \alpha_x \cdot \Delta P \tag{3.12}$$

The equation 3.11 can be written as:

$$(P_{inlet} - P_1) \cdot \alpha_1 = (P_1 - P_2) \cdot \alpha_2 \tag{3.13}$$

where P_{inlet} is the pressure at gas supply channel inlet. Thus, for equations of all the control volume:

$$\begin{cases} q_{inlet} = q_1 \\ q_1 = q_2 \\ \cdots \\ q_{2i+2} = q_{2i+3} \end{cases} \tag{3.14}$$

the following equations can be obtained:

$$\begin{cases} \dfrac{P_{inlet} - P_1}{l_{inlet-1}} \dfrac{D^2 \rho A}{32\mu} = \dfrac{P_1 - P_2}{l_{1-2}} \dfrac{D^2 \rho A}{32\mu} \\ \dfrac{P_1 - P_2}{l_{1-2}} \dfrac{D^2 \rho A}{32\mu} = \dfrac{P_2 - P_3}{l_{2-3}} \dfrac{D^2 \rho A}{32\mu} \\ \cdots \\ \dfrac{P_{2i+2} - P_{2i+3}}{l_{2i+2-2i+3}} \dfrac{D^2 \rho A}{32\mu} = \dfrac{P_{2i+3} - P_{outlet}}{l_{2i+3-outlet}} \dfrac{D^2 \rho A}{32\mu} \end{cases} \tag{3.15}$$

where l_{x-y} is the distance between two adjacent control volumes x and y. Equation 3.15 can then be written as the tridiagonal matrix:

$$\begin{cases} \alpha_1 P_{inlet} - (\alpha_1 + \alpha_2) P_1 + \alpha_2 P_2 = 0 \\ \alpha_2 P_1 - (\alpha_2 + \alpha_3) P_2 + \alpha_3 P_3 = 0 \\ \cdots \\ P_{2i+2} - (\alpha_{2i+3} + \alpha_{2i+4}) P_{2i+3} + \alpha_{2i+4} P_{outlet} = 0 \end{cases} \tag{3.16}$$

where P_{inlet} and P_{inlet} is considered as boundary conditions, since they are known. Equation 3.16 describes the reactants flow behaviors in a tridiagonal matrix form, which can be directly employed the TDMA. After solving equation 3.16 using TDMA, the pressure distribution due to the mechanical losses suffered in straight channels (P_{i+1}, P_{i+3}) can be obtained. Then the pressure distribution in the serpentine channels can be further obtained based on the equation 1.43.

3.2.4 Solve Reactant Gas Diffusion 2-D Model Using Tridiagonal Matrix Algorithm

In order to clearly show the calculation procedures of TDMA, the "fluid adjacent volumes" are denoted as "F1-F6", the "solid adjacent volumes" are denoted as "S1-S3", as illustrated in figure 3.4 [10]. Take the "solid adjacent volumes S2" as an example. Due to the diffusion phenomena, the reactant gas molar flow (mol/s) entering the "S2" including three parts: diffusion from "F3" to "S2" (x-axis, marked with arrow 1); diffusion from "F4" to "S2" (x-axis, marked with arrow 2); diffusion from "S1" to "S2" (y-axis, marked with arrow 3). The reactant gas molar flow (mol/s) leaving the "S2" including two parts: diffusion from "S2" to "S3" (y-axis, marked with arrow 4); diffusion from "S2" to catalyst layer (z-axis, marked with arrow 5).

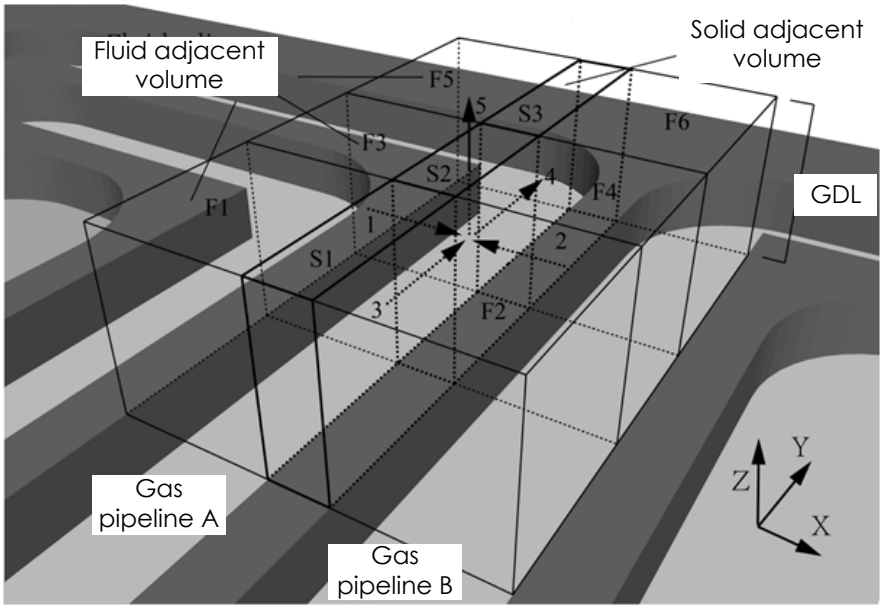

Figure 3.4 Diffusion phenomena for "solid adjacent volumes S2"

In the steady state, the gas molar flow entering the "S2" is equal to that of leaving:

$$N_1 + N_2 + N_3 = N_4 + N_{O_2,S2} \tag{3.17}$$

where N is the gas molar flow. Since the gas molar flow is determined by the pressure difference between two control volumes, thus the equation 3.17 can be expressed as:

$$f_1(P_{F2} - P_{S2}) + f_2(P_{F4} - P_{S2}) + f_3(P_{S1} - P_{S2}) - f_4(P_{S1} - P_{S3}) - N_5 = 0 \tag{3.18}$$

All these diffusion phenomena in the gas diffusion layer, except the above-mentioned current-driven one q_5, can be described by the modified Fick's diffusion law equation:

$$f(\Delta P) = \frac{A_{GDL} \cdot D^{eff}_{GDL,x-y} \cdot \Delta P}{R \cdot T_{GDL} \cdot L} = \alpha_x \cdot \Delta P \tag{3.19}$$

where $\dot{N}_{GDL,x}$ is the gas molar flow rate of specie x, A_{GDL} is the gas diffusion area, $D^{eff}_{GDL,x-y}$ is the gas diffusion coefficient, R is the ideal gas constant, T_{GDL} is the temperature of GDL, L is the center point distance between two control volumes. Thus, equation 3.18 can be rewritten by:

$$-\alpha_3 \cdot P_{S1} + (\alpha_1 + \alpha_2 + \alpha_3 + \alpha_4) \cdot P_{S2} - \alpha_4 \cdot P_{S3} = \alpha_1 \cdot P_{F2} + \alpha_2 \cdot P_{F4} - N_{O_2,S2} \tag{3.20}$$

where

$$N_{O_2,S2} = \frac{M_{O_2} \cdot i_{S2,solid}}{4F} \tag{3.21}$$

In order to compute all the pressure of "solid adjacent volumes S2, S3, S3...", the above equation can be extended to a set of equations:

$$\begin{cases} -\alpha_3 \cdot P_{S1} + (\alpha_1 + \alpha_2 + \alpha_3 + \alpha_4) \cdot P_{S2} - \alpha_4 \cdot P_{S3} \\ \quad = \alpha_1 \cdot P_{F1} + \alpha_2 \cdot P_{F2} - \dfrac{M_{O_2} \cdot i_{S2,solid}}{4F} \\ -\alpha_8 \cdot P_{S2} + (\alpha_6 + \alpha_7 + \alpha_8 + \alpha_9) \cdot P_{S3} - \alpha_9 \cdot P_{S4} \\ \quad = \alpha_6 \cdot P_{F3} + \alpha_7 \cdot P_{F4} - \dfrac{M_{O_2} \cdot i_{S3,solid}}{4F} \\ -\alpha_{13} \cdot P_{S3} + (\alpha_{11} + \alpha_{12} + \alpha_{13} + \alpha_{14}) \cdot P_{S4} - \alpha_{14} \cdot P_{S5} \\ \quad = \alpha_{11} \cdot P_{F5} + \alpha_{12} \cdot P_{F6} - \dfrac{M_{O_2} \cdot i_{S4,solid}}{4F} \\ \quad \cdots \end{cases} \tag{3.22}$$

Thus, equation 3.22 describes the reactants diffusion behaviors through GDL in a tridiagonal matrix form, which can be directly employed the TDMA.

3.3 Implicit Iterative Solver

In the proposed 2-D PEMFC model, the calculations of fluidic gas channel model is based on the non-uniform control volume (black mesh in the figure 1.10), while the calculations of electrode/electrolyte related physical quantities is based on the unified control volume (red mesh in the figure 1.10).

It should be noted that, since the activation loss V_{act} appears in an implicit form in the Butler-Volmer equation 2.6, an iterative solving method should be developed to calculate V_{act} [11]. In addition, this iterative algorithm should also solve the current of each segment (current density distribution) and cell potential (fuel cell output voltage), which cannot be calculated explicitly *a priori* in a 2-D modeling approach. A detailed schematic diagram of the proposed iterative algorithm is presented in the following figures 3.5.

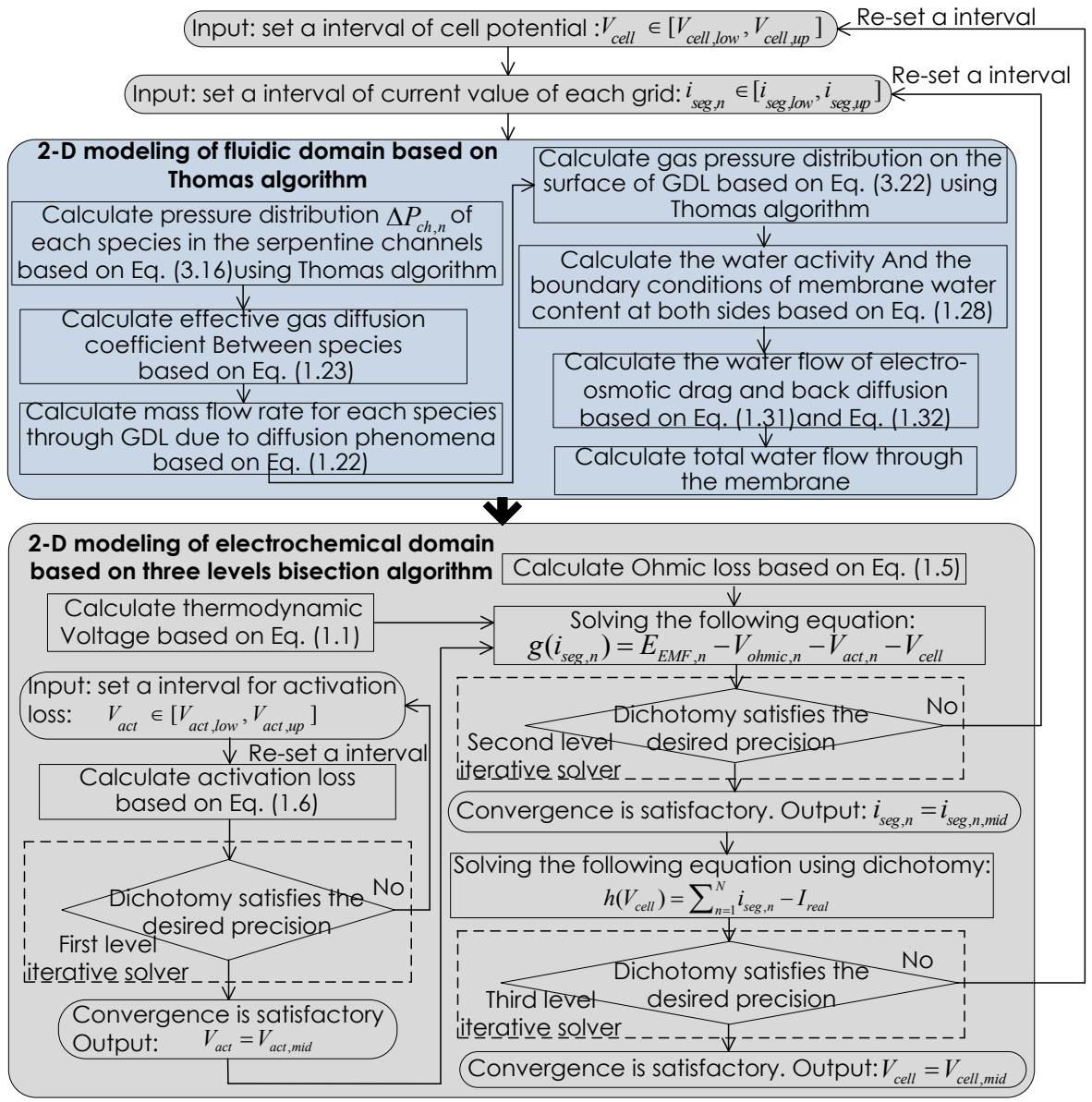

Figure 3.5 Schematic diagram of the proposed iterative solver (First level).

As shown in the figure 3.5, the proposed solver consists of three levels bisection algorithm. The first level solver is the top level algorithm, which is used to compute cell potential V_{cell} (fuel cell output voltage), as shown in the figure. In order to resolve current value of each segment $i_{seg,n}$ (current density) based on the output of first level solver, a second level solver is included in the algorithm. The third level iterative solver is used to calculate activation losses $V_{act,n}$ in the non-linear implicit Butler-Volmer equation 2.6.

By knowing the total current value of fuel cell, and setting appropriate numerical ranges for activation losses of segments $V_{act,n}$, current value of segments $i_{seg,n}$, and cell potential V_{cell}, the cell voltage and individual current in each control volume can be properly calculated by the proposed iterative algorithm.

3.4 Experimental Validation

3.4.1 Experimental Setup

In order to allow a real-time implementation of the developed PEMFC model, the model physical equations, as well as the proposed iterative solver are written in pure C language. The model is then implemented in a RT-LAB real-time simulator (real-time processor operating at 2.5 GHz). The experimental setup of RT-LAB simulator and PEMFC test platform is shown in Figure 3.6.

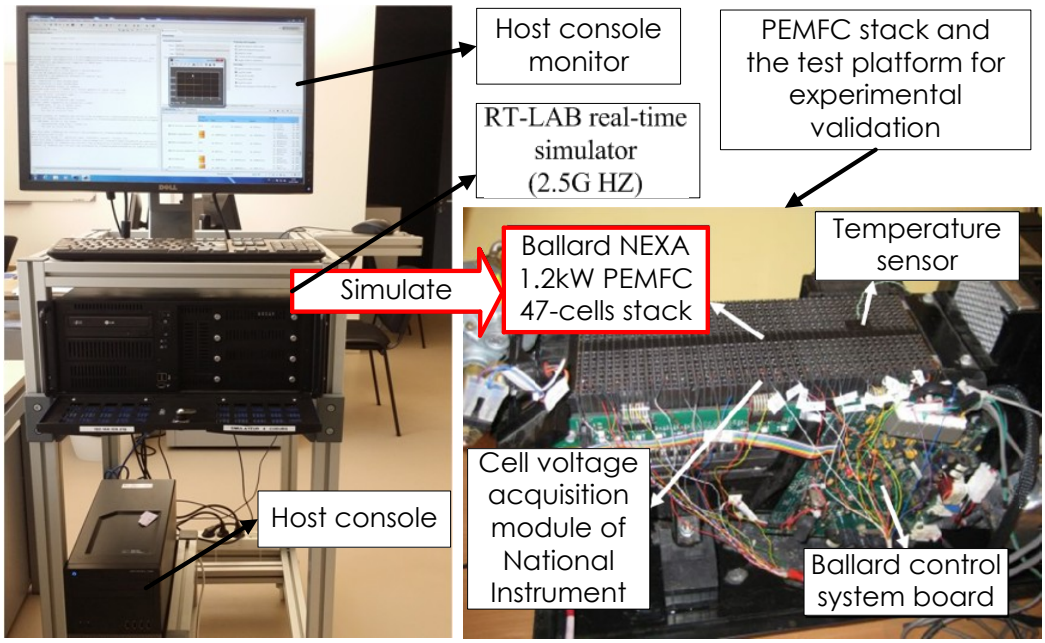

Figure 3.6 RT-LAB real-time simulator platform setup.

The RT-LAB real-time simulator used in this thesis has a real-time processor operating at 2.5 GHz. For a real-time simulation, the model time step should be settled based on model complexity and computation performance.

3.4.2 Experimental Results

The real-time simulation bench mark results of the proposed model under different 2-D mesh number are shown in the table 3.1.

It can be seen from the table 3.1 that, the model execution time increases quasi-linearly with mesh number, since there are more iterations should be solved for a higher number of control volumes. It can be concluded from this benchmark results that, the proposed 2-D multi-physic PEMFC model in this thesis can be effectively used in real-time control implementations with a time step level on the order of milliseconds.

Table 3.1 2-D Real-Time Model Benchmark Results (2.5GHz CPU)

Mesh number	Model CPU execution time	Model time step used	CPU occupation
32	7.429 ms	10 ms	73.3%
48	12.308 ms	15 ms	82.1%
64	17.731 ms	20 ms	88.7%
128	43.061 ms	50 ms	86.12%
256	101.218 ms	120 ms	83.35%
600	257.193 ms	300 ms	85.73%

It should be noted that, the iterative algorithm used in this thesis is completely independent of commercial platform, and can be easily implemented to any embedded controller of PEMFC systems.

3.4.3 Real-Time Performance Comparison

3.4.3.1 Comparison with Newton's Method

In order to show the advantages of the proposed 2-D model in terms of computation time, its performance is compared with a recently published research [12] in Table 3.2.

Table 3.2 2-D Real-time performance comparison with Newton's method [12].

Simulation	Simulation duration	Simulation time cost	Ratio
The proposed model with N=32 (2.5 GHZ CPU)	800 s	297 s	37.12%
	1200 s	473s	39.41%
Model in [12] with N=25 (2.4 GHZ CPU)	800 s	431 s	53.87%
	1200 s	611 s	50.91%

The pseudo-2D fuel cell model in [12] uses Newton's method to solve the ordinary differential equations, which describe reactant transport only along the straight channel direction. It can be seen from Table 3.2 that, the proposed full-2D real-time modeling approach can achieve a faster computation speed with a more comprehensive two-dimensional consideration and a slightly larger mesh number. It is also important to mention that, the model in [12] uses a commercial software solver (Matlab/Simulink), while the developed iterative solver is completely independent of commercial platform, and can be easily implemented to any embedded controller of PEMFC systems.

3.4.3.2 Comparison with Gaussian Elimination Method

As mentioned before, as the proposed approach uses a special form of elimination and solves the tridiagonal system equations in backward substitution, the arithmetic complexity of tridiagonal equations system can thus be exponentially reduced compared to the classical Gaussian elimination method. This advantage is particularly evident for a larger mesh number. To show further this advantage, another Gaussian elimination based 2-D real-time modeling approach [13] has been used for performance comparison.

It can be seen from the model computation time of different mesh numbers in Table 3.3 that, the model CPU execution time in [13] is faster than that in this paper for a low mesh number ($N<64$). However, the CPU execution time in [13] significantly increases with increasing of mesh number. It can be observed that, when the mesh number $N \geqslant 328$, the CPU execution time could exceed 100 ms. And as mentioned in [13], for a large mesh number, the CPU execution time could exceed 1 second, thus making this model not suitable for real-time model-based controller applications.

Table 3.3 2-D Real-time performance comparison with Gaussian method [13].

Mesh number	104	200	328
Execution time	6.3 ms	39.5 ms	162 ms

Although the model CPU execution time in this paper is higher than that in [13] for a low mesh number, the execution time quasi-linearly increases with mesh number when the mesh number N is larger than 128. And it can be observed that from Table 3.3, when the mesh number N=600, the execution time is 50.429 ms. Such short CPU execution time further demonstrates the effectiveness of the proposed modeling approach, especially for large mesh numbers.

3.5 Conclusion

A 2-D multi-physical real-time model of proton exchange membrane fuel cell has been presented in this chapter. An innovative non-uniform 2-D mesh grid method is proposed for real-time simulation performance consideration. In order to efficiently calculate the physical quantities distribution in 2-D plane, an iterative solver is also developed in the model. The proposed original iterative solver algorithm is composed by three interactive computational loops and uses a robust convergence method for real-time computation.

The proposed 2-D model has been tested in a RT-LAB real-time simulator and has been experimentally verified using a Ballard NEXA 1.2kW PEMFC stack. The experimental results demonstrate the practical feasibilities of the proposed 2-D model for advanced real-time control of PEMFC systems with a control loop time level on the order of milliseconds [10] [14]. Such short execution time of the proposed 2-D model makes control decisions and actions based on the predicted local phenomena and spatial distribution physical variables inside the fuel cells.

3.6 Reference

[1] C. Restrepo, "Simplified mathematical model for calculating the oxygen excess ratio of a PEM fuel cell system in real-time applications", *IEEE Trans. Ind. Electron.*, vol. 61, no. 6, pp. 2816-2825, Jun. 2013.

[2] J. H. Jung, S. Ahmed and P. Enjeti, "PEM fuel cell stack model development for real-time simulation applications", *IEEE Trans. Ind. Electron.*, vol. 58, no. 9, pp. 4217-4231, Sep. 2011.

[3] F. Gao, B. Blunier, A. Miraoui, A. El-Moudni, "A multiphysic dynamic 1-d model of a proton-exchange-membrane fuel-cell stack for real-time simulation," *IEEE Trans. Ind. Electron.*, vol. 57, no.6, pp. 1853-1864, Jun. 2010.

[4] A. M. Colclasure, B. M. Sanandaji, T. L. Vincent, and R. J. Kee, "Modeling and control of tubular solid-oxide fuel cell systems. I: Physical models and linear model reduction," *J. Power Sources*, vol. 196, no. 1, pp. 196- 207, Jan. 2011.

[5] S. um, C. Yang and K. Chen, "Computational Fluid Dynamics Modeling of Proton Exchange Membrane Fuel Cells," *J. Electrochem. Soc.*, vol. 147, no. 12, pp. 4485-4493, 2000.

[6] B. R. Sivertsen and N. Djilali, "CFD-based modelling of proton exchange membrane fuel cells", *J. Power Sources*, vol. 141, no. 1, pp. 65-78, Feb. 2005.

[7] G. W. Stewart, *Matrix Algorithms: Volume II: Eigensystems*. Society for Industrial and Applied Mathematics, 2001.

[8] N. Nguyen, P. Milanfar, G. Golub, "Efficient generalized cross-validation with applications to parametric image restoration and resolution enhancement," *IEEE Trans. Image Process.*, vol. 10, pp. 1299-1308, 2001.

[9] V. Mathiesen, T. Solberg, B. H. Hjertager, "Predictions of gas/particle flow with an Eulerian model including a realistic particle size distribution," *Powder Technology*, vol. 112, pp. 34-45, 2000.

[10] D. Zhou, F. Gao, E. Breaz, A. Ravey, A. Miraoui, "Tridiagonal Matrix Algorithm for Real-Time Simulation of a 2-D PEM Fuel Cell Model," *IEEE Trans. Ind. Electron.*, Accepted and to be published;

[11] F. Gao, M. Simoes, B. Blunier and A. Miraoui, "Development of a quasi 2-D modeling of tubular solid-oxide fuel cell for real-time control," *IEEE Trans. Energy Convers.*, vol. 29, no.29, pp. 9– 19, March. 2013.

[12] A. Goshtasbi, B. Pence, T. Ersal, "Computationally Efficient Pseudo-2D Non Isothermal Modeling of PEM Fuel Cells with Two-Phase Phenomena," *J. Electrochem. Soc.*, vol. 163, pp. F1412–1432, 2016.

[13] P. Massonnat, F. Gao, R. Roche, D. Paire, D. Bouquain, "Multi-physical, multidimensional real-time PEM fuel cell modeling for embedded applications," *Energy Convers. Manage.*, vol. 88, pp. 554-564, 2014.

[14] D. Zhou, F. Gao, E. Breaz, A. Ravey, A. Miraoui, "Development of a Multi-physical 2-D model of PEM Fuel Cell for Real-Time Control," *IEEE Industry Applications Society Annual Meeting*, Hyatt Regency Cincinnati, OH, Oct. 1-5, 2017.

Chapter IV: Degradation Prediction of Proton Exchange Membrane Fuel Cell Stack

Two different degradation prediction methods for proton exchange membrane fuel cell (PEMFC) performance are proposed in this chapter. In the first part, a novel degradation prediction approach for proton exchange membrane fuel cell (PEMFC) performance is proposed based on a multi-physical aging model with particle filter and extrapolation approach. The proposed multi-physical aging model considers major internal physical aging phenomena of fuel cells, including fuel cell ohmic losses, reaction activity losses, and reactants mass transfer losses. By knowing a prior the parameter-function pairs, even when the acquired training data is extremely limited, this physical-based method is still able to provide acceptable results at immediate short prediction time range.

However, the first physical-based method cannot be used in the on-line prognostic applications, since this single-step prognostic method makes predictions for a fixed horizon only. In order to improve the proposed method, iteration-based prediction methods are particularly useful to achieve a better performance in the on-line prognostic applications.

For this purpose, an iteration-based prediction algorithm for performance degradation of PEMFC is proposed in the second part of this chapter. A novel approach using the moving window method is applied, in order to dynamically retrain the models during the forecasting process with new data inputs for iterative data training at next prediction step. In addition, since the proposed hybrid prognostic method is based on a combination of model-based and data-driven prognostic methods, it is able to capture both the fade trend and non-linear features observed in the fuel cell voltage degradation data.

4.1 Literature Review

As an advanced concept, the Prognostic and Health Management (PHM) of PEMFC is designed to minimize maintenance costs while increasing operational availability and utilization of PEMFC [1]. As a key process of PHM, the prognostics use a set of monitoring data from actual life cycles of PEMFC system, in order to indicate the future degradation trends as well as its current state of health [2]. Based on the degradation trends, the

PEMFC system impending faults and remaining useful life (RUL) can be predicted, the advent of failure can be further forecasted [3].

Generally speaking, there are two main approaches for degradation prediction: model-based methods [4]-[6] and data-driven methods [7]-[12]. Model-based methods consider the real physical aging phenomena during the PEMFC degradation process. Although model-based methods need large computations and complex physical model, it can predict not only the system degradation trend (fuel cell output voltage decay over time), but also the information about the internal physical parameters during the degradation process. However, as mentioned before, the complexity of physical degradation phenomena makes it very difficult to build a reliable physical model of degradation. Several PEMFC model-based aging prediction methods can be found in the literature.

Jouin *et al.* [4] present a prognostics framework to provide RUL predictions based on three voltage degradation empirical models: a linear, an exponential and a log-linear model. However, the empirical voltage degradation models are too simplified, the fuel cell operating conditions, such as operating current and temperature are also not taken into account.

Bressel *et al.* [5] have proposed an empirical model of degradation. Based on Extended Kalman Filter (EKF) method, the proposed prognostic algorithm is able to estimate the PEMFC state of health and to predict its RUL under a variable load profile. However, the electrochemical kinetics in the proposed aging model is described by Tafel equation. Under a variable load profile, this aging model can lead to a large error of electrochemical activation loss, especially for small current values.

Chen *et al.* [6] have developed a PEMFC lifetime quick evaluation method by taking the various changes of the operating condition into consideration. This method can achieve the RUL prediction in real-time applications. However, the fuel cell performance degradation is described by a linear aging model, which cannot truly reflect the non-linear aging trend. Indeed, the fuel cell is a multi-physical system (electrochemical, fluidic, and thermal). Therefore, it is necessary to take into account aging process in different physical domains.

In the proposed model-based method, a multi-physical aging model is developed to consider major internal physical aging phenomena of fuel cells, including Ohmic losses, reaction activity losses, and reactants mass transfer losses. In addition, the Butler-Volmer

equation is used in the proposed aging model to accurately calculate the electrochemical activation loss for all possible values of PEMFC stack current.

On the other hand, the data-driven methods use pattern recognition, statistical or machine learning techniques, such as Artificial Neural Network (ANN) [7], Support Vector Machine (SVM) [8], and adaptive neuro-fuzzy inference system (ANFIS) [9], to track and predict the system non-linear characteristics. Compared with model-based approach, data-driven method can be easily implemented without specific knowledge of physical degradation.

Marra *et al.* [10] proposed a neural network estimator of solid oxide fuel cells for its diagnostic. The proposed degradation estimator is trained based on a set of experimental data, in which includes stack current, temperature and reactant gas mass flow rate.

Mao *et al.* [11] investigated sensor selection algorithms for prognostic of PEMFC. With the identified optimal sensor, an adaptive neuro-fuzzy inference system (ANFIS) is used to predict the performance of fuel cell system.

Ibrahim *et al.* [12] proposed a data-driven approach for PEMFC prognostic based on Wavelet Transform technique. The prediction process consists of decomposition and reconstruction. This approach is able to predict the future power and estimate RUL under static and dynamic operating conditions of PEMFC system.

However, a common drawback of these data-driven methods is that the degradation trend and non-linear behaviors cannot be simultaneously captured, thus make them inaccurate for prognostic. The proposed hybrid prognostic method is able to capture both the fade trend and non-linear features observed in the fuel cell voltage degradation data. In addition, a novel approach using the moving window technique is applied in order to iteratively update the prediction process when the newly measured data become available. This iteration-based prediction method is particularly useful to achieve a more accurate prediction when the initial training samples are limited.

4.2 Degradation Prediction Based on Multi-physical Aging Model with Particle Filter Approach

In this section, a multi-physical aging model of a PEMFC is developed at first. The presented aging model considers different physical aging phenomena including fuel cell ohmic losses, reaction activity losses and reactants mass transfer losses. The proposed aging model is then initialized by fitting the PEMFC polarization curve at the beginning of lifetime.

During the prediction process, the aging dataset is then divided into two parts: learning and prediction phases. The particle filter framework is used to study the degradation characteristics and update the aging parameters during the learning phase. The suitable fitting curve functions are then selected to satisfy the degradation trends of trained aging parameters, and used to further extrapolate the future values of aging parameters in the prediction phase. By using these extrapolated aging parameters, the prediction results are thus obtained from the proposed aging model. Three experimental validations with different aging testing profiles have been performed. The results demonstrate the robustness and advantages of the proposed prediction method.

4.2.1 Description of Aging phenomena

In this section, the presented aging model is developed based on a previously developed multi-physical PEMFC model [13] [14]. In this model, each single cell is also divided into seven different element layers, and each layer modeling covers three physical domains: electrical, fluidic and thermal domain. It should be noted that, the time constant of aging process is much higher than the other physical dynamics in PEMFC system (thermal dynamic, membrane water dynamic, etc.). Thus, all the physical dynamics are removed in the proposed aging model compared to the original multi-physical model.

In order to model the aging process over PEMFC operating lifetime, the proposed model uses time-variant modeling coefficients to describe three most important aging phenomena in different physical domains [15] [16], including fuel cell ohmic losses, reaction activity losses in electrical domain, and reactants mass transfer losses in fluidic domain, as shown in the figure 4.1.

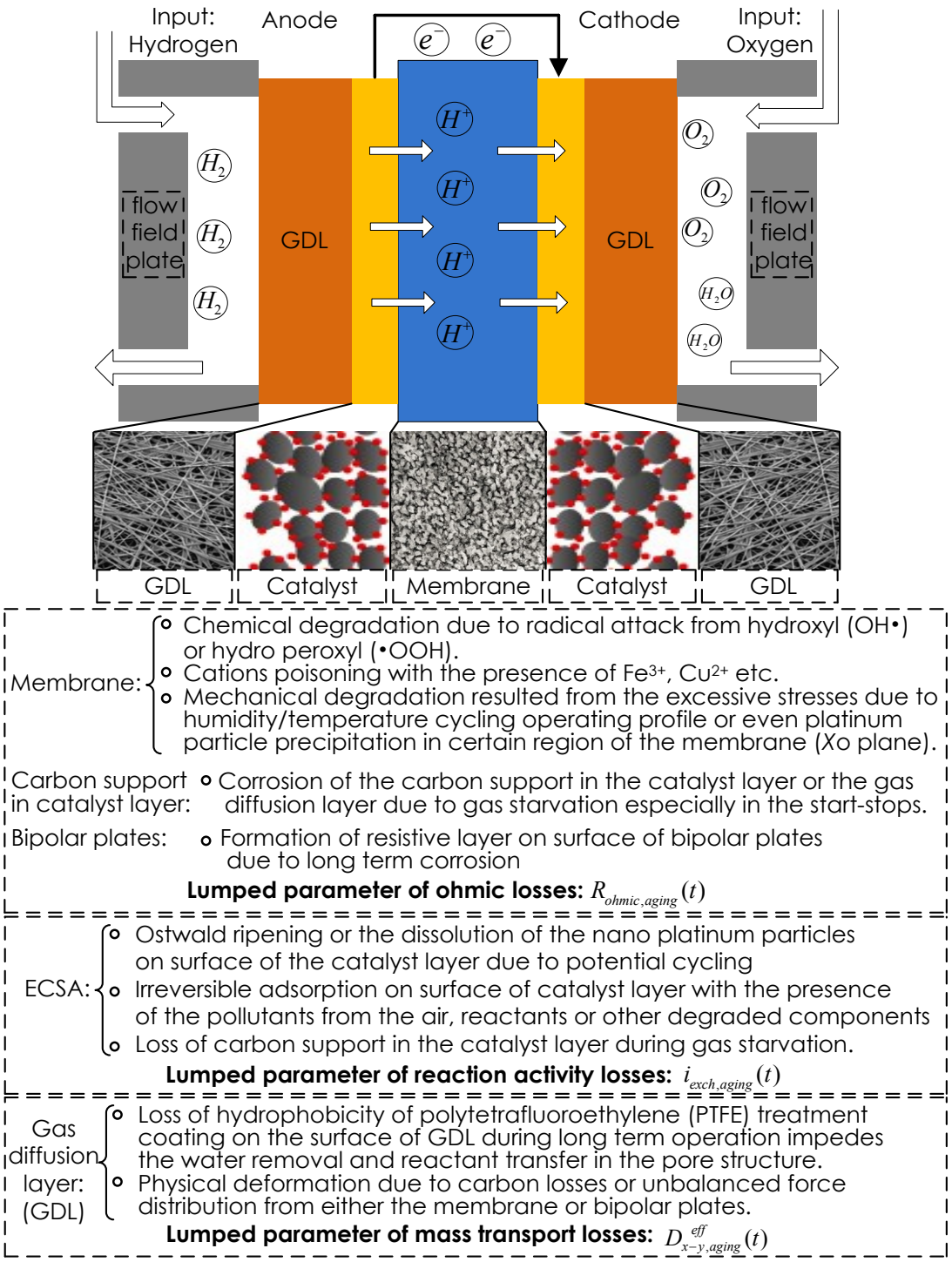

Figure 4.1 Degradation mechanisms considered in the individual lumped aging parameters.

4.2.1.1 Aging Parameter Membrane Resistance

The first aging phenomenon considered in the proposed aging model is described by ohmic losses of fuel cell, including layer contact resistance, electrode resistance and membrane resistance [16]. More explanations and causes of fuel cell ohmic losses are

shown in the figure 4.1 (first group). In order to describe the fuel cell ohmic losses during the degradation process, the first lumped aging parameter ohmic resistance (Ω) has been proposed as following:

$$R_{ohmic,aging}(t) = R_{ohmic,aging,0}\big(1 + \alpha(t)\big) \tag{4.1}$$

where the aging coefficient $\alpha(t)$ indicates the aging degree of ohmic resistance.

4.2.1.2 Aging Parameter Exchange Current Density

In order to describe the reaction activity losses during fuel cell operation, the second lumped aging parameter exchange current density $i_{exch,aging}$ (A/m^2) has been proposed with the following form:

$$i_{exch,aging}(t) = i_{exch,aging,0}\big(1 + \beta(t)\big) \tag{4.2}$$

where the aging coefficient $\beta(t)$ reflects the aging degree of exchange current density over time. As a parameter who represents electrode kinetics, the exchange current density determines how easily the reaction can occur on the electrodes. The reaction activity losses may result from degradation of active electrode surface area, Nafion in contact with active area, or loss of catalyst material [16]. More explanations and causes of reaction activity losses are shown in the figure 4.1 (second group).

4.2.1.3 Aging Parameter Gas Diffusion Coefficient

In order to describe the losses of reactants mass transfer during fuel cell aging, the third lumped aging parameter gas diffusion coefficient $D^{eff}_{GDL,x-y,aging}$ (m^2/s) between the species x and y has been proposed under the following form:

$$D^{eff}_{GDL,x-y,aging}(t) = D^{eff}_{GDL,x-y,aging,0}\big(1 + \gamma(k)\big) \tag{4.3}$$

where the aging coefficient $\gamma(k)$ reflects the aging degree of fuel cell gas diffusion layer material that influences the reactants mass transfer. The losses of reactants mass transfer may result from the corrosion of electrode supporting material, increase of tortuosity due to catalyst particle ripening, or more difficult water removal due to degradation of polymer material [16]. More explanations and causes of reactants mass transfer losses are shown in the figure 4.1 (third group).

4.2.2 Estimation Method

Compared with the Extended Kalman filter (EKF) which only focuses on linear systems and Gaussian noise [17], [18], the particle filter (PF), which use the Monte Carlo sequence for solving integration problem in Bayesian estimation, has significantly better

estimation accuracy when non-linear battery models are used, since it focus on approximating the solution for non-linear and non-Gaussian system [19]-[22].

In this section, the state space representation of the proposed model is presented at first. Then, the Bayesian estimation method is introduced, followed by a detailed description of particle filter algorithm.

4.2.2.1 State Space Model for Aging

In order to give a clear structure of the proposed aging model, the proposed non-linear model can be written in the form of state-space representation as follows:

$$\begin{cases} x_k = x_{k-1} + w_{k-1} \\ y_k = h(x_k, u_k) + v_k \end{cases} \tag{4.4}$$

where x_k represents the state variable of system at time k, y_k the observed variables of system, u_k the input variables of system, the non-linear system observation equation h can be derived using the formula of the electrical and fluidic domain modeling equations presented in chapter I. w_k and v_k the process and observation noises respectively. The system state x_k includes three aging parameters:

$$x_k = [\alpha(k), \beta(k), \gamma(k)]^T \tag{4.5}$$

The schematic diagram of non-linear function h is shown in the figure 4.2.

It can be seen from the figure 4.2 that, three aging coefficients are considered as the system state variables. The initial values of the three aging parameters $R_{ohmic,aging,0}$, $i_{exch,aging,0}$, and $D^{eff}_{GDL,x-y,aging,0}$ are obtained by fitting the polarization curve of PEMFC at the beginning of lifetime (described hereafter in section 4.2.3.1). Other modeling parameters (geometrical values or physical properties of the Ballard Nexa 1.2kW fuel cell stack) can be obtained in the previous work [13] [14].

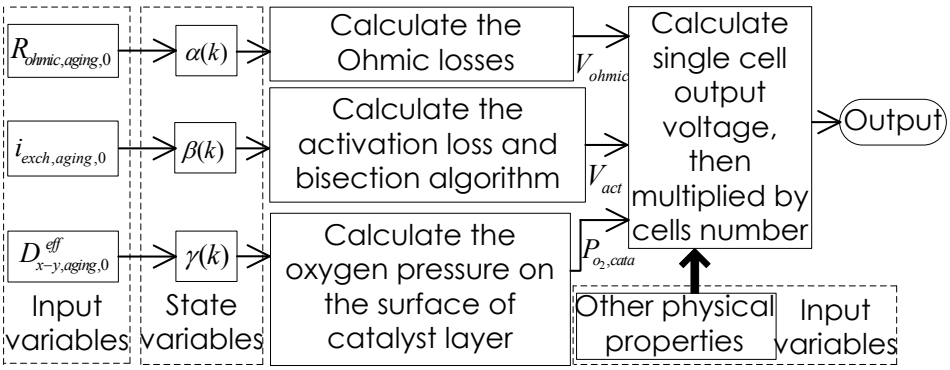

Figure 4.2 Schematic diagram of proposed aging model.

4.2.2.2 Bayesian Estimation

In the framework of Bayesian estimation, the state variable x_k in the state space of aging model (equation 4.1- 4.3) is estimated based on the observation sequence $y_{0:k} = \{y_i, i = 0,1,2 \dots, k\}$. Then, the optimal estimation of x_k can be written in the form of the conditional expectation:

$$E(x_{0:k}|y_{0:k}) = \int x_{0:k} p(x_{0:k}|y_{0:k}) d\, x_{0:k} \tag{4.6}$$

The main idea of Bayesian importance sampling is that, a set of random sample particles, which are sampled from the known proposal distribution $q(x_{0:k}|y_{0:k})$, are used to approximate the posterior probability density function $p(x_{0:k}|y_{0:k})$. Thus, $E(x_{0:k}|y_{0:k})$ can be rewritten as:

$$E(x_{0:k}|y_{0:k}) = \int x_{0:k} \frac{p(x_{0:k}|y_{0:k})}{q(x_{0:k}|y_{0:k})} q(x_{0:k}|y_{0:k}) d\, x_k \tag{4.7}$$

Then the Summation form of equation 4.7 can be expressed by:

$$E(x_{0:k}|y_{0:k}) = \frac{\frac{1}{N}\sum_{i=1}^{N} x_{0:k}^i w(x_{0:k}^i)}{\frac{1}{N} w_t(x_{0:k}^i)} = \sum_{i=1}^{N} x_{0:k}^i \tilde{w}(x_{0:k}^i) \tag{4.8}$$

where $x_{0:k}^i$ are the particles sampling from $q(x_{0:k}|y_{0:k})$, $\tilde{w}(x_{0:k}^i)$ are the normalized form of importance weights $w(x_{0:k})$, which can be expressed by:

$$w(x_{0:k}) = \frac{p(y_{0:k}|x_{0:k}) p(x_{0:k})}{q(x_{0:k}|y_{0:k})} \tag{4.9}$$

Bayesian importance sampling is an effective method using Monte Carlo sequence. However, each step of importance weights calculation depends on all the previous observations, thus its computation is increasing with time. In order to avoid this deficiency, the sequential importance sampling is proposed. In this case, the importance weights are calculated recursively, and the proposal distribution can be rewritten as:

$$q(x_{0:k}|y_{0:k}) = q(x_k|x_{0:k-1}, y_{0:k}) q(x_{0:k-1}|y_{0:k-1}) \tag{4.10}$$

From equation 4.10, the importance weights at time k-1 can be described as follows:

$$w_{k-1} = \frac{p(y_{0:k-1}|x_{0:k-1}) p(x_{0:k-1})}{q(x_{0:k-1}|y_{0:k-1})} \tag{4.11}$$

From equation 4.10 and 4.11, the importance weights at time k can be described as follows:

$$w_k = \frac{p(y_{0:k}|x_{0:k})p(x_{0:k})}{q(x_k|x_{0:k-1}, y_{0:k})q(x_{0:k-1}|y_{0:k-1})} \tag{4.12}$$

Thus, the relationship between $w_k$and w_{k-1} can then be expressed by:

$$w_k = w_{k-1}\frac{p(y_{0:k}|x_{0:k})p(x_{0:k})}{p(y_{0:k-1}|x_{0:k-1})p(x_{0:k-1})q(x_k|x_{0:k-1}, y_{0:k})} = w_{k-1}\frac{p(y_k|x_k)p(x_k|x_{k-1})}{q(x_k|x_{0:k-1}, y_{0:k})} \tag{4.13}$$

It should be noted that the system state variables follow a first order Markov process, and each observation are statistically independent.

4.2.2.3 Particle Filter Framework

From the previous analysis of Bayesian estimation based on the sequential importance sampling, a detailed particle filter algorithm can be described as follows:

1) Initialization: the set of particle samples is obtained from the initial distribution at time t=0: $x_0^i \sim p(x_0), i = 1,2,\dots,N$, where N is the number of particles.

2) Importance sampling: the proposal distribution is generated by:

$$x_k^i \sim q\left(x_k^i | x_{0:k-1}^i, y_{0:k}\right) \tag{4.14}$$

3) Weights calculation: the state estimation is optimal with the assumption of $q\left(x_k^i | x_{0:k-1}^i, y_{0:k}\right) = q\left(x_k^i | x_{k-1}^i, y_k\right)$. It means that probability density function only depends on x_{k-1} and y_k, then each sample particle x_k^i can be obtained. Each sample particles weights can be calculated from equation 4.12 and 4.13:

$$w_k^i = w_{k-1}^i \frac{p\left(y_k | x_k^i\right)p\left(x_k^i | x_{k-1}^i\right)}{q\left(x_k^i | x_{k-1}^i, y_k\right)} \tag{4.15}$$

The importance weight at time t=0 is set to $1/N$.

4) Normalize the weights: the set of new particle sample is obtained by normalized weights:

$$\tilde{w}_k^i = w_k^i / \sum_{i=1}^{N} w_k^i \tag{4.16}$$

5) Re-sampling: the effective sample size is defined by: $N_{eff} = 1/\sum_{i=1}^{N}\left(w_k^i\right)^2$, the re-sampling step is performed when N_{eff} is smaller than the given threshold N_{th}.

6) State prediction: calculate the state by the equation:

$$\hat{x}_k = \sum_{i=1}^{N} \tilde{w}_k^i x_k^i \tag{4.17}$$

4.2.3 Prediction Methodology Implement

In this section, the proposed model-based PEMFC performance degradation prediction method is given in detail. The initialization of three aging parameters is performed based on the initial polarization curve of PEMFC. Then, the proposed prediction method is divided into two stages: learning and prediction phases. During the learning phase, the particle filter estimator studies the system non-linear behavior, and at the same time updates the corresponding aging parameters. Based on these updated aging parameters, suitable fitting curve functions are then selected to extrapolate the values of aging parameters in the prediction phase. At last, by using these extrapolated aging parameters, the proposed aging model predicts the PEMFC degradation voltage in prediction phase.

4.2.3.1 Initialization of Aging Parameters

The performance of the proposed prediction method depends strongly on the initial estimation of aging parameters. In order to accurately estimate the initial values of aging parameters, these values are determined based on the reliable physical equations and experimental calibrations.

4.2.3.1.1 Initialization of Aging Parameter Ohmic Resistance

At the beginning of PEMFC lifetime, the ohmic losses are considered only in the membrane, the electrode resistance and layer contact resistance are negligible. Thus, the initial value of ohmic resistance can be calculated by the equation:

$$R_{ohmic,aging}(0) = \frac{\int_0^{\delta_{mem}} r_{mem} dz}{A_{mem}} \tag{4.18}$$

where δ_{mem} is the thickness of the membrane (m), A_{mem} is the membrane section surface (m^2), r_{mem} is the membrane resistivity and is highly dependent on water content $\lambda(z)$ in polymer membrane, where $z \in [0(anode), \delta_{mem}(cathode)]$. More detailed information about ohmic losses and water content equations can be found in [13]. With the membrane properties data given in [13], the initial value of first lumped aging parameter $R_{ohmic,aging}(0)$ is around 2.1e-03 (Ω).

4.2.3.1.2 Initialization of Aging Parameter Exchange Current Density

The initial value of exchange current density $i_{exch,aging}$ is calculated by the following equation:

$$i_{exch,aging}(0) = \gamma_c \cdot P_{O_2,cata}^{\beta_c} \cdot e^{-\frac{E_c}{RT}\left(1-\frac{T_{cata}}{298.15}\right)} \tag{4.19}$$

where $P_{O_2,cata}$is the oxygen pressure (atm) at the interface of cathode catalyst layer, γ_c and β_c are two empirical parameters need to be identified through fuel cell experimental tests, E_c is the oxygen activation energy at electrode platinum interface (J/mol). With $\gamma_c = 2.42$, $\beta_c = 2.12$, the initial value of second lumped aging parameter $i_{exch,aging}(0)$ is around 0.1154 (A/m2).

4.2.3.1.3 Initialization of Aging Parameter Diffusion Coefficient

3) Initialization of $D^{eff}_{GDL,x-y,aging}$: The initial value of diffusion coefficient between species x and y $D^{eff}_{GDL,x-y,aging}$ is calculated by the equation [13]:

$$D^{eff}_{GDL,x-y,aging}(0) = \frac{1}{P_{tot}} \cdot a \cdot \left(\frac{T_{GDL}}{\sqrt{T_{crit,x}T_{crit,y}}}\right)^b \cdot \left(P_{crit,x}P_{crit,y}\right)^{\frac{1}{3}} \cdot \left(T_{crit,x}T_{crit,y}\right)^{\frac{12}{5}} \cdot \left(\frac{10^{-3}}{M_x} + \frac{10^{-3}}{M_y}\right)^{\frac{1}{2}} \cdot \varepsilon^{\iota} \quad (4.20)$$

where P_{tot} is the total pressure of species (atm), T_{crit} is the critical temperature of species (K), P_{crit} is the critical pressure of species (atm), and M is the molar mass of species (kg/mol). The coefficients a and b depend on whether one of the species is a polar gas or not and are determined accordingly, ε is the porosity of the GDL and ι is the GDL tortuosity. With the characteristic data of gas diffusion layer given in [13], the initial value of third lumped aging parameter $D^{eff}_{GDL,x-y,aging}(0)$ is around 6.7e-06 (m2/s).

4.2.3.1.4 Genetic Algorithm

In order to demonstrate the modeling accuracy and identify the initial values of aging parameters, the proposed multi-physical aging model is used to fit the experimental measurement of polarization curve at the beginning of PEMFC lifetime. As a commonly used strategy, the Genetic Algorithm (GA) is particularly suitable for such multi-parametric and non-linear system. The purpose of GA is to find optimal solution for objective function, defined as follow:

$$f\left(\hat{\chi}_k^g\right) = min\left\{\sum_{t=T_0}^{T}\left[\left(Y_k - \hat{Y}_{ESPM}\left(\hat{\chi}_k^g\right)\right]^2\right\} \quad (4.21)$$

where $\hat{\chi}_k^g$ are the estimated parameter values at time k in the generation g, Y_k is the measured output value at time k, and $\hat{Y}\left(\hat{\chi}_k^g\right)$ is the predicted output value.

The flow diagram of aging parameters initialization using GA algorithm is shown in the figure 4.3. The main idea of GA is to generate a population of solutions and then to improve it using techniques of natural evolution, such as inheritance, mutation, selection,

and crossover method. This generational process is repeated until an appropriate solution can satisfy (optimize) the objective function. More detailed content about GA can be found in [23] [24].

As shown in the figure 4.3, the inputs of GA include fuel cell stack geometry parameters and physical properties, as well as operating condition of auxiliary components. In addition, the numeric variation range of above each aging parameter has been set to ±5% of their calculated initial values for the GA tuning.

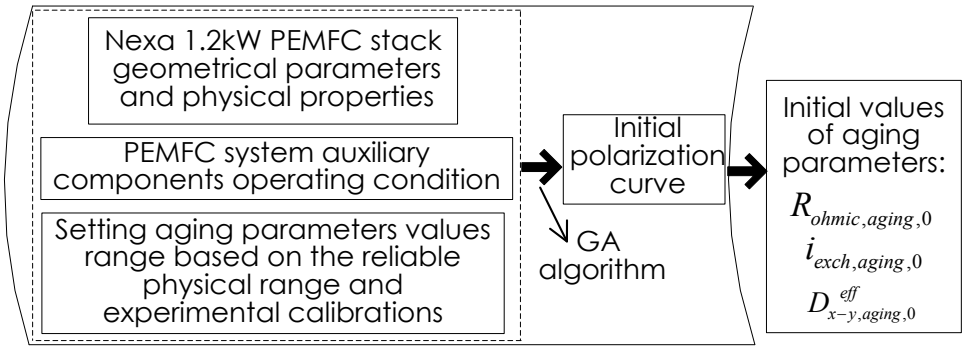

Figure 4.3 Flow diagram of GA for fitting the initial polarization curve.

Figure 4.4 shows the polarization curve measured at PEMFC beginning of lifetime, and the GA fitting result of the proposed model. It can be seen from the figure 4.4 that, the identified aging model output fits very well to the experimental measurement over the entire current range by using the GA approach (the fitness value is 97.27%). The identified initial values of three aging parameters are, respectively, $R_{ohmic,aging,0}$=2.081e-03 (Ω), $i_{exch,aging,0}$=0.1149 (A/m²), and $D^{eff}_{GDL,x-y,aging,0}$=6.839e-06 (m²/s). These three initial values are further used for particle filter to study the degradation characteristics in the learning phase of the proposed aging prediction method.

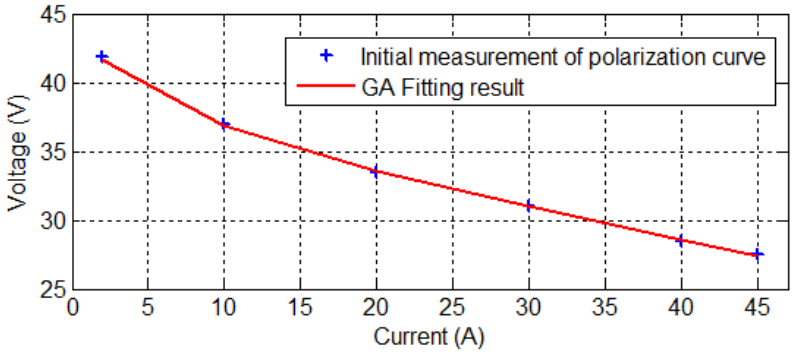

Figure 4.4 Initial measurements of polarization curve and GA fitting results.

4.2.3.2 Prediction Method Design

The proposed model-based prediction method is divided into learning phase and prediction phase. In order to give a detailed flow diagram of proposed algorithm design, the PEMFC experimental degradation voltage dataset and working conditions are presented at first. A Ballard NEXA 1.2 kW commercial PEM fuel cell stack is used in this experimental aging test. As shown in the figure 4.5, the PEMFC stack voltage is measured under a current of 36 A at a temperature of 40 °C. The experimental aging data is measured and recorded every ten minutes during the 400 hours experimental test.

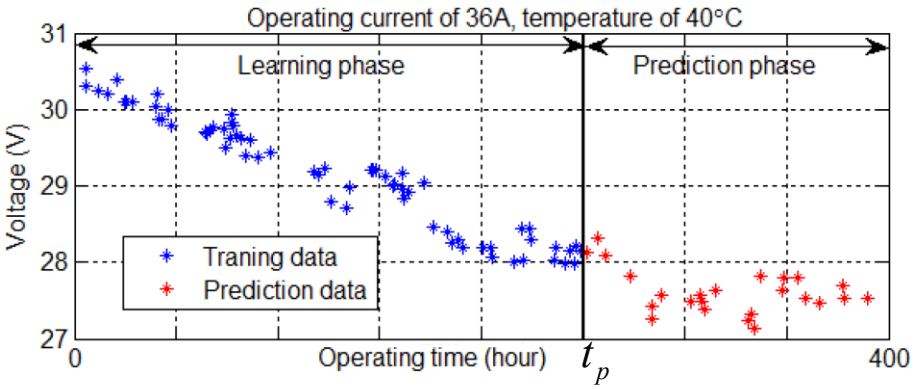

Figure 4.5 Experimental measurements of the fuel cell stack output voltage under a current of 36A at a temperature of 40 °C.

It should be noted that, in order to eliminate the unreliable measurement data points before applying the proposed algorithm, a data post-processing is performed to down-sample the original measured data. Thus, the available measured aging data consists of 91 data points as shown in the figure 4.4. The learning phase point is set to t_p. It means that, by using the proposed prediction method, the aging parameters is trained and updated from 0 h to t_p h, the remaining data between the learning time t_p h and the end time 400 h is thus used to evaluate the consistency of the prediction results from the proposed aging model.

The detailed flow diagram of proposed prediction methodology is shown in figure 4.6. It includes accordingly two parts: learning phase and prediction phase.

For the learning phase, the objective of particle filter is to recursively estimate the state variables x_k based on the initial aging parameters and experimental aging voltage data. It should be noted that, during the particle filter based estimating process, the variance selection of process noise w_k is a compromise problem. A large variance of w_k can provide a set of sample particles with great diversity, and further expands the sampling distribution, while a small variance ensures a sufficiently fast convergence. The

observation noise v_k already exists in the experimental aging data, since the stack voltage is measured by physical sensors.

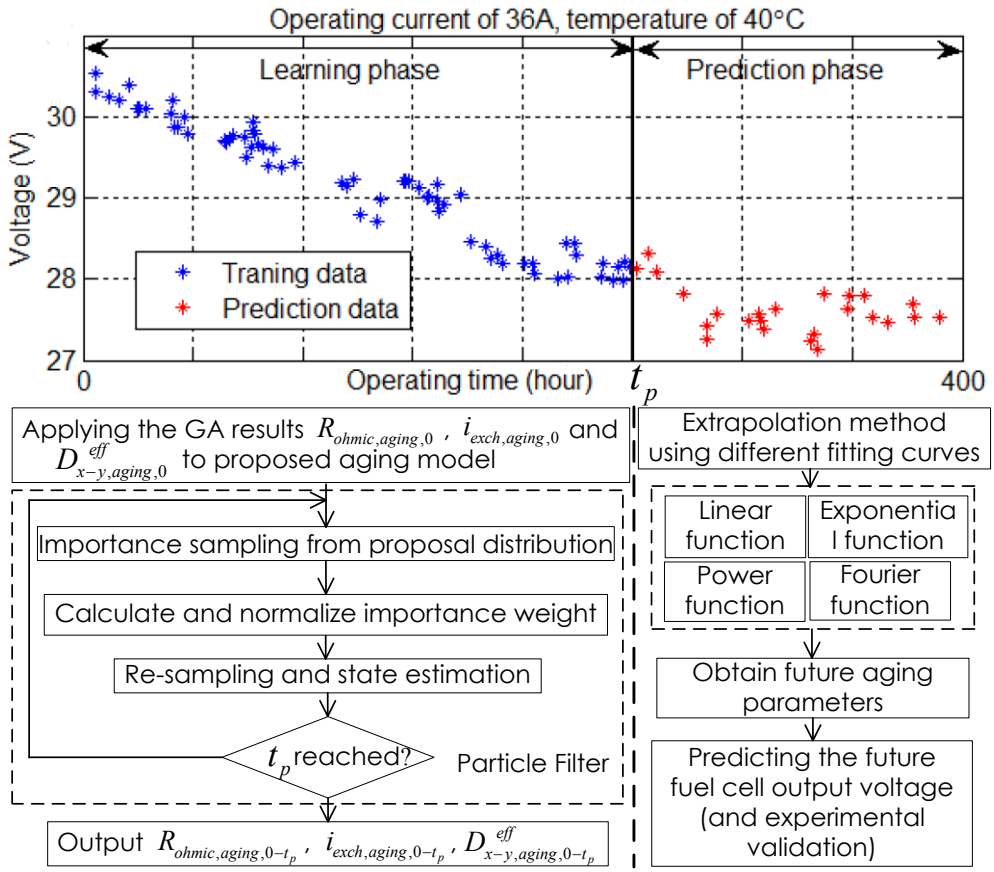

Figure 4.6 Schematic diagram of proposed prediction methodology including learning phase and prediction phases.

The particle filter in the previous learning phase estimates and updates the state variables $x(k)$ at every sampling step, thus the non-linear behaviors of voltage degradation before the learning time t_p h can be fully captured. In order to well represent the captured aging behavior, the multiply exponential function is commonly used in the literature [25]-[28] to describe the degradation trend. Furthermore, linear, exponential, power, and Fourier series functions [29] can also well express the PEMFC aging process under constant current and temperature condition. Since the degradation trends of different aging parameters represent different physical aging progresses and degradation mechanisms, the above-mentioned fitting curve functions should be properly selected for each aging parameter extrapolation, in order to further achieve accurate prediction voltages in the prediction phase.

4.2.4 Experimental Results and Discussions

In this section, a 400 hours experimental degradation voltage dataset is fully investigated to perform the fitting curve function selections at first. Then, based on the selected fitting functions, the proposed prediction method is then applied to 3 other 400 hours PEMFC experimental degradation tests under different operation conditions. The prediction performance evaluation of the proposed approach with shorter duration of learning phase is also shown and discussed at last.

The 4 datasets of Ballard NEXA 1.2 kW commercial PEMFC stacks, used in this thesis, are measured and post-processed under steady-state operation conditions of 12A 30°C, 30A 35°C, 36A 40°C and 44A 40°C, respectively. Four identical NEXA stacks (from same manufacturer batch) are used during experiments and each stack is tested under 400 hours aging experimentation. The detailed operation conditions of 4 NEXA fuel cell stacks are listed in the following table 4.1.

Table 4.1 Operation Conditions of NEXA Fuel Cell Stacks

	Test in section 4.1.4.1	1st test in section 4.1.4.2.1	2nd test in section 4.1.4.2.2	3rd test in section 4.1.4.2.3
Stack type	Ballard NEXA 1.2 kW commercial PEM fuel cell stack			
Operation mode	Dead–end mode			
Air supply	Air blower + filter			
Cooling	Air fan cooled			
Active area	150cm^2			
Fuel supply	99.99% dry H_2 @1.2 bar			
Operating hours	400 hours			
Air stoichiometry	2.0	4.2	2.2	2.0
Stack temperature	40°C	30°C	35°C	40°C
Current density	$0.24\ \text{A/cm}^2$	0.08A/cm^2	$0.20\ \text{A/cm}^2$	$0.30\ \text{A/cm}^2$

4.2.4.1 Fitting Function Selection and Extrapolation Method

In the first experimental aging test, the Ballard NEXA 1.2 kW PEMFC stack runs for 400 hours under 36 A at 40 °C (the dataset is shown in the figure 4.5). The learning phase time t_p is set to 250 h. This experiment aims to find appropriate fitting function for each aging

parameter extrapolation. By applying the proposed prediction method, the particle filter studies the non-linear aging behaviors and updates the aging parameters in the learning phase. Then, an important step of the proposed method is to select appropriate fitting functions, which are used to represent the trends of aging parameters in the learning phase, and further extrapolate the future values of aging parameters in the prediction phase. As mentioned previously, the aging trend behaviors can be well expressed by the following fitting curve functions: multiply exponential, linear, exponential, power, and Fourier function.

Taking the first aging parameter $R_{ohmic,aging}$ as an example. In the learning phase, the particle filter studies the voltages degradation behaviors and updates the parameter $R_{ohmic,aging}$ values, as shown in the figure 4.7 (blue points in the learning phase). The upward tendency of $R_{ohmic,aging}$ in the learning phase can be well described by above-mentioned linear, exponential, power, and Fourier series functions. These four functions also generate different extrapolated values of parameter $R_{ohmic,aging}$ in the prediction phase, as shown in the figure 4.7 (different colors points in the prediction phase).

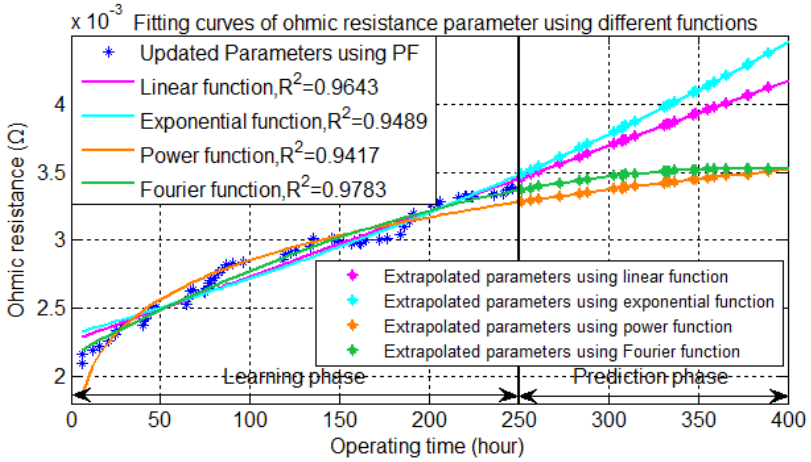

Figure 4.7 Fitting curves of ohmic resistance parameter using different functions.

It can be seen from the figure 4.7 that, although all the four functions can provide good fitting results in the learning phase (high coefficient of determination R^2), the extrapolated parameters have large differences in the prediction phase. For comparison purpose, these different extrapolated values of parameter $R_{ohmic,aging}$ are further used in the proposed aging model. As a consequence, the prediction results of degradation voltage also show difference in the prediction phase, as shown in the figure 4.8.

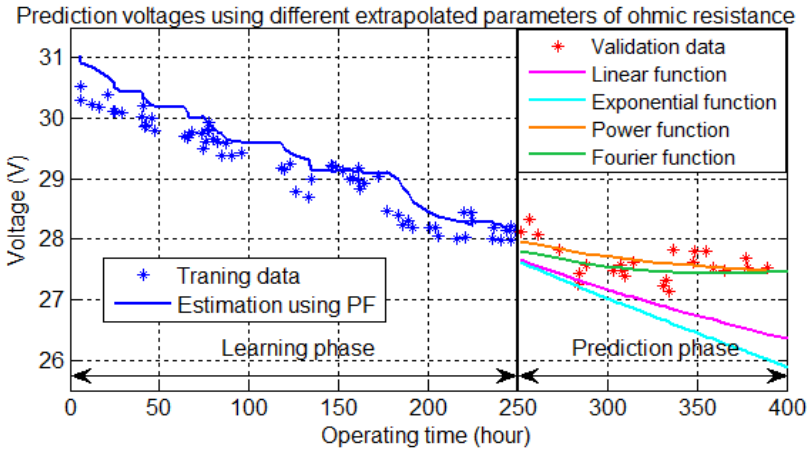

Figure 4.8 Prediction voltage results using extrapolated parameter of $R_{ohmic,aging}$.

In figure 4.8, the voltage curve in the learning phase (blue curve) is estimated by particle filter. The four forecasted voltage curves in the prediction phase are generated by the proposed aging model with the above-mentioned different extrapolated aging parameter $R_{ohmic,aging}$. It can be clearly seen from the figure 4.8 that, the trend of forecasted curves using power function and Fourier function are in good agreement with the measured voltage points, while the linear and exponential functions have relatively large errors. It can be concluded from the prediction results that, compared to linear and exponential functions, power and Fourier functions can reflect more accurately reflect the trend of fuel cell ohmic losses.

The similar function selection process are also used for the other two aging parameters $i_{exch,aging}$ and $D^{eff}_{GDL,x-y,aging}$. Since each aging parameter has four different fitting functions to extrapolation, there are a total of $4^3 = 64$ possible combinations to predict the degradation voltage.

The root mean square error (RMSE) is used to measure the accuracy of all the 64 different prediction results using the above fitting functions selection method. It has been found out that, in order to achieve best forecast performance of prediction curve, the most appropriate extrapolation pairs are:

Power function extrapolation for $R_{ohmic,aging}$:

$$R_{ohmic,aging}(t) = \alpha \cdot t^{\beta} \tag{4.22}$$

Fourier series function extrapolation for $i_{exch,aging}$:

$$i_{exch,aging}(t) = p_1 + p_2\, cos(\omega t) + p_3\, sin(\omega t) \tag{4.23}$$

Multi-exponential function extrapolation for $D^{eff}_{GDL,x-y,aging}$:

$$D^{eff}_{GDL,x-y,aging}(t) = a \cdot exp\,(b \cdot t) + c \cdot exp\,(d \cdot t) \tag{4.24}$$

where the parameters α, β, p_1, p_2, p_3, ω, a, b, c, d are determined by the curve fitting functions. The above three parameter-function pairs are then considered for future study.

4.2.4.2 Experimental Validation: Long Learning Time

In order to experimentally verify the effectiveness of proposed prediction method, three more experimental degradation voltage datasets of the same type of Ballard NEXA 1.2 kW PEMFC stack for 400 h operation under different working conditions of 12A 30°C, 30A 35°C, 44A 40°C are presented respectively, with a learning time t_p of 250 hour.

4.2.4.2.1 First Experiment: PEMFC Operation under 12A at 30°C

In the first experimental aging test, the PEMFC stack runs for 400 hours under a current of 12A at 30°C. By applying the proposed prediction method, the extrapolation results of the aging parameter are shown in figure 4.9.

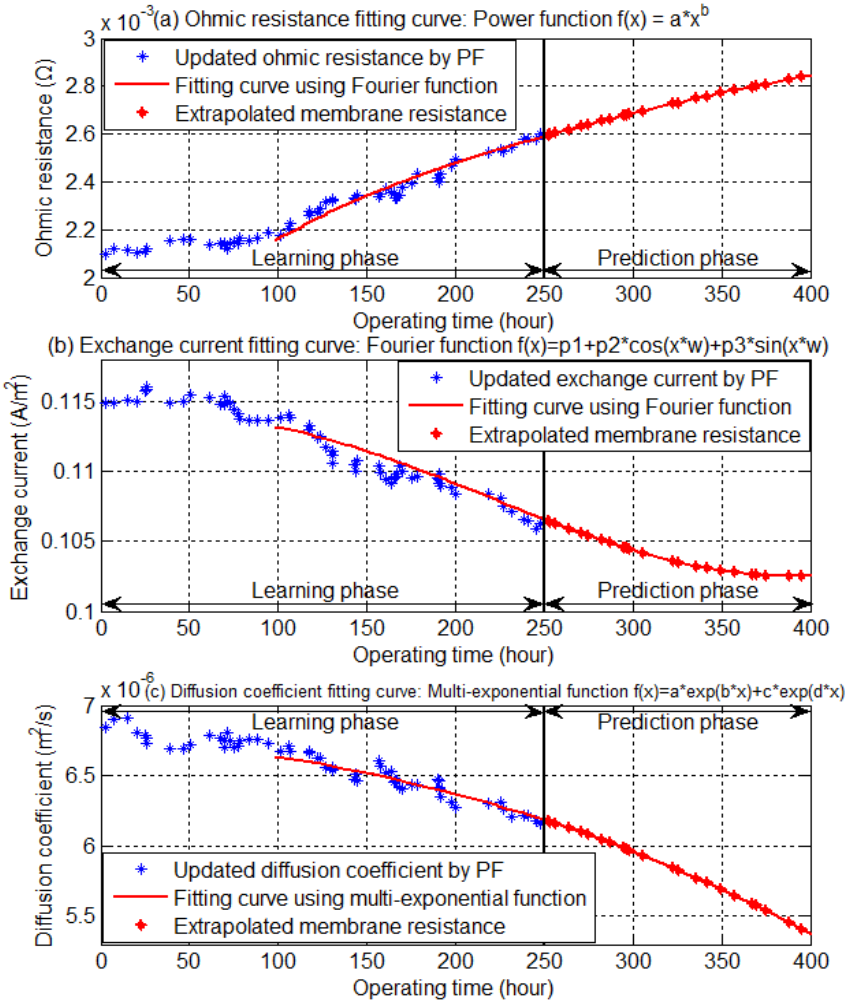

Figure 4.9 Extrapolated result of aging parameters: (a). ohmic resistance. (b). exchange current density. (c). diffusion coefficient. (operating current 12A at 30°C).

It can be seen from the figure 4.9 that, three aging parameters show different non-linear aging characteristics, due to their different physical performance and degradation mechanisms. The prediction results show that under the first PEMFC 400 hours operation under a current of 12A at a temperature of 30°C, the Ohmic resistance increases by more than 39%, the exchange current density and diffusion coefficient decrease by 10% and 23%, respectively. Based on the values of three extrapolated parameters, the proposed aging model outputs the prediction results, as shown in the figure 4.10.

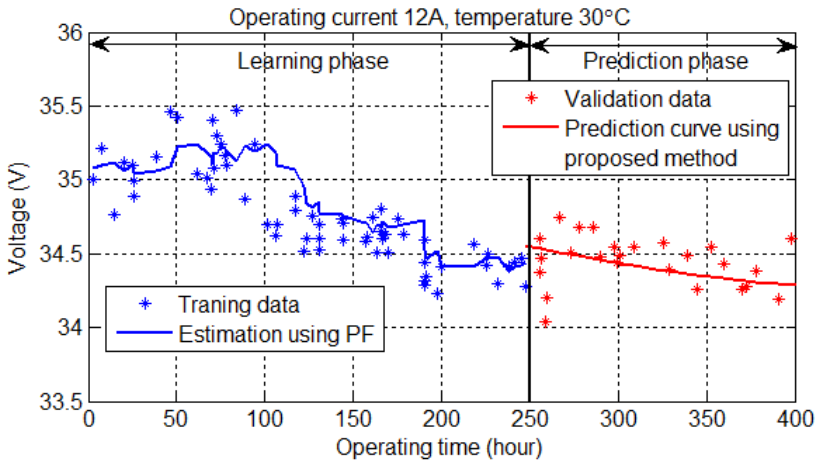

Figure 4.10 Prediction result (current 12A at 30°C, learning time is set to 250 h).

It can be seen from the figure 4.10 that, the predicted voltages can follow the trend of the non–linear experimental data set with a great accuracy. The root mean square error (RMSE) and mean absolute percentage error (MAPE) of prediction result are 0.1857 and 0.0042, respectively.

4.2.4.2.2 Second Experiment: PEMFC Operation under 30A at 35°C

In the second experimental aging test, the PEMFC stack runs for 400 hours under a current of 30A at 35°C. By applying the proposed prediction method, the extrapolation results of the aging parameter and voltage degradation prediction result are shown in figure 4.11 and figure 4.12, respectively.

It can be seen from the figure 4.11 that, three aging parameters show again different non-linear aging characteristics. The prediction results show that, for the second experimental aging test, the Ohmic resistance increases by more than 57%, the exchange current density and diffusion coefficient decrease by 12% and 29%, respectively. Then, based on the values of three extrapolated parameters, the proposed aging model outputs the prediction voltages. Figure 4.12 clearly points out again that,

the proposed prediction method shows a precise conformity with the validation data. The RMSE and MAPE of prediction result are 0.1865 and 0.0052, respectively.

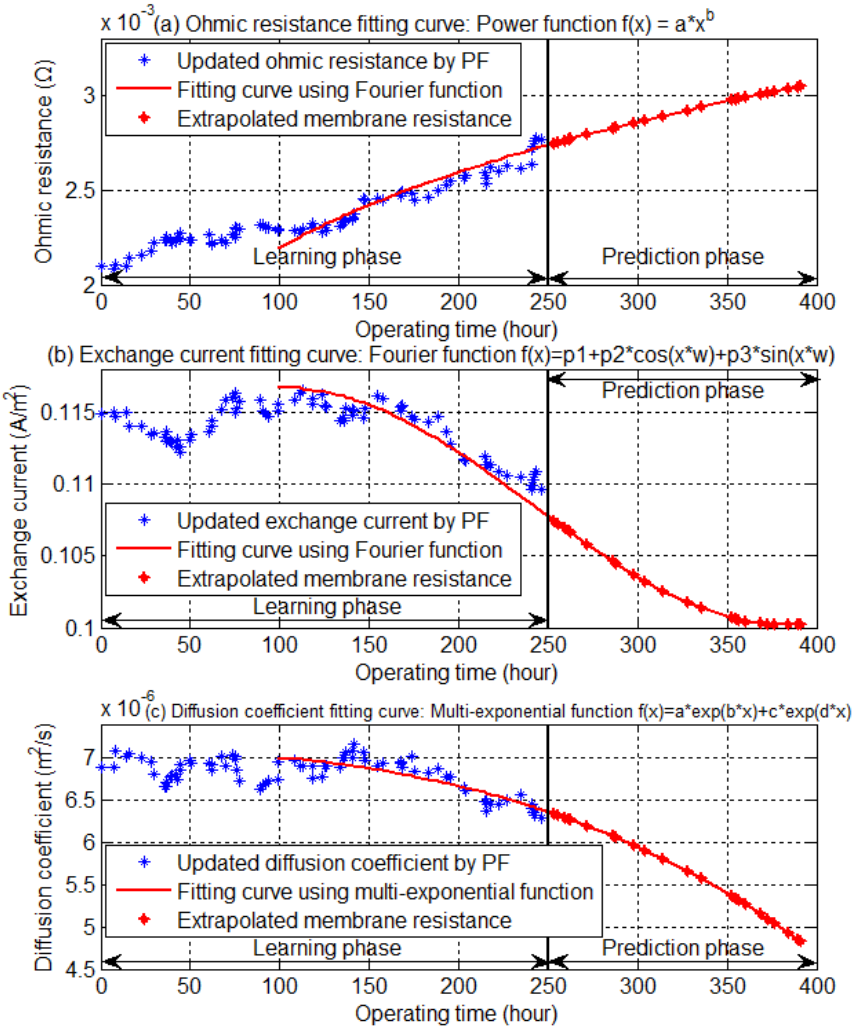

Figure 4.11 Extrapolated result of aging parameters: (a). ohmic resistance. (b). exchange current density. (c). diffusion coefficient. (operating current 30A at 35°C).

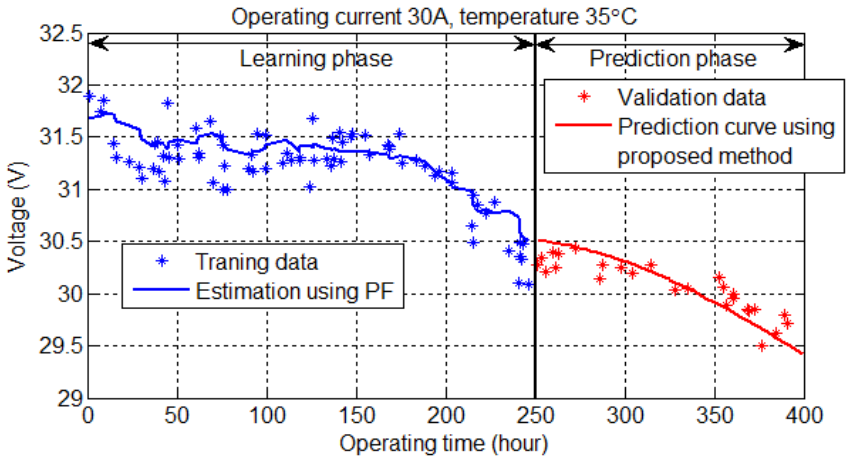

Figure 4.12 Prediction result (current 30A at 35°C, learning time is set to 250 h).

4.2.4.2.3 Third Experiment: PEMFC Operation under 44A at 40°C

In the third experimental aging test, the PEMFC stack runs for 400 hours under a current of 44A at 40°C. By applying the proposed prediction method, the extrapolation results of the aging parameter and voltage degradation prediction result are shown in figure 4.13 and figure 4.14, respectively.

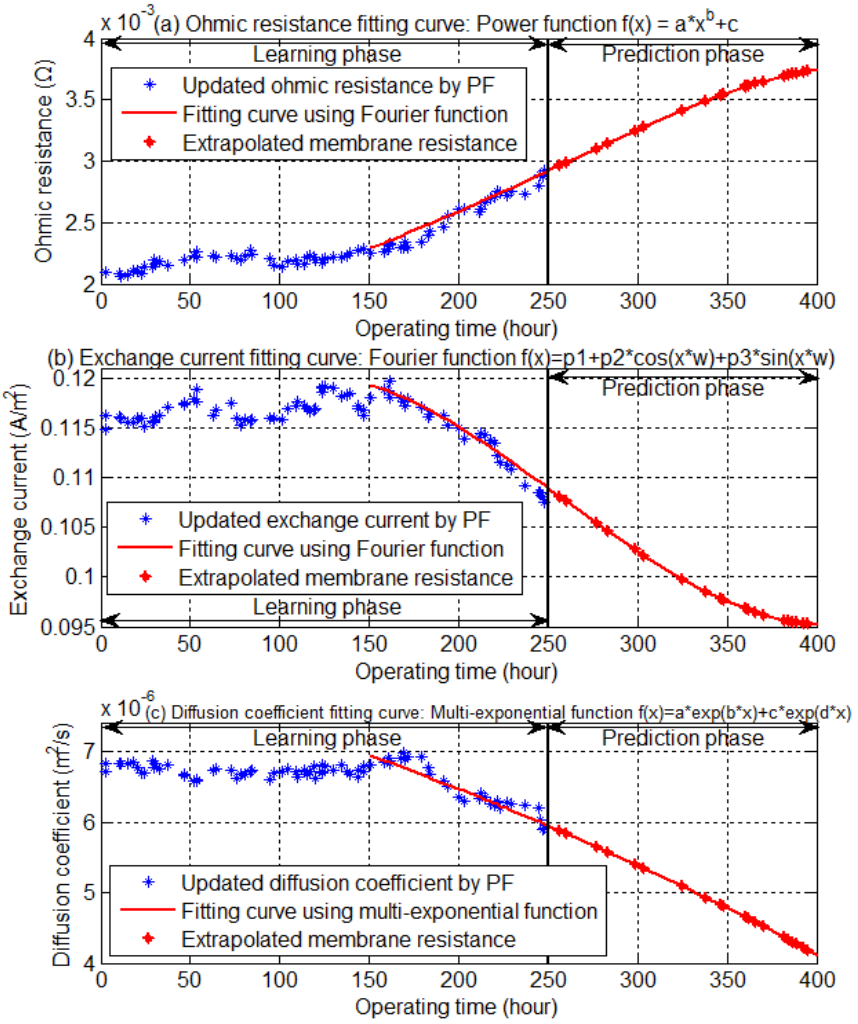

Figure 4.13 Extrapolated result of aging parameters: (a). ohmic resistance. (b). exchange current density. (c). diffusion coefficient. (operating current 44A at 40°C)

The prediction results show that, for the third experimental aging test, the Ohmic resistance increases by more than 76%, the exchange current density and diffusion coefficient decrease by 15% and 40%, respectively. Figure 4.14 clearly shows again that, the prediction curve can describe the trend of the non-linear experimental data set. The RMSE and MAPE of prediction result are 0.3168 and 0.0083, respectively.

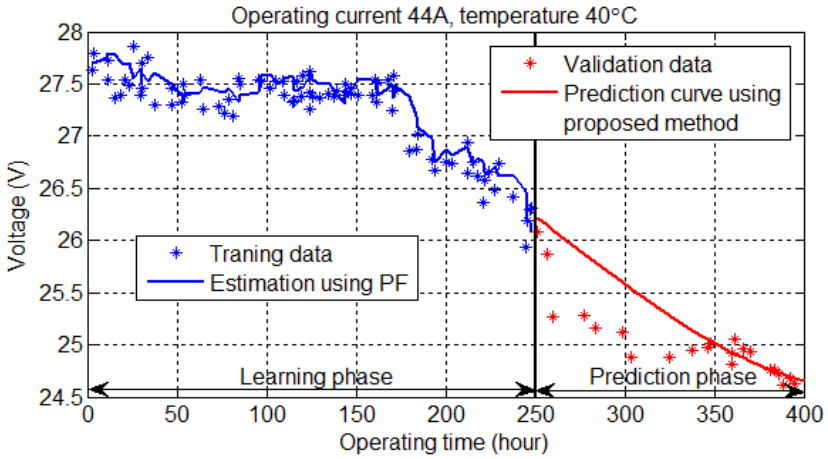

Figure 4.14 Prediction result (current 44A at 40°C, learning time is set to 250 h).

It can be concluded from the above three experimental validations that, when a relatively large amount of data is used by particle filter in the learning phase, with suitable fitting curve functions to extrapolate the values of aging parameters, the proposed prediction method has demonstrated its strong capability on forecasting the future trend of PEMFC degradation voltage under different fuel cell operation conditions.

4.2.4.3 Experimental Validation: Short Learning Time

In order to thoroughly show the effectiveness and advantages of the proposed prediction method, we would like to further investigate the prediction performance of the proposed model with a shorter learning time interval. The learning time t_p is now set to only 150 h (previously 250h). In this case, fewer training points are available to fit the function. By applying the proposed method with this new learning interval, the prediction voltages are shown in the figure 4.15 - 4.17.

The degradation prediction results for the first experimental aging test are shown in the figure 4.15. In this limiting condition, the trend of PEMFC degradation voltage can still be captured, however with a larger prediction error. Figure 4.16 shows the second experimental aging test and it can be seen that, although the proposed prediction method could not show a precise conformity with the validation data after 200 hours, the prediction could still provide accurate and useful prediction results in the near time interval (i.e. between 150h and 200h). For the third experimental aging test, the prediction results are shown in the figure 4.17. Since the training data is very limited, its non-linear degradation trend is not fully learned by particle filter. Thus, the prediction results are not very accurate, especially after 250 hours. Nevertheless, the voltage aging trend can still be roughly described by the predicted results.

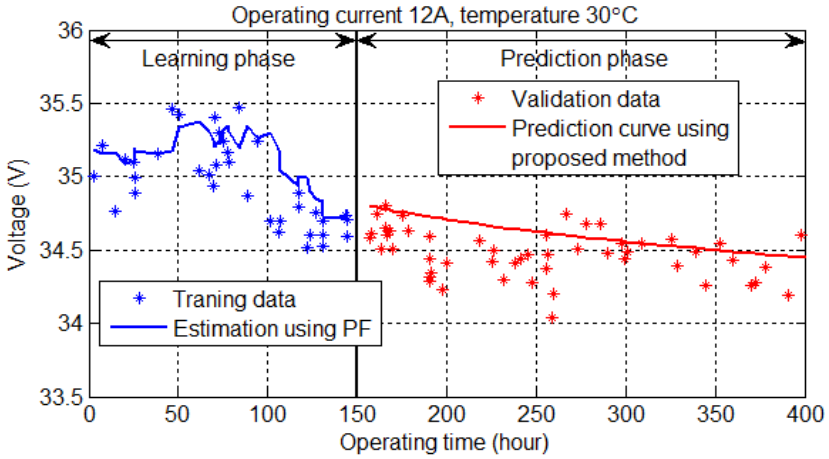

Figure 4.15 Prediction result (current 12A at 30°C, learning time is set to 150 h).

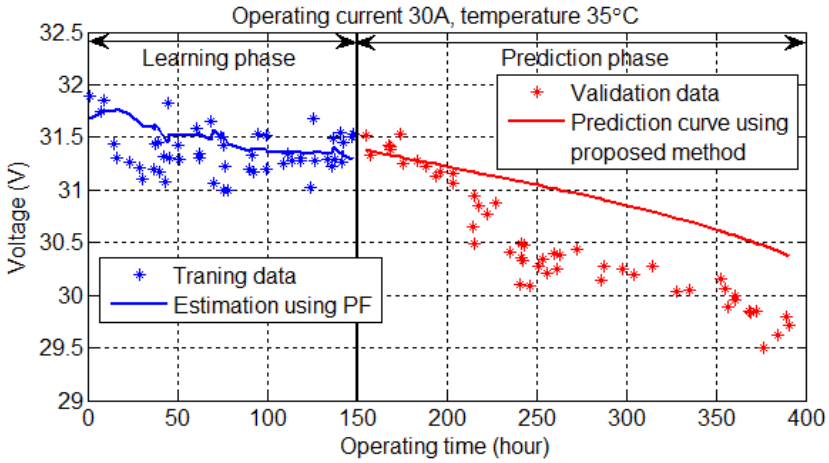

Figure 4.16 Prediction result (current 30A at 35°C, learning time is set to 150 h).

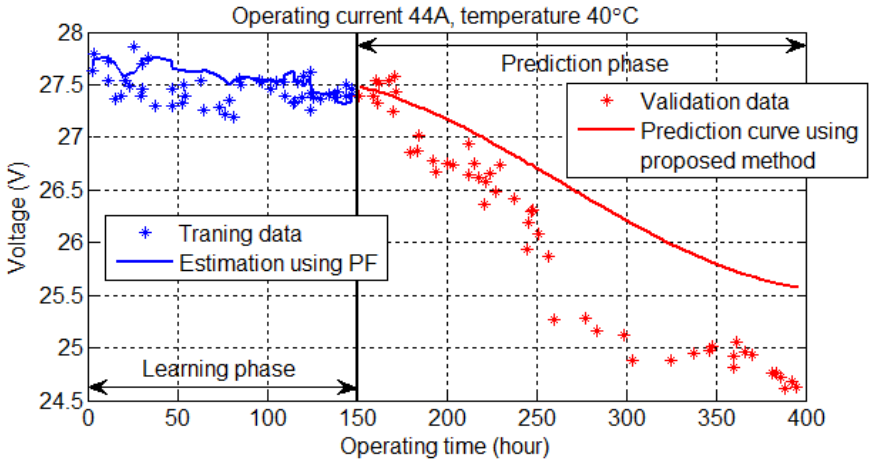

Figure 4.17 Prediction result (current 44A at 40°C, learning time is set to 150 h).

Thus, it can be concluded from the above experimental validation that, although the acquired aging data is extremely restricted, based on the prior known parameter-function pairs, the proposed method has the potential to provide fairly acceptable prediction results, especially at immediate short prediction time range.

It worth also to mentioned that, when the initial training samples are limited, iteration-based prediction strategies [30] are particularly useful to achieve a better performance of the proposed prediction method. The purpose of using an iteration-based prediction strategy is to provide more accurate short-term prediction results and to dynamically update the prediction result with the newest dataset (newly measured data) for iterative data training at next prediction step.

4.2.5 Conclusion

In this section, a novel approach for PEMFC output voltage prediction based on a multi-physical aging model with particle filter and data extrapolation approach was proposed (please refer to previous work [13] [14]). The proposed multi-physical aging model fully considers the three most important aging phenomena during PEMFC operation: ohmic losses, reaction activity losses, and reactants mass transfer losses.

The proposed prediction method is divided into two stages: learning phase and prediction phase. During the learning phase, the particle filter is applied to study the non-linear aging behavior and update the proposed aging parameters. Then, different fitting curve functions are used to represent the trend of aging parameters in the learning phase, and further extrapolate the future values of aging parameters in the prediction phase. At last, by using the extrapolated aging parameters, the proposed aging model predicts fuel cell voltages in the prediction phase.

The experimental validations show that, in order to fully and accurately represent the non-linear trends of aging parameters and further achieve a better performance of proposed prediction method, a relatively large amount of data should be learned by particle filter in the learning phase, and suitable fitting curve functions should be used to extrapolate the values of aging parameters in the prediction phase. It is also important to note that, even when the acquired training data is extremely limited, by knowing a prior the parameter-function pairs, the proposed method is still able to provide acceptable results, especially at immediate short prediction time range.

4.3 Degradation Prediction Using a Moving Window Based Hybrid Prognostic Approach

The above physical-based prediction method cannot be used in the on-line prognostic applications, since this single-step prognostic method makes prediction for a fixed horizon. In order to improve the proposed method, an innovative robust prediction algorithm for PEMFC performance degradation is proposed based on a combination of model-based and data-driven prognostic method. In the proposed hybrid method, a novel approach using the moving window method is applied, in order to 1) train the developed models; 2) update the weight factors of each method and 3) further fuse the predicted results iteratively. In the proposed approach, both model-based and data-driven methods are simultaneously used to achieve a better accuracy.

In order to verify the proposed method, three experimental validations with different aging testing profiles have been performed. The results demonstrate that the proposed hybrid prognostic approach can achieve a higher accuracy than conventional prediction methods. In addition, in order to find the satisfactory trade-off between the prediction accuracy and forecast time for optimizing on-line prognostic (for example the dynamic operating conditions in fuel cell hybrid electric vehicles), the performance variation of proposed approach with different moving window length is further shown and discussed.

In this section, a model-based fuel cell voltage degradation prediction model using empirical equation and particle filter approach, and a data-driven prediction model using NARNN are presented, respectively. Then, a hybrid prognostic approach is further given based on combining the fusion approach and moving window techniques.

4.3.1 Model-Based Prediction Method

A model-based approach has been chosen as the first prediction method in this thesis. In this section, an empirical fuel cell voltage degradation model is presented at first. In order to estimate the state variables in the model, a particle filter based identification algorithm is applied. The corresponding prognostic method is presented and discussed at last.

Based on regression analysis of experimental degradation data, it has been found that an empirical equation form can well describe the fuel cell voltage degradation process [26]-[28]:

$$V_{cell}(t) = a(t) \cdot exp(b(t) \cdot t) + c(t) \cdot exp(d(t) \cdot t) \tag{4.25}$$

where $V_{cell}(t)$ is the fuel cell output voltage at time t, the coefficients a and b are related to the fuel cell internal impedance, the coefficients c and d are related to the fuel cell aging rate. The discrete-time state space of this voltage degradation model is depicted as follows:

$$\begin{cases} x(k) = x(k-1) + Q_{k-1} \\ y(k) = a(k) \cdot exp(b(k) \cdot k) + c(k) \cdot exp(d(k) \cdot k) \end{cases} \tag{4.26}$$

where k is the sampling step, the state variables need to be estimated can be described by $x(k) = [a(k), b(k), c(k), d(k)]^T$, the observed variable $y(k)$ represents the fuel cell voltage, and Q_k is the system stochastic normal distributed noises.

The equation 4.26 is clearly in a non-linear form. In order to accurately estimate the state variable $x(k)$, the particle filter approach is used, since it can effectively solve the Bayesian estimation problem of non-linear system based on the Monte Carlo sequence. The purpose of using particle filter for non-linear model parameter identification is to capture the trend of fuel cell degradation voltage during the training phase, and further correctly represent the captured aging trend in the future (prediction phase).

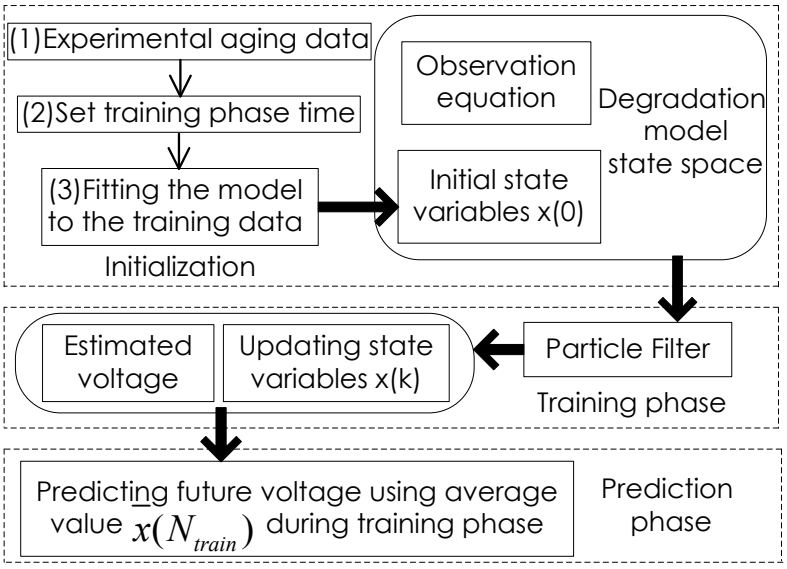

Figure 4.18 Schematic diagram of model-based diagnostic approach.

Based on the presented degradation model state space representation equation 4.26, the detailed flow diagram of model-based prognostic methodology is shown in figure 4.18. It can be seen from the figure 4.18 that, the development and validation of this model-based prognostic method includes three parts: initialization, training phase and prediction phase.

4.3.1.1 Initialization of Model-Based Approach

The detailed steps of initialization for model-based diagnostic approach are described as follows:

1) The degradation data and corresponding experimental conditions are presented at first. A PEMFC stack (commercial Ballard NEXA 1.2 kW PEM fuel cell stack) is used in a 400 hours experimental degradation test. It can be seen from the figure 4.19 that, during the 400 hours degradation testing (operating condition: current 35A at temperature 40°C), the fuel cell degradation voltage data is measured and recorded every 10 minutes. It should be noted that, before applying the proposed algorithm to the PEMFC stacks aging dataset, a data post-processing is performed to eliminate the unreliable measurement data points. Thus, the available degradation data consists of 91 data points (by down-sampling the original measured data), which can be seen in the figure 4.19.

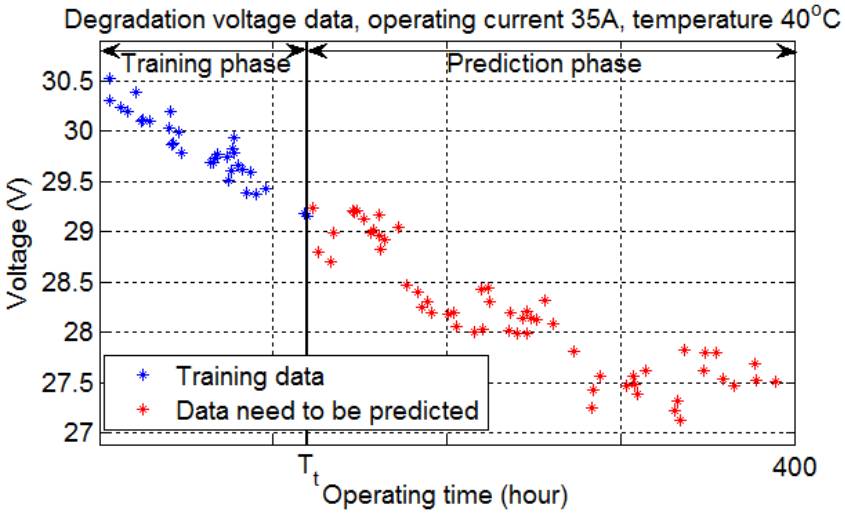

Figure 4.19 Fuel cell stack experimental aging voltage under current 36A at 35 °C.

2) Then, the training time point is set to T_t and thus the prediction phase is $400 - T_t$ long. It means that, 0 h to T_t h, the state variable is trained and updated using particle filter, the remaining degradation data from T_t to 400 hours is use to evaluate the prediction results.

3) The initialization of state variables $x(k)$ is performed by fitting the experimental degradation data into the initial model.

4.3.1.2 Training Phase of Model-Based Approach

In the training phase, the purpose of particle filter is to estimate recursively the state variable $x(k)$ based on the initialization model and experimental aging data in the training phase. It should be noted that, during the particle filter based estimating process, the variance selection of process noise Q_k need to be chosen carefully. A large variance of Q_k ensures a more extensive sampling distribution, since it provides sample particles with a great diversity. On the other hand, a smaller variance of Q_k allows a sufficiently fast convergence. There already exists the observation noise in the experimental aging data, since the fuel cell degradation voltage data are measured directly by sensors.

From the known proposal distribution, the particle filter uses a set of random sample particles based on the Monte Carlo sequence, in order to estimate the posterior probability density of non-linear system. More detailed content about particle filter can be found in the previous section.

4.3.1.3 Prediction Phase of Model-Based Approach

In the previous training phase, the particle filter estimates and updates the state variables $x(k)$ at every sampling step. Thus, the voltage degradation behaviors of training phase have been fully captured. As mentioned before, in order to well represent the captured aging behavior in the prediction phase, all of the trained state variables $x(k)$ during the training phase should be taken into account in the empirical model equation 4.25. In this case, the most efficient way of integrating all the state variables $x(k)$ is to use their average value during the training phase (from 0 to T_t hour). The average value of state prediction results is expressed as:

$$\bar{x}_{0-T_t} = \frac{\sum_{k=0}^{T_t} \hat{x}_k}{N_{train}} \tag{4.27}$$

where N_{train} is the number of degradation data (blue points), which are used for particle filter learning during the training phase, as shown in the figure 4.19.

Thus, the prediction voltage results in the prediction phase $\hat{y}_k$ are calculated by the output equation of state space equation 4.25:

$$\hat{y}_k = \bar{a}_{0-T_t} \cdot exp\left(\bar{b}_{0-T_t} \cdot k\right) + \bar{c}_{0-T_t} \cdot \exp\left(\bar{d}_{0-T_t} \cdot k\right) \tag{4.28}$$

where the sample step $k = T_t + 1, T_t + 2, T_t + 3, \ldots 400$.

4.3.2 Data-Driven Prognostic Method

The proposed model-based prognostic method is essentially based on an exponential regression model, it cannot accurately catch the non–linear and uncertain behaviors during the aging process. Compared with model-based prognostic method, the data-driven approach can well describe the local non-linear characteristics of degradation voltage. Especially for the short-range and medium-range prediction time, the data-driven prognostic method can give a better representation of uncertainties in the degradation process. In this thesis, a data-driven prognostic method has been chosen as the second prediction method.

As a data-driven approach, the artificial neural networks can be effectively used to implicitly indicate the complex non-linear characterization between system inputs and outputs. The aging process of PEMFC can be considered as a non-linear autoregressive time series model. The actual fuel cell voltage (model output) can be considered as a variable determined by an unknown non-linear process from the previous voltage values. In this case, the non-linear autoregressive neural network (NARNN) model can then be used to track the non-linear characteristics of PEMFC degradation.

In this section, a NARNN model for fuel cell degradation is presented at first. An optimal training strategy is also proposed in order to achieve good prediction performance of the developed NARNN model.

4.3.2.1 Non-linear Autoregressive Neural Network Model

A NARNN model is suitable to describe the non-linear dynamic in a wide variety of system and have been extensively implemented in various applications [31]-[33]. The general formulation of NARNN model can be expressed as follow:

$$y_t = F(y_{t-1}, y_{t-2}, \dots y_{t-m}, u_t, u_{t-1}, u_{t-2}, \dots u_{t-n}) \tag{4.29}$$

where u_t and y_t are the prediction model inputs and outputs at time t respectively, m and n are the respective delay factors, F is the NARNN function describes the non-linear correlation between the u_t and y_t. For the fuel cell diagnostic purpose, the detailed NARNN layer diagram is shown in the figure 4.20.

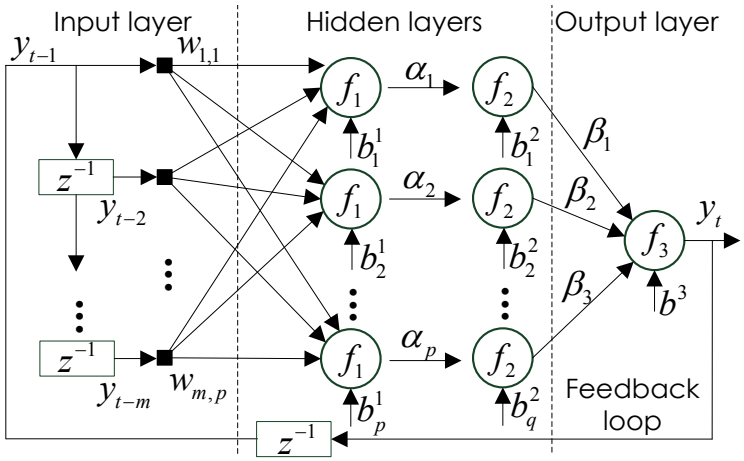

Figure 4.20 Structure of the NARNN model for PEMFC aging prediction.

As shown in the figure 4.20, the vector of the input layer at time t is $U_t = [y_{t-1}, y_{t-2}, \dots y_{t-m}]^T$, and the output of model y_t stands for the PEMFC voltage value at time t, p is the number of neurons in the first hidden layer, q is the number of neurons in the second hidden layer. The activation functions of neurons in the first hidden layer are log-sigmoid transfer functions, the function in the second hidden layer is the tan-sigmoid transfer function, and the function in the output layer is the linear transfer function. Thus the output of the proposed NARNN model can be written as follow:

$$y(t) = purelin(w^3 tansig(w^2 logsig(w^1 U_t + b^1) + b^2) + b^3) \tag{4.30}$$

where w and b respectively stand for the vector of weights and bias for each layer, the output of NARNN model $y(t)$ is the PEMFC voltage prediction result, the model input U_t is the PEMFC voltage in the previous time from $t-1$ to $t-m$. Thus, the future degradation behaviors of PEMFC $y(t)$ are expressed in the above non-linear autoregressive form.

4.3.2.2 Data-Driven Prognostic Method Implementation

The detailed flow diagram of data-driven prognostic methodology using the presented NARNN prediction model is shown in figure 4.21. Similar to the previous model-based prognostic method, the proposed data-driven prognostic method also includes two parts: training phase and prediction phase.

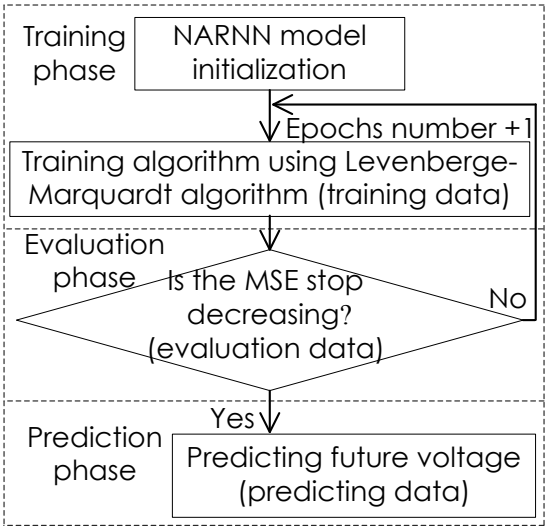

Figure 4.21 Schematic diagram of data-driven prediction using NARNN model.

For the training phase, the initialization of NARNN model includes setting the number of neurons, transfer functions selection, initialization of weights and deviations in each hidden layer, etc. In terms of the system identification algorithm, the Levenberge-Marquardt optimization method is adopted. Compared with the common back propagation first-order method, this training method provides a more rapid quadratic rate of convergence. More detailed content about Levenberge-Marquardt method can be found in [34].

It should be noted that, different from the previous particle filter training, the neural networks are sensitive to data over-fitting. To overcome this problem in practice, the aging data of training phase are further divided into training part and evaluation (validation) part. The training data are used to identify the NARNN model parameters, and the evaluation data are used to evaluate network generalization fitting ability (accuracy on the validation data). There is usually a trade-off between accuracy for training part and generalization fitting ability for prediction part [35]. In our proposed method, the training process is terminated when the mean squared error (MSE) of validation part stopped decreasing, as shown in the figure 4.21.

4.3.3 Hybrid Prognostic Approaches

As an integration process of multiple prognostic results from different methods, a suitable fusion approach is critical to demonstrate their advantages [36]-[42]. It increases the process reliability and robustness by combining the complementary information from different prognostic methods in intelligent ways. Therefore, a hybrid prognostic

approach can be expected to provide more accurate and robust prediction results compared with single model based method.

In order to combine the advantages of different prediction methods in the proposed hybrid prognostic approach, a good understanding about the specific characteristics of each prediction method is important. The model-based method can effectively forecast the aging trend for a long-range prediction time, however it cannot accurately describe the local non-linear characteristics of aging. In contrast, the data-driven method can provide a good non-linear representation of uncertainties in the degradation process for the short-range and medium-range prediction time. But its long-term prediction result is not accurate due to predicted data fluctuation. Therefore, in order to effectively taking the advantages of each method into account, there are two critical issues that need to be considered when using a hybrid prognostic approach: 1) the range selection of training and prediction time, and 2) weight factors determination of each corresponding method.

As an efficient computational strategy, the moving window method is considered to be a good solution for the above-mentioned issues. In this section, a moving window method is presented firstly in order to take different prediction time range into account. A weight factors adjustment method is then proposed using the results from the moving window method. The proposed method can dynamically adjust the weights vector at each step of the moving window.

4.3.3.1 Moving Window Method

The primary purpose of using a moving window method is to update and add the newest dataset for iterative data training, and provide dynamic weight factors to further improve the prediction accuracy. In order to perform iterative training during the forecasting process, the model input dataset are updated continuously by moving window approach, as shown in the figure 4.22.

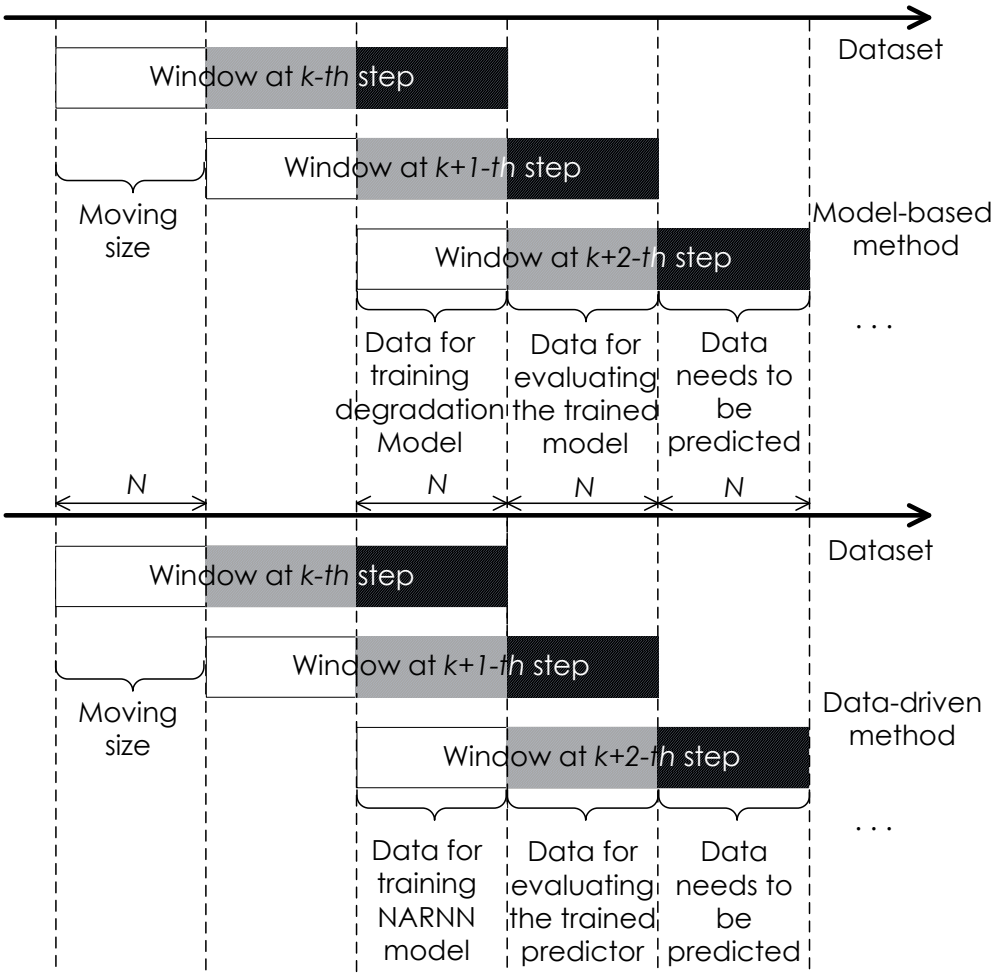

Figure 4.22 Schematic diagram of moving window method in the proposed hybrid prognostic approach.

In the figure 4.22, the length of each window includes three parts: training part (white region, measured data in the past), evaluation part (gray shadow region, measured data in the past) and predicting part (black shadow region, prediction data for the future). At each prediction step, the data in the white region are used to train the previously developed models. The data in the gray shadow region are then used to evaluate the newly updated model fitting ability, and the data in the black shadow region are the future data points that need to be predicted from the models.

Take the first model-based method as an example. It is assumed that the data number in training part, evaluation part and predicting part are equally defined as N, the moving size between each prediction step is also set to N. At the k-th prediction step, the N measured training data located at the beginning of moving window (from 1 to N) are applied to train the k-th model, the measured data from $N+1$ to $2N$ are then used to evaluate the model prediction accuracy, and the predicted data are given from $2N+1$

to $3N$. When the prediction is iterating from *k* to *k*+1 step, the previously measured aging data from $N+1$ to $2N$ are applied to train the *k+1*-th model, the newly measured data between two prediction step from $2N+1$ to $3N$ are used to evaluate the new model accuracy, and the predicted data are given this time from $3N+1$ to $4N$. The data-driven method has the similar iteration procedures.

Therefore, this moving window method is an efficient strategy to dynamically retrain the models during the forecasting process with new data inputs. In addition, by iteratively evaluating the fitting ability of each method at each prediction step, the corresponding weight factor can also be adjusted dynamically. Moreover, by using the proposed moving window method, the forecast time can be easily changed by using different values of N.

4.3.3.2 Weight Factors Calculation

As mentioned before, the data of gray shadow region are used to evaluate the model fitting ability (estimation of accuracy at actual prediction step). During the evaluation process (gray shadow region), the measured fuel cell voltage data are compared with both model outputs to generate individual residuals. The generated residuals are then used to calculate the weight coefficient of future prediction value obtained from each method. This weight factor, noted as $w_{p,k}$, represents the modeling accuracy of each method at actual prediction step, which is inversely proportional to the residual as expressed in the following equation:

$$w_{p,k} = \frac{1}{\sum_{i=1}^{N} \sqrt{\left(y_{eva,p,k}(i) - \hat{y}_{eva,p,k}(i)\right)^2}} \tag{4.31}$$

where $p = 1$ stands for the first model-method and $p = 2$ stands for the second data-driven method. k is the actual prediction step, $y_{eva,p,k}$ is the measured fuel cell voltage values used for evaluation, $\hat{y}_{eva,p,k}$ is the model predicted fuel cell voltage values in the evaluation part. At each prediction step, this weight factor is dynamically adjusted.

By assuming that both prediction processes (model-based and data-driven) are conditionally independent at each prediction step, the overall prediction results $y_{fus,k}$ can be described using weighted average as:

$$y_{fus,k} = \sum_{p=1}^{P} y_{pre,p,k} \cdot w_{norm,p,k} \tag{4.32}$$

where $P = 2$ representing the total number of methods, $y_{pre,p,k}$ is the predicting data, $w_{norm,p,k}$ is the normalized weight factor, which can be calculated by:

$$w_{norm,p,k} = \frac{w_{p,k}}{\sum_{p=1}^{P} w_{p,k}} \tag{4.33}$$

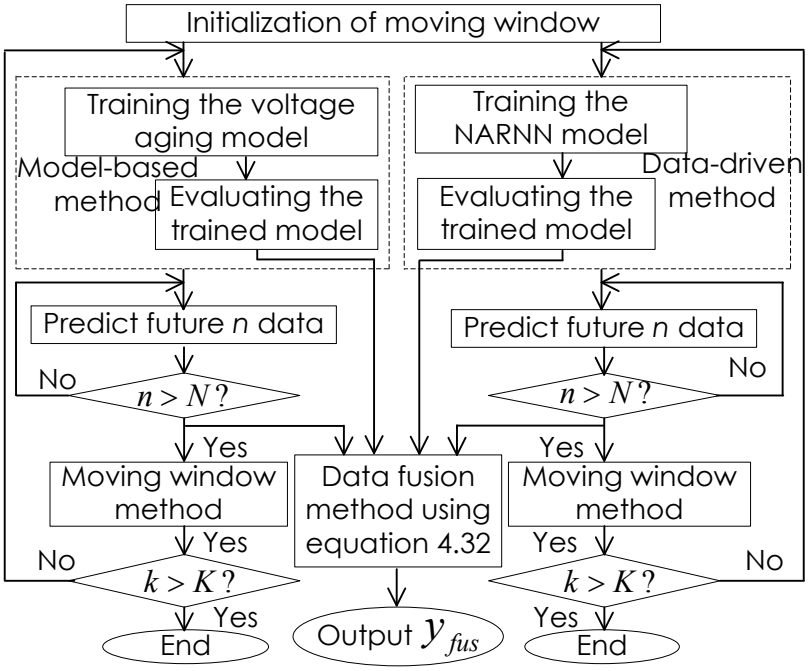

Figure 4.23 Flowchart of the proposed overall prediction algorithm method for fuel cell output voltage degradation prediction.

The proposed overall prognostic algorithm can then be illustrated in figure 4.23. In figure 4.23, N is the moving window coefficient, n is the number of predicted data, k is the actual prediction step, the total prediction step K (the threshold step in a specified length of voltage data) determines the retraining cycle time.

4.3.4 Experimental Results and Discussion

In order to experimentally validate the accuracy and robustness of the proposed hybrid prognostic method, experimental degradation datasets from three different types of fuel cell stacks are presented respectively in this section:

First case study: Ballard NEXA 1.2 kW commercial PEM fuel cell stack 400 hours aging test under the working conditions of current 35A at temperature 40°C;

Second case study: PM 200 8.0 kW fuel cell stack 10000 hours aging test working under stationary prime power application;

Third case study: 600 W stationary PEM fuel cell stack 1200 hours aging test under static current load.

4.3.4.1 First Case Study: Comparison of the Proposed Hybrid Model and Single Model Methods

In the first case, a Ballard NEXA 1.2 kW commercial PEM fuel cell stack runs for 400 hours aging test under the working conditions of current 35A at temperature 40°C (the aging dataset is presented in figure 4.19). This experiment aims to clearly show the accuracy and robustness of the proposed hybrid method. The detailed operation conditions of NEXA fuel cell stack are listed in table 4.2.

Table 4.2 Operation conditions of the first case study: Ballard NEXA fuel cell stack

	First case study
Stack type	Ballard NEXA 1.2kW
Number of cells	47
Operation mode	Dead–end mode
Air supply	Air blower + filter
Cooling	Air fan cooled
Operating hours	400h
Air stoichiometry	2.0
Stack temperature	40°C
Stack current density	$0.24\mathrm{A/cm^2}$

By applying only the model-based method, with a moving window coefficient N of 15, the prediction results and identified parameters are illustrated in figure 4.24.

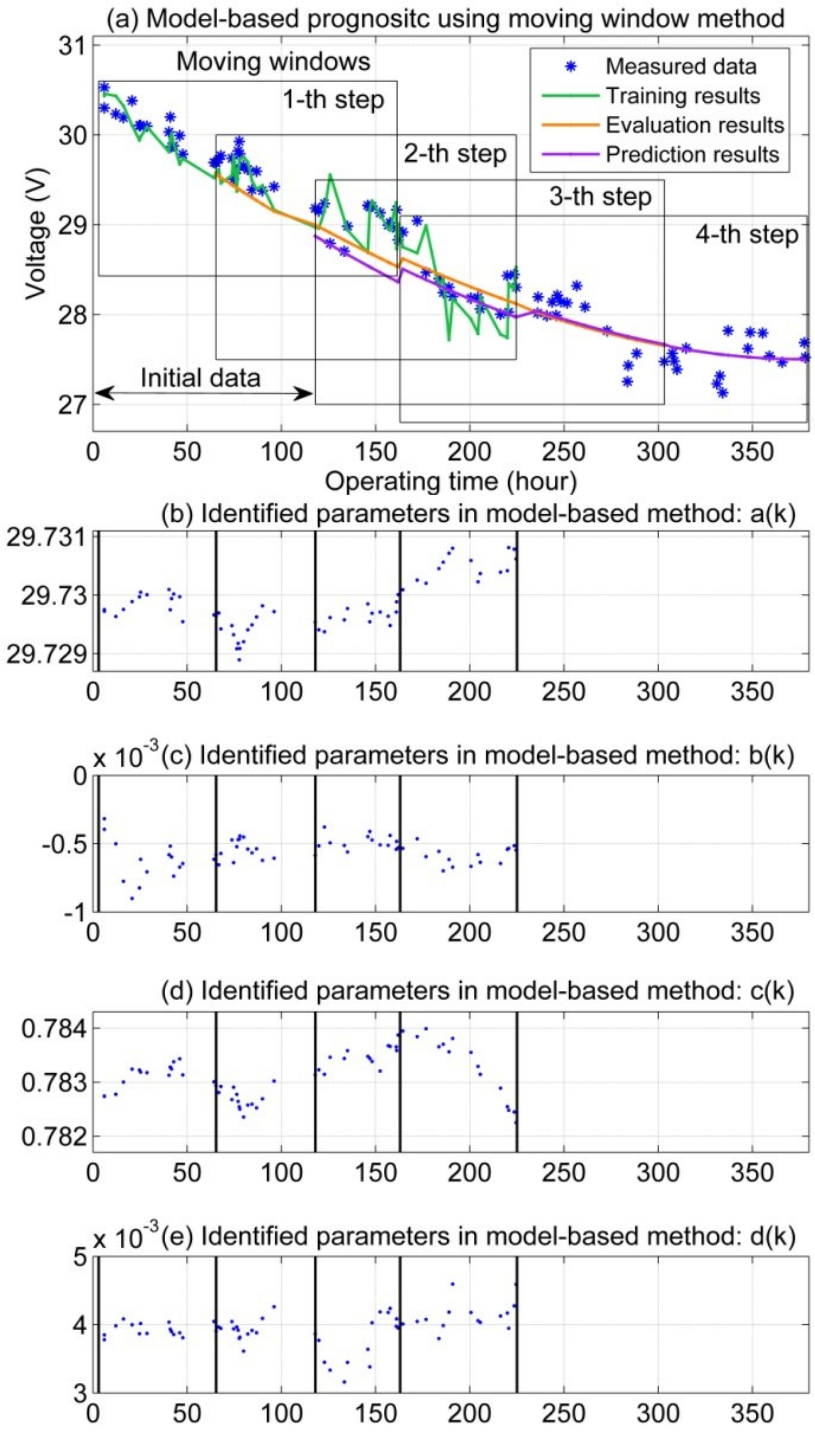

Figure 4.24 Prediction results and identified parameters of model-based prediction method.

As shown in the figure 4.24 (a), the initial known 30 data are used to train and evaluate the model for the *1-st* step of prediction. It can be seen clearly from the figure that, the fade trend of red prediction curve is in well agreement with the measured degradation data. It should be noted that, since the model is retrained at each step when data

training window move forward, it is natural that the new forecast trend of the new step is slightly different from the previous one. For each prediction step, the blue points in each data window indicate training data, which is used to identify four model parameters $a(k), b(k), c(k), d(k)$ in equation 4.25. The green curve stands for the obtained training results. Then the trained model generates the yellow curve, which is compared with the corresponding measured data to evaluate the accuracy of the trained model. The purple curve is the combination of prediction results at each step (moving window) from trained model.

Figure 4.24 (b)-(e) shows the identified model parameters at each prediction step, it can be seen that during forecasting process, the degradation model is dynamically retrained and the particle filter iteratively update the model parameters. As mentioned in section 4.3.1.3, the average value of each identified parameter at each step is further used to predict the model output in the prediction part, as shown in equation 4.28. These average values of model parameters $\bar{a}(k), \bar{b}(k), \bar{c}(k), \bar{d}(k)$ are given in the table 4.3.

Table 4.3 Average values of identified parameters used in the prediction part at each step (model-based)

	$\bar{a}(k)$	$\bar{b}(k)$	$\bar{c}(k)$	$\bar{d}(k)$
1-th	29.7299	-6.2637e-04	0.7831	3.9282e-03
2-th	29.7294	-4.4274e-04	0.7827	3.9289e-03
3-th	29.7297	-4.9277e-04	0.7835	3.7804e-03
4-th	29.7305	-4.8636e-04	0.7833	4.1389e-03

By applying only the data-driven prognostic method with the same moving window coefficient, the prediction results from data-driven method are illustrated in figure 4.25.

It can be seen clearly from the figure 4.25 that, compared with previous results from model-based method, the data-driven method has more advantages on describing the non-linear features of the degraded voltage during forecasting process (i.e. the results of NARNN model are fluctuated more dynamically with the measured voltage values). For each prediction step, the blue points in each data window indicate the training data, which is used to identify the model parameters. Then the trained model generates the gray curve, which is compared with the corresponding measured data to evaluate the accuracy of the trained model. The red curve is the combination of prediction results at

each step (moving window) from trained model. The identified NARNN model is shown in figure 4.26.

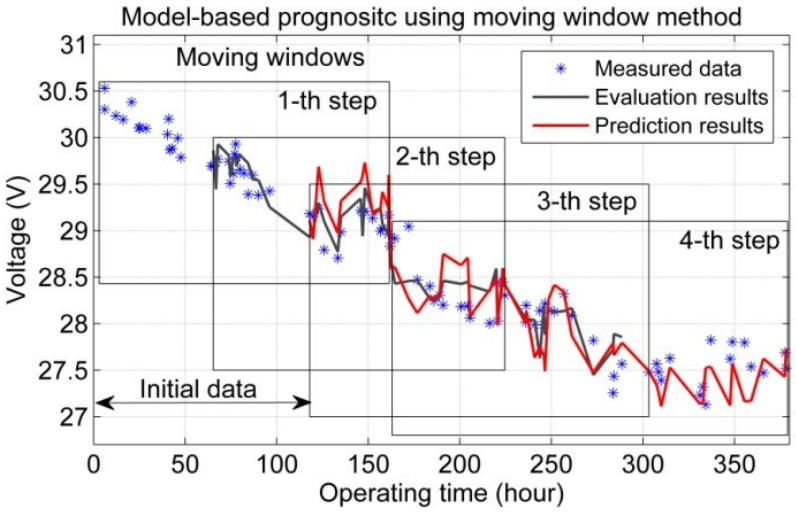

Figure 4.25 Prediction results of data-driven prediction method.

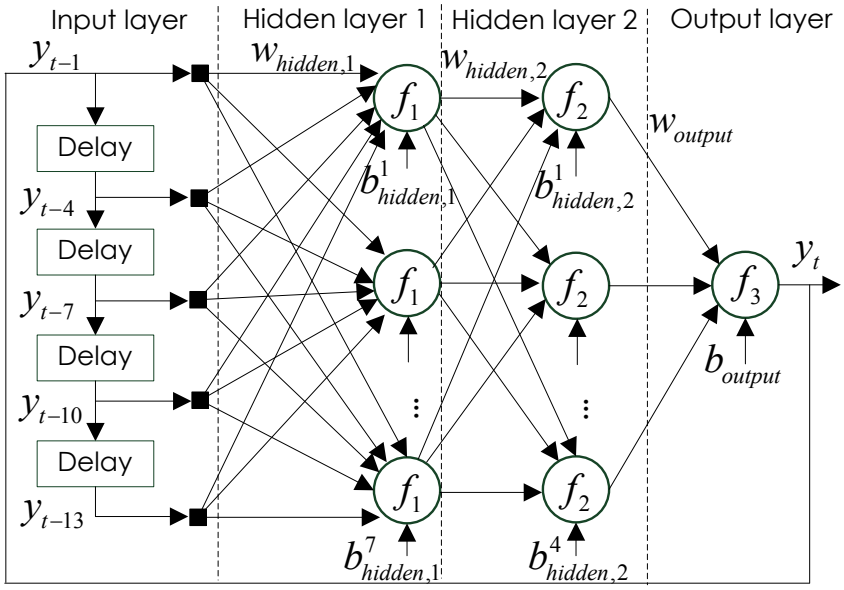

Figure 4.26 Identified NARNN model for data-driven method.

As shown in the figure 4.26, this NARNN model has two hidden layers, and its parameters consist of delay coefficients, the weight coefficients array of each layer $w_{hidden,1}$, $w_{hidden,2}$, w_{output}, the bias coefficients vector of each layer $b_{hidden,1}$, $b_{hidden,2}$, b_{output}. As shown in figure 4.26, the input layer is $U_t = [y_{t-1}, y_{t-4}, y_{t-7}, y_{t-10}, y_{t-13}]^T$, the first hidden layer has seven neurons, thus the output of the first hidden layer α is a 7×1 vector, which can be expressed as the following equation:

$$\alpha = logsig(w_{hidden,1} \cdot [y_{t-1}, y_{t-2}, \dots y_{t-m}]^T + b_{hidden,1}) \tag{4.34}$$

where the weight coefficients $w_{hidden,1}$ is a 7×5 array, the bias coefficients $b_{hidden,1}$ is a 7×1 vector. The second hidden layer has four neurons, thus the output of the second hidden layer is a 4×1 vector, which can be expressed as follow:

$$\beta = tansig(w_{hidden,1} \cdot \alpha + b_{hidden,2}) \tag{4.35}$$

where the weight coefficients $w_{hidden,2}$ is a 4×7 array, the bias coefficients $b_{hidden,2}$ is a 4×1 vector. The output of the NARNN y_t is:

$$y_t = purelin(w_{output} \cdot \beta + b_{output}) \tag{4.36}$$

where the weight coefficients $w_{hidden,2}$ is a 1×4 array, the bias coefficients b_{output} is a 1×1 vector.

Similar to the previous model-based prediction method, for each prediction step, the NARNN model is dynamically retrained and all the weight coefficients array and bias coefficients vector are iteratively updated. By applying now the proposed hybrid prognostic method, the comparison of prediction results is shown in figure 4.27.

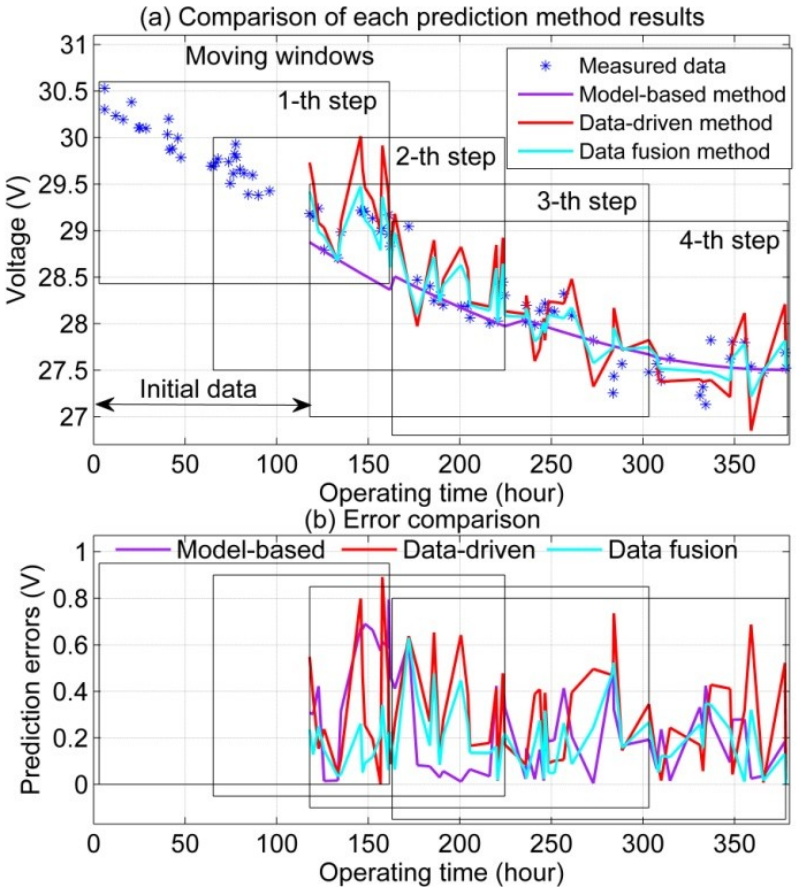

Figure 4.27 Comparisons of three prediction method results.

It can be seen from the figure 4.27 that, by adjusting the weight factors at each prediction step, the proposed hybrid prognostic method can simultaneously and accurately capture the long-term fuel cell voltage degradation trend, as well as the non-linear voltage variation characteristics. Comparison results show that the proposed hybrid prognostic method has stronger capability on maintaining high prediction accuracy. The accumulated prediction errors for the entire forecasting range (0 to 400 hours), such as Root Mean Square Error (RMSE) and maximum prediction error (MAE) are shown in table 4.4. It can be seen again that the proposed hybrid prognostic method can achieve better accuracy (prediction error is at least 30% lower) than both single prediction method.

Table 4.4 RMSE of Prediction Results

	Model-based method	Data-driven method	Hybrid prognostic method
RMSE	0.3362	0.3665	0.2352
MAE (V)	0.7949	0.8915	0.6302

4.3.4.2 Second Case Study: Performance Evaluation with Different Moving Window Length

In this second case, an 8 kW PM 200 PEMFC stack (96 cells) is operated for 10000 hours aging test. The operation conditions of PM 200 fuel cell stack are listed in table 4.5.

Table 4.5 Operation conditions of the second case study: PM 200 fuel cell stack

	Second case study
Stack type	PM 200 8.0kW
Number of cells	96
Operation mode	Recirculation mode
Air supply	Air blower + filter
Cooling	DI–Water / Glycol
Operating hours	10000h
Air stoichiometry	1.7
Stack temperature	58℃
Stack current density	$0.64 A/cm^2$

In this study, the total available aging data contains around 6500 data points, which are measured and post-processed under operation condition with a current density of $0.64A/cm^2$ and a temperature of 58℃. This experiment aims to analyse the influence of different moving window coefficient (length) on the performance of proposed algorithm for the long-term degradation prediction. By applying the proposed hybrid prognostic method, the coefficient of moving windows N is respectively set to 100, 200, 300, 500 and 700. The obtained prediction results are shown in the following figure 4. 28.

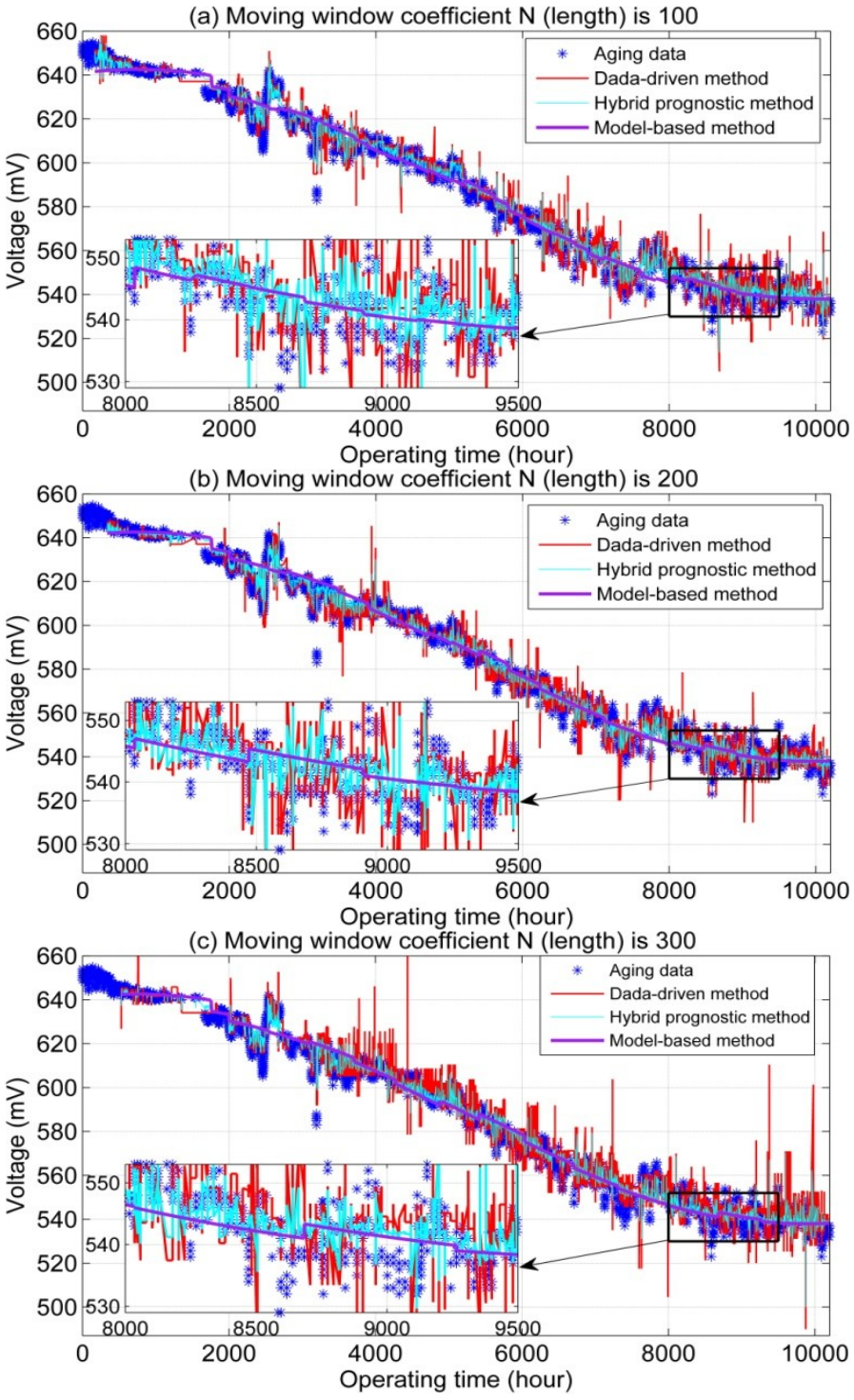

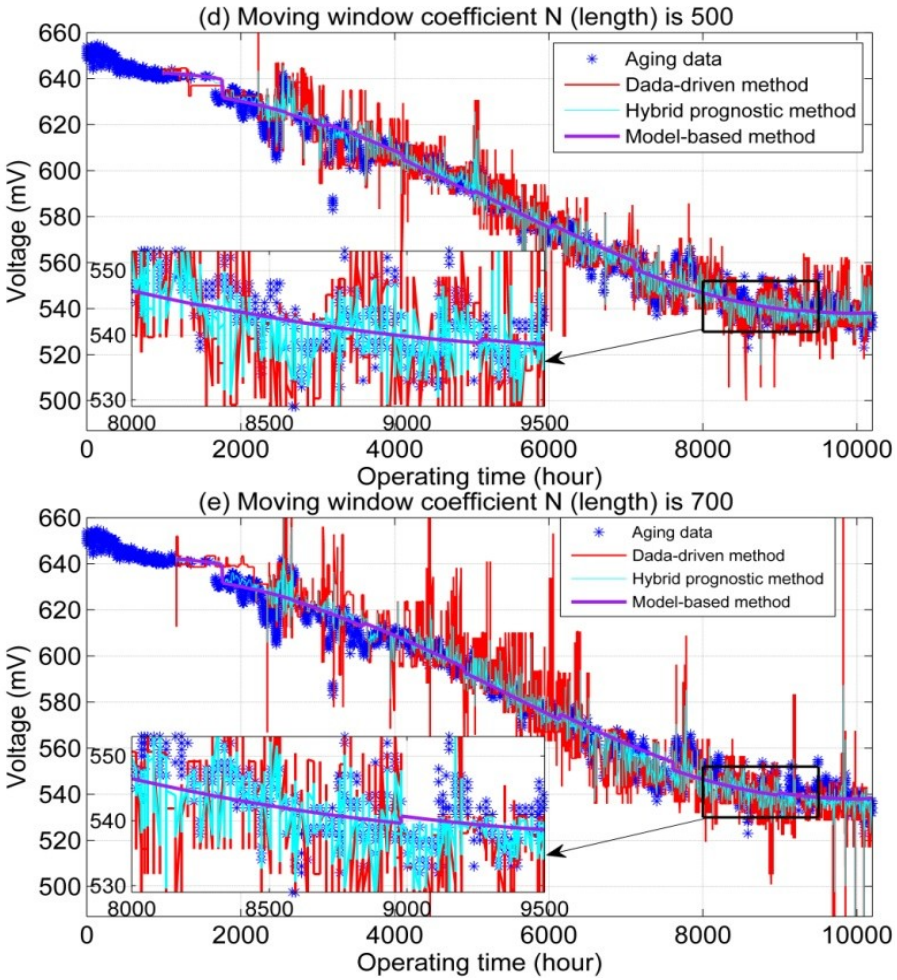

Figure 4.28 Prediction results of proposed hybrid prognostic method using different moving window coefficient N (length).

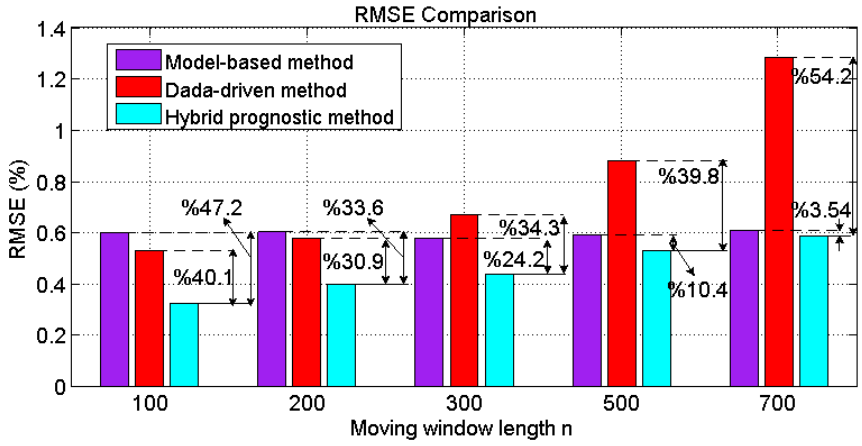

Figure 4.29 The accuracy improvement with different moving window coefficient N.

It should be noted that, the time interval between 2 data points is around 1.5 hours in this test case. Thus, a moving window coefficient N 100 to 700 corresponds to a forecast time of 150 to 1050 hours respectively. It can be concluded from the figure 4.29 that, by

using the proposed hybrid prognostic method, the accuracy improvement decreases when the forecast time length increases. This is mainly because the errors of data-driven method increase significantly with the forecast time. In contrast, it can be seen that the errors of model-based method are not visibly affected by the forecast time.

Thus, in order to maintain simultaneously high precision and relatively long forecast time for on-line prognostic applications, a compromise between prediction accuracy and forecasting time length should be appropriately defined based on the specific application requirement. From a decision making point of view, the prognostic of fuel cell system must be performed with a long enough forecasting time to allow reaction. For a stationary fuel cell application [12], around 160 hours long prediction (one week) is considered appropriate. It should be noted that, the proposed hybrid prognostic method has a rapid execution time for all the training, evaluation and prediction parts. With different moving window coefficient N from 100 to 700, the forecasting process is capable for on-line prognostic with a time step level in the order of several seconds.

4.3.4.3 Third Case Study: Comparison of the Proposed Hybrid Method with Other Methods

In the third case, a 600 W PEM fuel cell stack (5 cells) is operated for 1200 hours aging test under stationary condition with a static current density of $0.70A/cm^2$. This third case experiment aims to show the prediction performance comparison between the proposed hybrid method and other methods. The operation conditions of this case experiment are listed in table 4.6.

Table 4.6 Operation conditions of the third case study: 600W fuel cell stack

	Third case study
Stack type	600W PEMFC assembled at FCLAB
Number of cells	5
Operation mode	Recirculation mode
Air supply	Air boiler
Cooling	Cooling water system
Operating hours	1200h
Active area	$100\mathrm{cm}^2$
Stack current density	$0.70\mathrm{A/cm}^2$

By down-sampling the original measured data, the 1200 hours degradation voltage and power of PEMFC are shown in the figure 4.30.

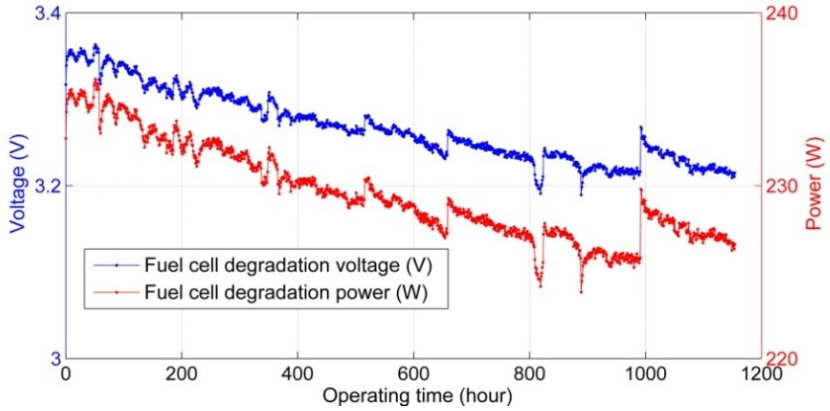

Figure 4.30 The third case 1200 hours aging test under a static current density of $0.70\mathrm{A/cm^2}$: fuel cell degradation voltage and power.

By applying the model-based method, the data-driven prognostic method and the proposed hybrid prognostic method with the same moving window horizon N of 165 hours (corresponds to one week), the comparison of prediction voltages is shown in figure 4.31.

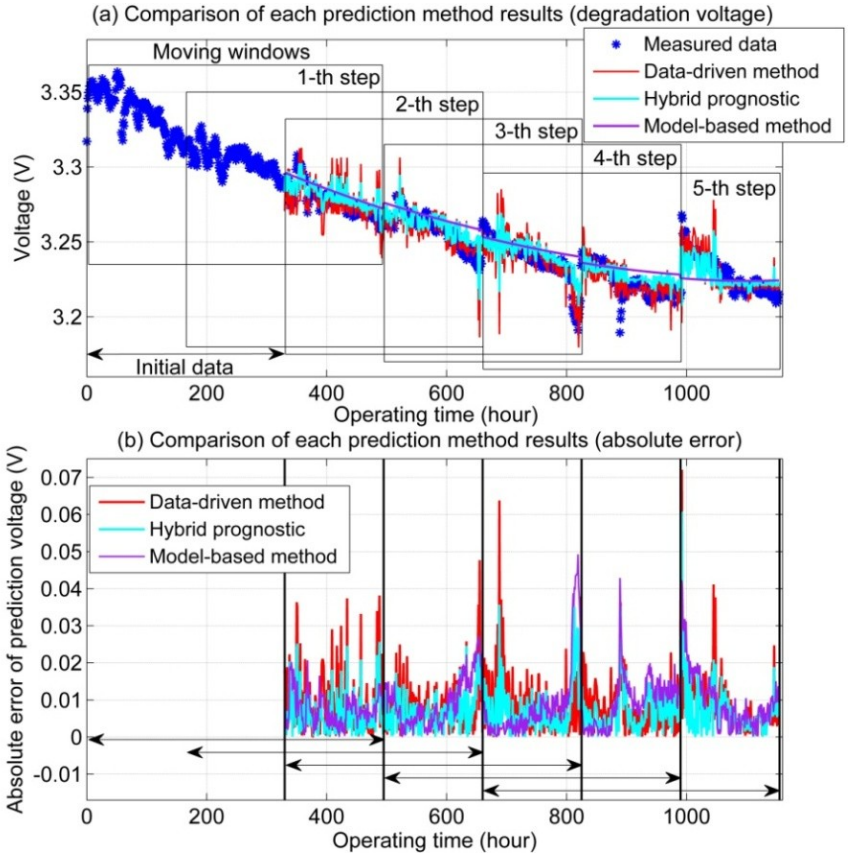

Figure 4.31 Comparisons of three prediction method (voltage and absolute error).

It can be seen from the figure 4.31 that, the proposed hybrid prognostic method can represent both the fade trend and non–linear features observed in the fuel cell voltage degradation data. The comparison of mean prediction error between the proposed methods and Adaptive Neuro-Fuzzy Inference System (ANFIS) algorithm [11] is shown in table 4.7. It can be seen that the proposed hybrid prognostic method can ensure a higher prediction accuracy than the both single prediction method, and could achieve nearly 21% improvement on the mean prediction error compared with the ANFIS algorithm. In addition, it is important to consider that the algorithm in [11] uses more degradation data (from 0 to 825 hours) for training the ANFIS, while the proposed moving window based prognostic approach requires fewer degradation data (only from 0 to 330 hours) for the first training, and can dynamically retrain the models during the forecasting process using the newly measured data. The above prediction results and analysis demonstrate the robustness and effectiveness of the proposed hybrid prognostic method.

Table 4.7 Comparison of mean prediction error between the proposed methods and ANFIS algorithm [11]

	Model-based method	Data-driven method	Hybrid prognostic method	ANFIS algorithm [11]
Mean error	0.0093	0.0089	0.0069	0.0087

In order to further show the prediction performance comparison of each moving window step between the proposed hybrid method and other method, the fuel cell power degradation dataset (shown as red curve in figure 4.30) is used to perform the proposed prediction methods. The forecast time is also set to one week (moving window horizon $N = 165$ hours), the comparison of prediction power is shown in the figure 4. 32.

The comparison of Root Mean Square Errors (RMSEs) between the proposed methods and Auto-Regressive Integrated Moving Average (ARIMA) algorithm [12] is shown in table 4.8.

It can be seen from the table 4.8 that, the proposed hybrid method shows again a better prediction performance than single model method. Compared with the ARIMA algorithm in [12], the proposed hybrid method could achieve higher forecasting accuracy from the fourth week to the sixth week, the RMSE result of the proposed hybrid method is nearly 19% less than that of ARIMA algorithm for the total four weeks.

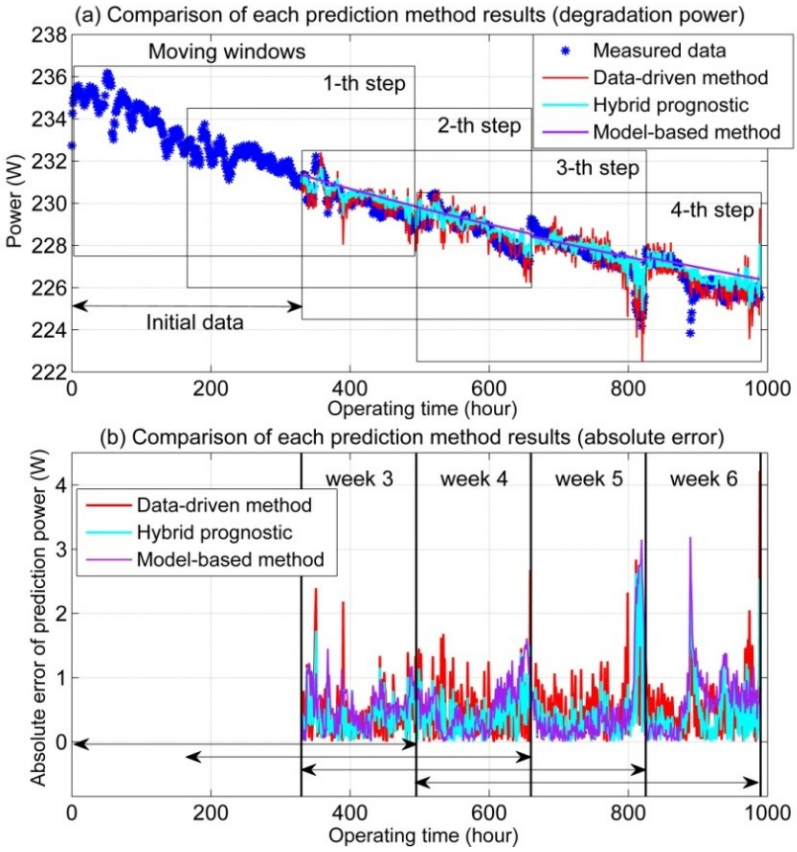

Figure 4.32 Comparisons of three prediction method results (power and absolute error).

Table 4.8 Comparison of RMSEs between the proposed methods and ARIMA [12]

	Model-based method	Data-driven method	Hybrid method	ARIMA algorithm [12]
Week 3	0.6184	0.5832	0.4778	0.4
Week 4	0.6458	0.6377	0.5145	0.6
Week 5	0.8026	0.8571	0.6633	0.7
Week 6	0.8027	0.7523	0.6265	1.1
Total four weeks	0.7198	0.7075	0.5705	0.7

4.3.5 Conclusion

In this section, an innovative approach based on a combination of different prognostic methods has been proposed for the application of PEMFC performance degradation prediction (please refer to previous work [43]). The proposed hybrid prognostic method considers two basic prediction approaches: model-based approach and data-driven approach. Model-based approach can be efficiently used to forecast the fuel cell aging trend in a long-range forecast time. Data-driven approach can accurately describe the local non-linear characteristics of degraded voltage for the short-range and medium-range prediction time.

By combining the advantages of the above two common prediction methods (i.e. model-based approach and data-driven approach), the proposed method in this thesis can simultaneously and accurately capture the long-term fuel cell voltage degradation trend, as well as the non-linear voltage variation characteristics. In addition, a novel approach using the moving window technique is applied in order to iteratively update the parameters during the prediction process. Furthermore, the prediction performance evaluation of the proposed hybrid prognostic approach with different moving window length is further shown and discussed.

Three experimental validations with three different PEMFC stacks and different aging test profiles have been performed to verify the accuracy and effectiveness of the proposed fuel cell performance degradation prediction method. The presented results can help engineers to appropriately choose the moving window length, in order to achieve simultaneously high prediction precision and relatively long forecast time for on-line prognostic, for example, the fuel cell hybrid electric vehicle (FCHEV) [] [].

4.4 Reference

[1] A. Gebregergis, P. Pillay, R. Rengaswamy, "PEMFC fault diagnosis modeling and mitigation," *IEEE Trans. Ind. Appl.*, vol. 46, no. 1, pp. 295-303, Jan. 2010.

[2] X. Hu, S. Li, Z. Jia, B. Egardt, "Enhanced sample entropy-based health management of Li-ion battery for electrified vehicles," *Energy*, vol. 64, pp. 953-960, 2014.

[3] D. Zhou, Z. Yu, H. Zhang, S. Weng, "A novel grey prognostic model based on Markov process and grey incidence analysis for energy conversion equipment degradation. *Energy*, vol. 109, pp. 420-429, 2016.

[4] M. Jouin, R. Gouriveau, D. Hissel, M. Pera and N. Zerhouni, "Prognostics of PEM fuel cell in a particle filtering framework," *Int. J. Hydrogen Energy*, vol. 39, pp. 481-494, 2014.

[5] M. Bressel, M. Hilairet, D. Hissel, B. Ould-Bouamama, "Extended Kalman filter for prognostic of proton exchange membrane fuel cell," *Appl. Energy*, vol. 164, pp. 220–227, Feb. 2015.

[6] H. Chen, P. Pei, M. Song, "Lifetime prediction and the economic lifetime of proton exchange membrane fuel cells," *Appl. Energy*, vol. 142, pp. 154–163, Mar. 2015.

[7] D. Marra, M. Sorrentino, C. Pianese, B. Iwanschitz, "A neural network estimator of SOFC performance for on-field diagnostics and prognostics applications," *J. Power Sources*, vol. 241, pp. 320–329, 2013.

[8] Z. Zhong, X. Zhu, G. Cao, "Modeling a PEMFC by a support vector machine," *J. Power Sources*, vol. 160, pp. 293–298, 2006.

[9] R. Silva, R. Gouriveau, S. Jemei, D. Hissel, L. Boulon, K. Agbossou, et al., "Proton exchange membrane fuel cell degradation prediction based on adaptive neuro fuzzy inference systems," *Int. J. Hydrogen Energy*, vol. 39, pp. 11128-11144, Jan. 2014.

[10] D. Marra, M. Sorrentino, C. Pianese, B. Iwanschitz, "A neural network estimator of Solid Oxide Fuel Cell performance for on-field diagnostics and prognostics applications," *J. Power Sources*, vol. 241, pp. 320–329, 2013.

[11] L. Mao, L. Jackson, "Selection of optimal sensors for predicting performance of polymer electrolyte membrane fuel cell," *J. Power Sources*, vol. 328, pp. 151–160, 2016.

[12] M. Ibrahim, N. Steiner, S. Jemei, D. Hissel, "Wavelets-Based Approach for On-line Fuel Cells Remaining Useful Lifetime Prediction," *IEEE Trans. Ind. Electron.*, vol. 63, pp. 5057-5068, 2016.

[13] D. Zhou, Y. Wu, F. Gao, E. Breaz, A. Ravey A. Miraoui, "Degradation Prediction of PEM Fuel Cell Stack Based on Multi-Physical Aging Model with Particle Filter Approach," *IEEE Trans. Ind. App.,* IEEE Trans. Ind. App., Vol. 53, Issue.4, Pages 4041-4052, 2017.

[14] D. Zhou, Y. Wu, F. Gao, E. Breaz, A. Ravey, A. Miraoui, "Degradation prediction of PEM fuel cell stack based on multi-physical aging model with particle filter approach," *IEEE Industry Applications Society Annual Meeting*, Portland, OR, Oct. 2-6, 2016.

[15] W. Fowler, R. Mann, J. Amphlett, B. Peppley, P. Roberge, "Incorporation of voltage degradation into a generalised steady state electrochemical model for a PEMFC," *J. Power Sources*, vol. 106, pp. 274-283, 2002.

[16] D. Song, Q. Wang, Z. Liu, T. Navessin, M. Eikerling, S. Holdcroft, "Numerical optimization study of the catalyst layer of PEM fuel cell cathode," *J. Power Sources*, vol. 126, pp. 104-111, Feb. 2004.

[17] D. Zhou, A. Ravey, F. Gao, D. Paire, A. Miraoui, and K. Zhang, "On-line estimation of state of charge of Li-ion battery using an iterated extended Kalman particle filter," in *Proc. IEEE ITEC*, Jun. 14-17, 2015, pp. 1-5.

[18] H. Dai, X. Wei, Z. Sun, J. Wang, and W. Gu, "On-line cell SOC estimation of Li-ion battery packs using a dual time-scale Kalman filtering for EV applications," *Applied Energy*, vol. 95, pp. 227-237, 2012.

[19] J. B. Rawlings and B. R. Bakshi, "Particle filtering and moving horizon estimation," *Computers and Chemical Engineering*, vol. 30, pp. 1529–1541, 2006.

[20] X. Liu, Z. Chen, C. Zhang, J. Wu, "A novel temperature-compensated model for power Li-ion batteries with dual-particle-filter state of charge estimation," *Applied Energy*, vol. 123 (15), pp. 263–272, Jun. 2014.

[21] M. Arulampalam, S. Maskell, N. Gordon, T. Clapp, "A Tutorial on Particle Filters for On-line Non-linear/Non-Gaussian Bayesian Tracking," *IEEE Trans. Signal Process.*, vol. 50, no. 2, pp. 174-188, Feb. 2002.

[22] A. Doucet, N. Gordon, V. Krishnamurthy, "Particle filters for state estimation of jump Markov linear systems," *IEEE Trans. Signal Process.*, vol. 49, no. 3, pp. 613-624, 2001.

[23] D. Zhou, K. Zhang, A. Ravey, F. Gao, A. Miraoui, "Parameter Sensitivity Analysis for Fractional-Order Modeling of Lithium-Ion Batteries," *Energies*, vol. 9, no. 123, 2016.

[24] J. Forman, S. Moura, J. Stein, and H. Fathy, "Genetic identification and fisher identifiability analysis of the Doyle–Fuller–Newman model from experimental cycling of a LiFePO4 cell," *J. Power Sources*, vol. 210, pp. 263– 275, 2012.

[25] B. Sana, K. Goebel, J. Christophersen, "Comparison of prognostic algorithms for estimating remaining useful life of batteries," *IEEE Trans. Inst. Meas. Contr.*, vol. 31, pp. 293–308, June–Aug. 2009.

[26] Q. Miao, L. Xie, H. J. Cui, W. Liang, M. Pecht, "Remaining useful life prediction of lithium-ion battery with unscented particle filter technique," *Microelectron. Rel.*, vol. 53, no. 6, pp. 805-810, Jun. 2013.

[27] D. Wang, Q. Miao, M. Pecht, "Prognostics of lithium-ion batteries based on relevance vectors and a conditional three-parameter capacity degradation model," *J. Power Sour.*, vol. 239, pp. 253-264, Oct. 2013.

[28] W. He, N. Williard, M. Osterman, M. Pecht, "Prognostics of lithium-ion batteries based on Dempster–Shafer theory and the Bayesian Monte Carlo method," *J. Power Sour.*, vol. 196, pp. 10314–10321, 2011.

[29] S. Cleghorn, D. Mayfield, D. Moore, J. Moore, G. Rusch, T. Sherman, "A polymer electrolyte fuel cell life test: 3 years of continuous operation," *J. Power Sour.*, vol. 158, no.1, pp. 446-454, 2006.

[30] A. G. Parlos, O. T. Rais, A. F. Atiya, "Multi-step-ahead prediction in complex systems using dynamic recurrent neural networks," *Neural Networks*, vol. 13, no. 7, pp. 765-786, Sept. 2000.

[31] K. Benmouiza, A. Cheknane, "Forecasting hourly global solar radiation using hybrid k-means and non-linear autoregressive neural network models," *Energy Convers Manage*, vol. 75, pp. 561-569, 2013.

[32] M. Ibrahim, S. Jemei, G. Wimmer, D. Hissel, "Non-linear autoregressive neural network in an energy management strategy for battery/ultra-capacitor hybrid electrical vehicles," *Electr. Power Syst. Res.*, vol. 136, pp. 262-269, 2016.

[33] S. Arbain, A. Wibowo, "Neural networks based non-linear time series regression for water level forecasting of Dungun river," *J. Comput. Sci.*, vol. 8, pp. 1506-1513, 2012.

[34] M. I. Lourakis, "A brief description of the Levenberg–Marquardt algorithm implemented by Levmar," *Matrix*, vol. 3, pp. 2, 2005.

[35] J. Tu, "Advantages and disadvantages of using artificial neural networks versus logistic-regression for predicting medical outcomes," *J. Clin. Epidemiol.*, vol. 49, pp. 1225-1231, 1996.

[36] J. Yuan, H. Chen, F. Sun, and Y. Huang, "Multisensor Information Fusion for People Tracking With a Mobile Robot: A Particle Filtering Approach," *IEEE Trans. Ins. Measure*, vol. 64, pp. 2427-2442, 2015

[37] G. Battistelli, L. Chisci, S. Morrocchi, F. Papi, A. Farina, and A. Graziano, "Robust Multisensor Multitarget Tracker with Application to Passive Multistatic Radar Tracking," *IEEE Trans. Aerospace. Electronic*, vol. 48 (4), pp. 3450–3472, 2012.

[38] G. Wang, S. Tan, C. Guan, N. Wang, and Z. Liu, "Multiple model particle filter track-before-detect for range ambiguous radar," *Chinese Journal of Aeronautics*, vol. 26 (6), pp. 1477–1487, Dec 2013.

[39] D. Svensson, and L. Svensson, "A New Multiple Model Filter With Switch Time Conditions," *IEEE Trans. Signal Process.*, vol. 58, no. 1, pp. 11-25, Jan. 2010.

[40] K. Punithakumar, T. Kirubarajan, and A. Sinha, "Multiple-model probability hypothesis density filter for tracking maneuvering targets," *IEEE Trans. Aerospace. Electronic*, vol. 44, no. 1, pp. 87-98, Jan. 2008.

[41] J. Lan, X. Li, V. Jilkov, C. Mu, "Second-Order Markov Chain Based Multiple-Model Algorithm for Maneuvering Target Tracking," *IEEE Trans. Aerospace. Electronic*, vol. 49, no. 1, pp. 3-19, Jan. 2013.

[42] F. Caron, M. Davy, E. Duflos, and P. Vanheeghe, "Particle Filtering for Multisensor Data Fusion With Switching Observation Models: Application to Land Vehicle Positioning," *IEEE Trans. Signal Processing*, vol. 55, no. 6, pp. 2703-2719, Jun. 2007.

[43] D. Zhou, F. Gao, E. Breaz, A. Ravey, A. Miraoui, "Degradation Prediction of PEM Fuel Cell Using a Moving Window Based Hybrid Prognostic Approach," *Energy*, vol. 138, pp. 1175-1186, Nov. 2017;

[44] D. Zhou, A. Al-Durra, F. Gao, A. Ravey, I. Matraji, M. G. Simões, "On-line energy management strategy of fuel cell hybrid electric vehicles based on data fusion approach," *Journal of Power Source*, Vol. 366, pp. 278-291, 2017;

[45] D. Zhou, A. Ravey, A. Al-Durra, F. Gao, "A Comparative Study of Extremum Seeking Methods Applied to Online Energy Management Strategy of Fuel Cell Hybrid Electric Vehicles," *Energy Conversion and Management*, Vol. 151, pp. 778-790, 2017.

CONCLUSION

Before mass commercialization of proton exchange membrane fuel cell, the research on the design of appropriate control strategies and auxiliaries need to be done for achieving proton exchange membrane fuel cell (PEMFC) optimal working modes. An accurate mathematical PEMFC model can be used to observe the internal variables and state of fuel cell during its operation, and could further greatly help the system control strategy development.

A comprehensive multi-physical dynamic model for PEMFC is developed in chapter I. The proposed model covers multi-physical domains for electric, fluidic and thermal features. Particularly, the transient phenomena in both fluidic and thermal domain are simultaneously considered in the proposed model, such as the dynamic behaviors of fuel cell membrane water content and temperature. Therefore, this model can be used to analyze the coupling effects of dynamic variables among different physical domains.

Based on the developed multi-physical PEMFC model, a full two-dimensional multi-physical model is further presented. The proposed model covers electrical and fluidic domains with an innovative 2-D modeling approach. In order to accurately describe the characteristics of reactant gas convection in the channels and diffusion through the gas diffusion layer, the gas pressure drop in the serpentine pipeline is comprehensively analyzed by fully taking the geometric form of flow field into consideration, such as the reactant gas pressure drop due to the pipeline sharp and U-bends. Based on the developed 2-D fluidic domain modeling results, spatial physical quantity distributions in electrical domain can be further obtained. Therefore, this 2-D PEMFC model can be use to study the influences of modeling parameters on the local multi-dimensional performance prediction. The simulation and experimental test are then performed to validate the proposed 2-D model with a commercial Ballard NEXA 1.2 kW PEMFC stack.

In chapter II, analyses of dynamic phenomena step responses are conducted based on the developed multi-physical dynamic PEMFC model using the relative gain array (RGA) method for various control input variables, in order to quantitatively analyze the coupling effects in different physical domains, such as the interactions of membrane water content and temperature. Based on the calculated values of relative gain array, the proposed model can be considered as a fuel cell MIMO system, which could be divided into two independent control sub-systems by minimizing parameter coupling effects between each other. Due to the closely coupled parameters in the proposed

first control sub-system, a decoupling control method is recommended to achieve optimized control results. The coupling analysis presented in this thesis can help engineers to design and optimize the fuel cell control strategies, especially for the water and thermal management in fuel cell systems.

A mathematical solver algorithm for the developed 2-D multi-physical real-time model of proton exchange membrane fuel cell is presented in Chapter III using an efficient tridiagonal matrix algorithm (TDMA). TDMA uses a special form of elimination, and solves the tridiagonal matrices in a backward substitution, its arithmetic complexity exponential decays to operations $O(n)$ compared with straightforward Gaussian elimination $O(n^3)$.

In order to thoroughly and effectively describe the gas flow characteristics in serpentine channels, the differential equations of reactant gas convection and diffusion phenomena are transformed into tridiagonal matrix. In addition, an original iterative solver algorithm composed by three interactive computational loops is also developed in the model, in order to obtain spatial physical quantity distributions of electrochemical domain in real-time. The experimental results demonstrate the practical feasibilities of the proposed 2-D model for advanced real-time control of PEMFC systems with a control loop time level on the order of milliseconds. The model execution time can be at least 4 times faster compared with step-by-step computing. Such short execution time of the proposed 2-D model ensures fast control decisions and actions based on the predicted local phenomena and spatial distribution physical variables inside the fuel cells.

Two different prognostic approaches for PEMFC performance degradation prediction is proposed in the Chapter IV. In the first part, a novel approach for PEMFC output voltage prediction based on a multi-physical aging model with particle filter and data extrapolation approach is proposed. The proposed multi-physical aging model fully considers the three most important aging phenomena during PEMFC operation: ohmic losses, reaction activity losses, and reactants mass transfer losses. The proposed prediction method is divided into two stages: learning phase and prediction phase. During the learning phase, the particle filter is applied to study the non-linear aging behavior and update the proposed aging parameters. Then, different fitting curve functions are used to represent and extrapolate the aging parameters in the learning phase. Three experimental validations with different aging testing profiles have been performed. The prediction results demonstrate that, this physical-based method could provide an acceptable prediction results under the condition of limited initial training samples.

However, the proposed physical-based method is a single-step prognostic method, which cannot be directly used in the on-line prognostic applications. In order to achieve on-line prognostic, it is important to develop an iteration-based prediction strategy, which allows the prediction result to be dynamically updated with the newest dataset (newly measured data) for iterative data training at next prediction step.

For this purpose, in the second part of chapter IV, a moving window based prediction method is developed, in order to dynamically retrain the models during the forecasting process with new data inputs. In addition, this approach is based on a combination of model-based and data-driven prognostic methods. By combining the advantages of the above two common prediction methods, the proposed hybrid method can simultaneously and accurately capture the long-term fuel cell voltage degradation trend, as well as the non-linear voltage variation characteristics. Furthermore, the prediction performance evaluation of the proposed hybrid prognostic approach with different moving window length is further shown and discussed. Three experimental validations with three different PEMFC stacks and different aging test profiles have been performed to verify the accuracy and effectiveness of the proposed hybrid method. The presented results can help engineers to appropriately choose the moving window length, in order to achieve simultaneously high prediction precision and relatively long forecast time for on-line prognostic applications.